DISSERTATION

BIOMATERIAL APPLICATIONS OF CROSS-LINKED POROUS PROTEIN MICROCRYSTALS

Submitted by

Alec Arthur Jones

School of Biomedical and Chemical Engineering

In partial fulfillment of the requirements

For the Degree of Doctor of Philosophy

Colorado State University

Fort Collins, Colorado

Summer 2026

Doctoral Committee:

Advisor: Christopher D. Snow

Timothy Stasevich
Christie Peebles
Dan Regan

ABSTRACT

BIOMATERIAL APPLICATIONS OF CROSS-LINKED POROUS PROTEIN MICROCRYSTALS

Porous protein crystals represent a promising but underexplored class of biomaterials for therapeutic delivery, molecular capture, and biofunctional scaffolding. This dissertation investigates the synthesis, stabilization, and biomedical applications of cross-linked porous protein microcrystals derived from a putative polyisoprenoid-binding protein from *Campylobacter jejuni* ("CJ"). These crystals possess a highly ordered P622 lattice with large solvent channels and can be reproducibly generated as microcrystals through batch crystallization and stabilized via chemical cross-linking.

Chapter 1 provides a review of the broader landscape of large-pore protein crystals, including methods of synthesis, stabilization, validation, and emerging applications in catalysis, delivery, and functional materials. In chapter 2, I demonstrate that CJ microcrystals can adsorb and retain diverse nucleic acid cargos, including single-stranded DNA, RNA, and plasmid DNA. Guest loading is rapid, dependent on pH and guest size, and can be partially reversed by exposure to high ATP concentrations, indicating specific but heterogeneous interactions between nucleic acids and the crystal scaffold. Because unmodified pores remain accessible to nucleases, I further show that a hexameric protein complex derived from the D2 domain of N-ethylmaleimide sensitive factor can function as a physical pore cap, significantly reducing nuclease-mediated degradation of guest nucleic acids.

In chapter 3, I extend the CJ platform toward selective capture of virus-sized particles by engineering SpyTag-bearing "SpyCrystals" that covalently host SpyCatcher fusion proteins. Functionalized crystals displaying SARS-CoV-2 spike binders selectively adsorb virions *in vitro* and can be integrated into a pump-driven filtration workflow for capture from wastewater. In chapter 4, I also evaluate *ex vivo* biocompatibility in precision-cut lung slices, showing that unloaded CJ crystals do not measurably impair tissue health or alter B-cell abundance, while lipopolysaccharide-loaded crystals elicit a moderated biological response consistent with guest release. Finally, in chapter 5, I investigate *in vivo* biodistribution using bioluminescent CJ microcrystals and find evidence consistent with rapid pulmonary exposure followed by partial retention in skeletal muscle microvasculature.

Collectively, this dissertation establishes cross-linked porous protein microcrystals as structurally precise, modular biomaterials with potential applications in nucleic acid delivery, pathogen capture, localized depot formation, and engineered therapeutic scaffolding.

ACKNOWLEDGEMENTS

First and foremost, I would like to express my sincerest gratitude to my advisor, Dr. Christopher Snow. Beyond your direct mentorship during my time in your lab, you have also been a North Star to me in terms of your scientific and engineering competence, deep creativity, and your infectious enthusiasm for your craft. Beyond teaching me to be a better scientist, you have also shown me how to be a better team leader, for which I am especially grateful.

I would also like to thank the members of my committee, Dr. Timothy Stasevich, Dr. Christie Peebles, and Dr. Daniel Regan, for their time commitment, patience, and continued guidance.

Among my collaborators, I first want to thank Dr. Katherine Horak and Laura Chubb (chapters 2 and 5) and Moe Masri (chapter 2); Dr. Susan De Long, Dr. Carol Wilusz, John Mizia, Semin Barlak (chapter 3); and Dr. Stu Tobet and Brielle Patlin (chapter 4).

I would also like to thank all of my undergraduate mentees: Anika O'Brian, Isaac Lewis, Brian Kelly, Tim Ahr, Lauren Beatty, Cole Sheperd, Lauren Frueh, and Matthieu Henry. You have all taught me so much more than I was ever able to teach you.

I would also like to thank my additional fellow Snow lab members, current and former: Rachel Cohen, Ashlyn Chen, Dr. Callie Slaughter, Emma Magna, John League, Dr. Jacob Deroo, Dr. Abby Orun, Dr. Julius Stuart, Dr. Ethan Shields, Austin Knight, and Pegah Eizadkhah.

Sara Neys, for her continued help navigating the PhD program and helping me meet deadlines.

I would additionally like to thank my undergraduate mentor, Dr. April DeLaurier, who first set me on my journey as a scientist. You taught me that every new discovery is a miracle, no matter how minor it may seem. And finally, I would like to thank my father, Gregory, my mother, Mary, and my sister, Julie, for their unwavering love and moral support, and for giving me a purpose to aspire to.

TABLE OF CONTENTS

LIST OF FIGURES

CHAPTER 1: Applications of Porous Protein Crystals

1.1 Overview

Proteins are well-suited as a substrate for biomaterial applications, due to their biocompatibility,[1] and structural diversity.[2] A variety of mesostructures emerge as a property of their constitutive nanostructures; these include protein nanoparticles,[3] nanocages,[4,5] hydrogels,[6] plate-like crystals and sheets,[7,8] and porous scaffolds.[9–11]

Porous materials, with their ability to host and transport guest molecules within their frameworks, have been explored in recent years for diverse scientific and industrial applications. Among these, large-pore protein crystals (LPCs) represent a distinctive class of crystalline materials characterized by a three-dimensional network of interconnected voids and channels. Large-pore protein crystals exhibit remarkable structural diversity compared with traditional nanomaterials, owing to the diversity of protein sequences found in nature. A typical bacterial protein sequence of 300 amino acids,[12] could have 20^{300} distinct amino acid sequences; assuming ~8 conformational degrees of freedom per residue,[13,14] the number of possible conformations extends to ~1.72×10^{661} theoretical conformations, effectively an infinite landscape of structural diversity. While most of these hypothetical structures would be unstable and any plausible structure would be restricted to narrowly defined minima within this energy landscape, the number of stable structures is nevertheless vast. The ability of proteins to undergo genetic selection, along with the wholesale shuffling and recombination of entire protein domains[15] enables a realistic sampling of this landscape. The enormous diversity of protein structures (and

functions) has sparked a growing interest in their potential applications as biomimetic scaffolds.

The unique architecture of protein crystals arises from the self-assembly of protein molecules into ordered, crystalline structures. Protein crystals typically contain a high surface area to volume ratio[16] with a well-defined lattice of interconnected pores. Pore diameters typically range from tens of Angstroms to greater than 10 nm, with corresponding wide-ranging solvent content between 27% and 65%.[11,17–21] These solvent channels enable the accommodation of a wide array of guest molecules, from small ions to large biomolecules such as peptides, nucleic acids, and other proteins. Possessing solvent channels of sufficient size for guest macromolecule transport would be one characteristic of the LPC subset of protein crystals. The Matthews coefficient (V_M), defined as the fraction of crystal volume per unit of protein molecular weight ($Å^3$/Da), is a useful parameter for specifying solvent content. More recent estimates on the distribution of V_M, based on reported crystallographic data, suggest that V_M of reported protein crystals is quite broad, from extremely high density (just over 1 $Å^3$/Da, approximating tightly-packed spheres) to extremely low density in the case of LPCs (just

below 10 $Å^3$/Da).[22,23]

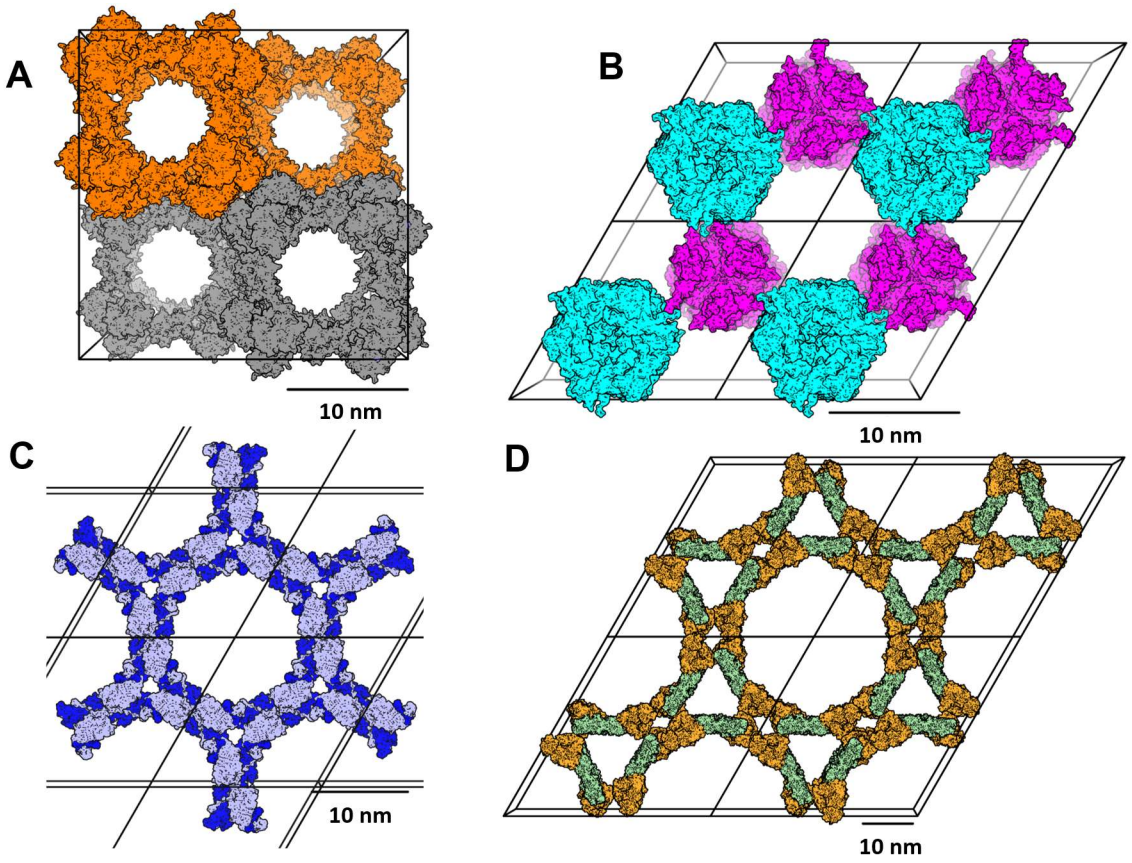

Figure 1.1: Lattice structures for Protein Database depositions **(A)** 4QCC, **(B)** 2INY, **(C)** 5W17, and **(D)** 2IOU, illustrating the diversity of porous nanostructures found in protein crystals. Pore diameters range from ~10 nm (2INY), up to ~30 nm (2IOU). Scale bar = 100 Å.

Understanding the formation mechanisms of LPCs is pivotal for their controlled synthesis. Crystallization of biomolecules is notably distinct from crystallizing small molecules, owing primarily to their increased molecular weight and complexity. The crystallization process involves an interplay of many factors, including protein concentration, pH, temperature, ionic strength, and the presence of precipitants and nucleating agents.[24] Proteins have additional considerations such as susceptibility to misfolding and ease of expression and purification. Recent advances in protein engineering and biophysical techniques have facilitated the rational design and optimization of LPCs.

Notably, while LPC growth is similar to the growth of other less porous protein crystals, one qualitative difference is that sufficiently large pores could allow building blocks throughout the crystal to exchange with solution. A candidate quantitative threshold for LPCs, therefore, would be any protein crystal with solvent channels of sufficient diameter to allow transport of the constituent crystal building blocks. Precise nanopore sizes within a crystal lead to a sharp cutoff on transport depending on guest size. Accordingly, biomolecular crystals have been explored as molecular sieves for selective adsorption and separation of biomolecules.[25] The confined environment within LPCs also provides a unique platform for enzyme immobilization and colocalization, enhancing catalytic efficiency and stability.[26–28] Specific applications for LPCs that have been investigated include catalysis, templating of nanostructures, and targeted therapeutic delivery of bioactive compounds, which will be broadly described in this chapter.

1.1.1 Common synthesis methods

Historically, protein crystallization has been most often used for the specific purpose of generating large, uniform crystals that are ideal for X-ray diffraction.[29] Due to their irregular shape and complex interactions with each other and the surrounding solvent, many proteins have a tendency to crystallize into structures which feature sizable solvent-filled cavities and pores. Multiple synthesis routes have been described for generating nanoporous scaffolds from proteins. The most commonly reported approach involves first growing the crystal using conventional methods, such as sitting- or hanging-drop vapor diffusion or batch crystallization. Vapor diffusion methods generally result in larger, fewer crystals, and are more suited towards generating crystals for X-ray diffraction. One common approach involves mixing concentrated protein stock with a high-ionic strength

precipitant buffer (e.g. a buffered high-salt solution, such as sodium chloride or ammonium sulphate). The wells also contain a reservoir containing the undiluted precipitant solution. The wells are subsequently sealed, and water molecules diffuse through the vapor phase between the well solution and the droplet containing protein. Due to the lower salt concentration within the protein droplet, equilibrium between the droplet and the well results in a gradual net decrease in volume in the protein droplet. The resulting gradual increase in protein and salt concentration occurs slowly enough that nucleation proceeds very slowly, and metastable growth of crystals can begin immediately after nucleation.

Batch crystallization is distinct from vapor diffusion in that both the protein and precipitant are mixed in a single volume, without any vapor-phase equilibration. At sufficiently high protein and precipitant concentrations, nucleation proceeds very rapidly, resulting in many smaller crystals. This approach is well-suited for generating a large number of small crystals, although it requires optimization to avoid issues such as excess protein aggregation. The "CJ" crystals described in this dissertation are grown from a putative polyisoprenoid-binding protein from *Campylobacter jejuni* have been shown to possess very large solvent channels (> 13 nm diameter), via X-ray diffraction[9] and atomic force microscopy.[30] We have frequently relied on batch crystallization to generate large

quantities of small porous microcrystals for a variety of applications.

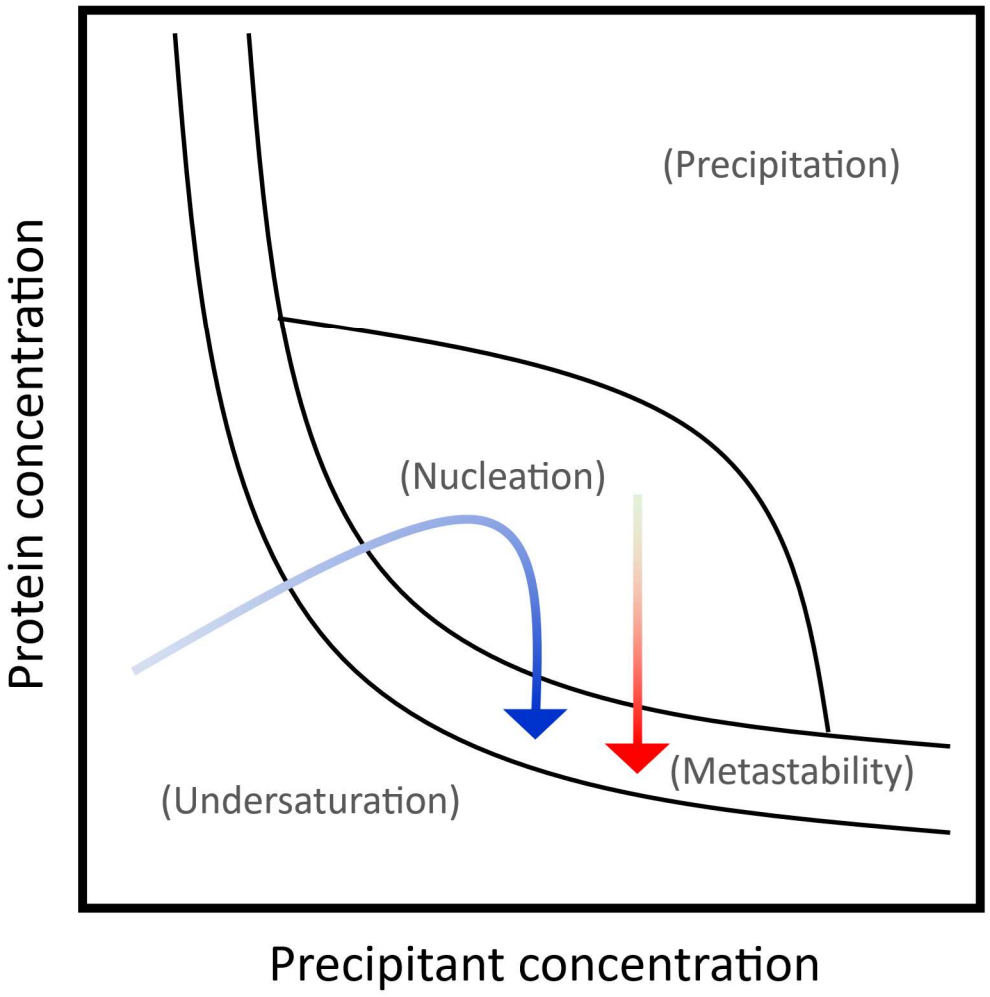

Figure 1.2: Phase diagram showing the trajectory, over time, of protein and precipitant concentration for vapour diffusion (blue gradient) and batch crystallization (red gradient).

Methods for generating porous protein structures include growth of complete structures from constituent monomers ("bottom-up"), or crystal growth followed by disassembly into sub-structures, such as protein nanotubes or cages. While the CJ crystals described in this dissertation are synthesized using a bottom-up approach, a number of approaches that instead use the crystal form as a template have been described. For instance, Ueno and coworkers constructed a supramolecular nanotube assembly, by mutating a key interface residue (I149C) in RuBisCO from *Thermococcus kodakaraensis*.[31] After growth, the

crystals were cross-linked in an oxidizing buffer for 24 hours; following cross-linking, the crystals were dissolved into their constituent nanotubes by soaking in an alkaline solution, and subsequently characterized via transmission electron microscopy.[31] Proposed applications of such tubular assemblies include templating of nanomaterials, as confinement within the tube enables size-restricted growth of inorganic materials like nanorods. Similar top-down strategies for synthesizing porous protein structures, specifically protein cages, have been employed by the Care group[32] and Hilvert group.[5]

1.1.2 Control of size and morphology

For most of the downstream applications described in this dissertation, it is favourable to generate monodisperse crystals of very small sizes (ideally less than 5 μm in diameter). For this reason, many methods have been explored for generating nano- and microcrystals in large batches. Crystal size, as well as crystallization efficiency (defined as the ratio of crystallized protein to total protein) is influenced most heavily by protein concentration, followed by precipitant concentration, temperature, pH, and the presence of nucleating agents.[33]

The canonical methods for growing protein crystals include batch crystallization, microdialysis, and sitting- and hanging-drop vapor diffusion. While vapor diffusion is a preferred method for growing large crystals, droplet handling is typically impractical for generating many small crystals. Nevertheless, it can be useful in the context of studying the behaviour of LPCs at a visible scale. Within our group, thanks to the conserved nanostructure of both large and small crystals, we routinely predict the behaviour of

smaller porous microcrystals from X-ray diffraction and fluorescence microscopy of larger crystals, which are easier to manipulate and observe.[11,34,35]

1.1.3 Methods for enhancing crystal stability

Most crystals derived from biomolecules are susceptible to dissolution when transferred outside of their mother liquor. Therefore, it is often necessary to chemically cross-link the crystals following growth and washing, to ensure that they retain their structural integrity following solvent exchange. Some rare protein crystals, such as crystals derived from the insecticidal, *Bacillus thuringiensis*-derived Cry toxins[36,37] do not require additional downstream cross-linking. S-layer proteins, which confer structural rigidity to the outer membrane of certain prokaryotic species, have also been shown to form highly stable two-dimensional porous crystals on the surface of living cells.[38–40]

Commonly reported methods for stabilizing protein crystals include chemical methods such as formaldehyde,[41] glutaraldehyde,[42,43] 1-ethyl-3-(3-dimethylaminopropyl)-carbodiimide,[44,45] and glyoxal.[46,47] Oxidation of proximal cysteines to promote the formation of disulfide bonds within LPCs is another well-established strategy.[48–50] While sortases[51–53] and SpyCatcher/SpyTag[54] have been well studied in the context of enzyme immobilization and installation of guests within or on scaffolds, these systems have been

less characterized for their use in stabilizing the scaffold itself.

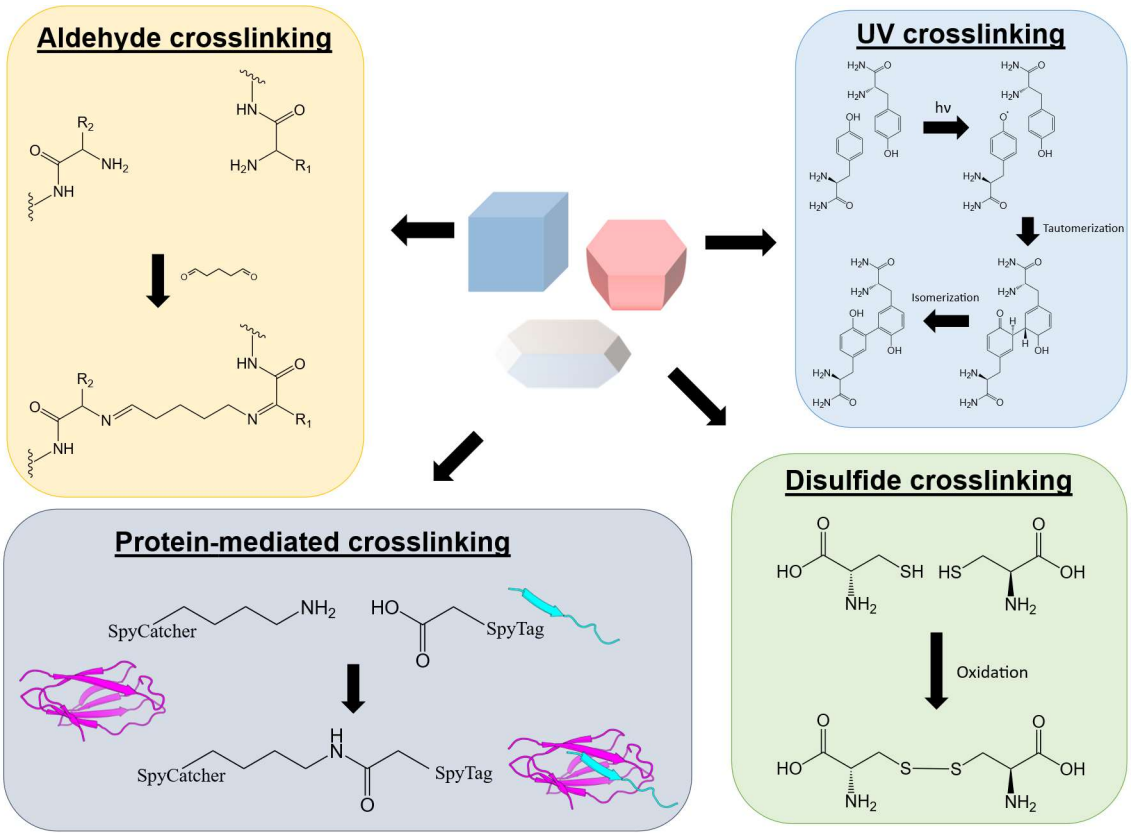

Figure 1.3: An overview of the various reported methods for cross-linking PPCs, or stabilizing guest-crystal interactions, via covalent bonds.

Solution exchange and downstream handling are potential challenges when cross-linking LPCs. In an ideal scenario, the crystals should be stabilized within their mother liquor immediately following or during growth, as downstream handling and washing steps and solution exchanges can result in mishandling and damaging of the crystals. Ultraviolet photo-cross-linking is an alternative strategy for LPC stabilization that remains largely unexplored. UV excitation of tyrosine-rich proteins in the presence of strong oxidizers, such as Ru(II) complexes, results in the formation of reactive radical species which can subsequently form covalent bonds with neighbouring tyrosines.[55] Similar chemistries are believed to contribute to the mechanical strength of insect wings[56] and fibroin and keratin structures in Tussah silk.[57] Dityrosine cross-linking has been

employed for other structure determination-based methods such as mass spectrometry[58,59] and NMR,[60] and has seen some use as a method for stabilizing protein films and nanoparticles.[61] At the same time, it should be noted that radical chemistry can result in multiple off-target effects; UV photo-cross-linking is a common method for sterilization and inactivating enzymes *in vitro*.[62] For biochemically inert scaffolds however, the reduced handling and transfer steps may make UV-induced cross-linking an attractive strategy for stabilizing LPCs. All of the crystals described throughout this dissertation have been stabilized via chemical cross-linking.

1.1.4 Methods for validating size, structure, and functionality

While this chapter has described some of the methods for generating LPCs, as well as stabilizing them outside of their mother liquor, it is worth noting that the methods for characterizing LPCs themselves are similarly diverse, and these depend in large part on the nature of the crystals themselves. Properties of interest include crystal size, porosity, dimensionality, and tolerance to desiccation. Many of the methods for studying the morphology and behaviour of LPCs overlap significantly with established techniques used in materials engineering, and structural and cell biology.

For small crystals, scanning electron microscopy (SEM) is often used to validate both the size and correct habit of porous microcrystals. For tiny crystals (< 1 μm diameter), dynamic light scattering (DLS) is another technique used for size validation and has the additional benefit of being able to measure the surface zeta potential. The latter property is critical for ensuring that crystals are monodisperse in solution. The Chan group has routinely used SEM and DLS on Cry3Aa crystals to validate their morphology and size.[10]

Throughout this dissertation, SEM was used to determine the size and shape of LPC microcrystals, and atomic force microscopy (AFM) for characterizing the pore surface of macroscopic crystals. Some advantages of AFM over TEM include its non-destructive nature, ease of sample preparation, and the ability to monitor guest-crystal interactions *in situ*.[30,63] Tunable resistive pulse sensing (TRPS) (commonly employed for quantifying extracellular vesicles and nanoparticles)[64] was also used for microcrystal batches to obtain size distributions and concentrations of microcrystal batches.

1.2 Specific Applications

1.2.1 Enzymatic scaffolds

The controlled confinement within crystal pores offers a unique platform for enzyme immobilization, luminescence trace-labeling, and biocatalysis. By harnessing the ordered structure and tailored pore sizes of LPCs, enzymes can be selectively encapsulated, resulting in enhanced stability and catalytic efficiency.[65,66] The integration of enzymes within LPCs not only expands the scope of biocatalytic processes but also may enable sustainable industrial applications due to increased reusability.

Kowalski et al. from our group previously characterized enzymatic activity in CJ crystals.[34] CJ crystallizes to form *P*622 crystals with large pores (~13 nm) along their hexagonal face, along with smaller flanking pores (~3 nm). Because CJ crystals typically have a hexahistidine tag at the C-terminus, the resulting tags project into the major pore. As a result, guest proteins which also have a polyhistidine tag are able to interact with the histidine tag inside of the crystal via shared metal affinity,[67] resulting in non-covalent "tethering" of the protein guest. In this study, CJ crystals were grown to large sizes (> 0.1 mm) using sitting-drop vapor diffusion, and subsequently cross-linked using glyoxal. The

resulting scaffolds remained resistant to dissolution after transferring outside their mother liquor. After cross-linking, the crystals were soaked in a basic buffer containing nickel, in order to saturate the histidine tags in the crystal with nickel ions. Co-loading of both GOX and HRP within the same crystal resulted in visible HRP activity throughout the crystal over a 2-minute period, following substrate addition. It was additionally observed that the crystal could be reused up to at least 5 recycles. These results demonstrated the feasibility of using protein crystals as a multi-enzyme scaffold, although this approach remained limited insofar as guest loading was non-covalent, and pH and metal dependent as a result of histidine tag tethering.

Recyclability of the scaffold in an industrial context is additionally a vital consideration. Heater et al. from the Chan group previously characterized the use of Cry3Aa crystals as a catalytic scaffold for the production of biodiesel from waste cooking oil.[68] Following their investigations of Cry3Aa structures, which revealed the presence of large pores (~50 Å x 50 Å), Heater et al. managed to confer lipase activity on crystals comprised of Cry3Aa-lipase fusion protein; the resulting crystals contained a lipase enzyme fused to the C-terminus of Cry3Aa, projecting into the pore space of conventional Cry3Aa crystals.[68] The Cry3Aa-lipase fusion was subsequently screened (while the crystals were still encapsulated within cells) for improved activity via directed evolution. Optimized crystals displayed slightly higher K_m values, and greatly reduced k_{cat} values. When the crystals were purified *in vitro*, they demonstrated fatty acid transesterification to fatty acid methyl esters (FAME) in a variety of harsh solvent conditions and following prolonged exposure to increased temperatures. The same crystals were capable of an impressive 15 reuse cycles despite having been centrifuged, washed twice with hexane,

and vacuum-dried between each cycle, with relative percent conversion remaining greater than 77%. The greatly reduced turnover may be explained as a result of suboptimal orientation of the immobilized enzyme. Similarly reduced catalytic efficiency was observed by Kowalski et al. for HRP immobilized within CJ crystal pores. It is probable that turnover and substrate binding are heavily influenced by a variety of factors that are difficult to control, such as the orientation of the enzyme active site relative to the crystal pore, as well as possible off-target binding between the guest enzyme and the pore wall.

An critical factor to consider with any reusable scaffold is modularity. It is self-evident that modification of a single platform to be able to accommodate multiple alternative guests is economically advantageous. Covalent installation of guest enzymes within a LPC is likewise desirable, as the resulting irreversible bond is neither pH or redox dependent, allowing the scaffold to tolerate a wider range of chemistries and solution conditions.[69] Following on their work with Cry3Aa-lipase crystals, Sun et al. attempted to introduce greater modularity in the Cry3Aa scaffold by fusing SpyCatcher at the C-terminus.[70] "SpyCatcher" is a 12.3 kDa protein, redesigned from the immunoglobulin-like CnaB2 domain from *Streptococcus pyogenes*, which is capable of reacting with a 13 amino acid peptide ("SpyTag") to form an intermolecular, isopeptide amide bond;[71] second and third generation variants which exhibit improved second-order rate constants have since been developed via directed evolution and rational design.[72] This platform has been used in a wide variety of applications, including enzyme immobilization,[73–75] recombinant protein purification,[76] and cyclization of protein termini to improve their stability.[77,78] By introducing SpyCatcher at the Cry3Aa terminus within the crystals, the Cry3Aa scaffolds were able to accommodate multiple different guest enzymes in a

modular fashion, thereby enabling the confinement of an entire metabolic pathway inside a single crystal scaffold.[70] The main limitation of this system is the narrowness of the crystal pores necessitates sequential guest loading on the basis of molecular weight/size. Crystals with larger diameter pores, such as those grown from CJ, could allow larger domain guests to load without steric occlusion of the solvent channels.

1.2.2 Therapeutic delivery

Previously well-characterized platforms for therapeutic delivery of DNA, RNA, proteins, and small molecules include gold nanoparticles,[79–81] mesoporous silica particles,[82–84] liposomes,[85,86] and polymer-based scaffolds such as chitosan[87] and agarose-based hydrogels.[88] While each of these platforms are traditionally treated as independent frontiers in medical research, and the methods of synthesis can vary substantially, there is a considerable degree of overlap in terms of their experimental and analytical methods. Alongside these existing platforms, LPCs represent an emerging frontier.

Porous micro- and nanocrystals are particularly amenable to delivery applications, as larger protein crystals localized to the bloodstream could result in capillary occlusion.[89] Additionally, morphology and aspect ratio of particles, which can be difficult to control for certain protein crystals, has been shown to greatly influence circulation time and organ and tissue localization.[90] As a result, there have been few reported accounts testing delivery *in vivo* using LPCs. The Chan lab tested *in vivo* delivery of antimicrobial peptides housed in 1 μm-diameter Cry3Aa crystals in BALB/c mice via intravenous injection, and observed consistent localization of Cry3Aa crystals to the liver, lungs, and kidneys, up to 24 hours post-injection.[10] A more recent study by Yang et al. from the same group demonstrated delivery of p53 protein to mammalian cells *in vitro* using a

modified version of Cry3Aa (dubbed Pos3Aa), which contained multiple lysine substitutions to increase the surface charge of the crystals. The Cry protein used to grow these crystals was fused to either mCherry fluorescent protein, or the p53 tumour-suppressing protein.[91] An additional justification for these mutations was based on ample evidence that uptake and endosomal escape are heavily dependent on the presence of numerous positively charged residues, such as lysine and arginine.[92–97] Independent staining of endosomes and crystals revealed that while cellular uptake occurred for both versions of Cry3Aa, endosomal escape into the cytoplasm was only observed for Pos3Aa crystals. Using different endocytic inhibitors, it was further observed that uptake was not receptor mediated, but instead occurred via macropinocytosis.[91] Crystals comprised of Pos3Aa-p53 fusion protein were able to sensitize mice to chemotherapy treatments, consistent with release and activity of p53 within the tumour cells. The results of this study demonstrate that LPCs can be engineered towards stable delivery of exogenous therapeutic proteins.

Outstanding questions related to the use of new LPCs in living systems include their potential cytotoxicity, immunogenicity, and their compatibility in vasculature, as previously mentioned. The question of cytotoxicity arises from both the potential toxicity of the scaffold protein, as well as the use of any reactive cross-linkers for stabilizing the crystals following synthesis. While our group has previously shown that large CJ crystals do not induce significant cytotoxicity,[44] and Cry protein crystals do not appear to be cytotoxic or haemolytic,[10] parasporins (also derived from *Bacillus thuringiensis*) display clear cytotoxicity against HeLa and HT-29 cancer cells.[98] This example emphasizes the importance of careful evaluation of the potential *in vivo* effect of each scaffold protein, as

well as consideration of possible carryover of undesirable bioactive substances (e.g. lipopolysaccharide and other endotoxins) from the host organism used to grow the crystals. The second question as to what extent protein crystals can negatively impact circulation is implicitly addressed in the Chan group studies; intravenous injection of mice with ~1 μm diameter crystals did not result in any apparent ill-effects on the mice.[10,91] Furthermore, as described in chapter 5 of this dissertation, no ill effects were observed on mice following intravenous injection of cross-linked CJ microcrystals.

1.2.3 Emerging applications

In addition to the aforementioned applications, LPC scaffolds have been utilized for a variety of niche applications, the majority of which are dependent on the unique properties of the protein itself. For instance, the CJ crystals that our lab routinely works with are able to rapidly adsorb nucleic acids to their interior,[30,99] and this property is currently being exploited by our group across multiple projects.

There is a precedent for the use of recombinant proteins in textile applications. Spider silk,[100,101] elastin,[102] resilin,[103,104] collagen,[105] fibroin,[106] and keratin[107] are all well-characterized structural proteins, and have been utilized in textiles in recent years, most commonly via electrospinning of individual fibres, or casting and self-assembly in foams and hydrogels. However, precisely controlled porosity is difficult in such systems. In pursuit of multifunctional textiles involving attachment of protein crystal depots, Hartje et al. from our group recently demonstrated integration of individual lysozyme and CJ crystals on bulk cotton, via chemical cross-linking with dihydrazides or dialdehydes, respectively.[108] The resulting crystals were able to adsorb guest sulforhodamine-labeled cytochrome P450 protein, although the activity of guest P450 enzyme was not tested.

Despite repeated laundering of the functionalized fabrics, at least 20% of the attached crystals were retained when chemically cross-linked to fabric.[108] Crystal retention might be improved via more robust chemical cross-linking;[108] additional strategies could involve *in situ* crystal growth on the surface of the fabric, which could reduce downstream handling and transfer of crystals. This approach may enable additional functionalization of cloth surfaces, particularly when combined with biosensing crystals or scaffolds which interact with specific pathogens.

Yet another novel application of LPCs is as a marker for mark-release-recapture (MRR) studies. It was previously demonstrated that CJ crystals were able to adsorb DNA to the crystal interior,[99] so Stuart et al. from our group synthesized CJ microcrystals loaded with a synthetic DNA marker; after saturating these microcrystals with DNA, they were deposited in tubs of stagnant water and allowed to incubate for several days alongside mosquito larvae.[99] Emerging adult mosquitoes were subsequently captured and reared in an insectary, whereupon they were sacrificed, and the original barcode sequence was recovered from the adult mosquitoes via qPCR-based detection and next-generation sequencing.[99] This study demonstrates a novel application of LPCs for marking and detection of mosquitoes, which have traditionally relied on fluorescent powders,[109] paints/dyes, or radioisotopes.[110]

1.3 Specific Aims

Large-pore protein crystals have emerged as promising biomaterials because they combine structural precision, high solvent content, and tunable pore architecture. However, several important questions remain unresolved. Although prior studies have demonstrated enzyme immobilization, guest loading, and modular functionalization in

protein crystal scaffolds, it is still not well understood whether such materials can be developed into practical biomedical platforms for macromolecular delivery, selective biological capture, and use in complex living environments. In particular, key gaps include the lack of data on nucleic acid loading and protection in large-pore protein microcrystals, the feasibility of reprogramming crystal scaffolds for selective capture of virion-sized targets, and the compatibility of these materials with *ex vivo* tissue and systemic *in vivo* exposure.

This dissertation addresses these gaps by evaluating cross-linked CJ porous microcrystals *in vitro*, *ex vivo*, and *in vivo* for different diagnostic, therapeutic, and biotechnological applications. Chapter 2 examines the loading, retention, conditional release, and pore-level protection of nucleic acid cargoes in CJ microcrystals. Chapter 3 engineers modular SpyCrystals for selective capture of virus-sized particles, including SARS-CoV-2 from wastewater. Chapter 4 evaluates the compatibility and guest-release behavior of CJ crystals in precision-cut lung slices as an ex vivo model of tissue response. Chapter 5 investigates biodistribution and persistence in vivo using bioluminescent trace-labeled CJ microcrystals. Collectively, these studies establish a framework for evaluating porous protein microcrystals as modular biomaterials for delivery, capture, and therapeutic scaffolding.

CHAPTER 2: Engineered Porous Protein Microcrystals as a Host Scaffold for Nucleic Acids

2.1 Overview

Contemporary gene therapies are constrained by a lack of diversity in delivery platforms. Various methodologies have been investigated for protecting DNA and RNA during delivery, but few can simultaneously protect guest nucleic acids, enable surface modification for tissue-specific targeting, and demonstrate high-capacity loading and containment. In this chapter, we describe the *in vitro* DNA adsorption and synthesis methods of CJ microcrystals. These crystals demonstrate a high potential capacity for guest macromolecules due to their high solvent content, and are able to rapidly concentrate a variety of nucleic acids; furthermore, the guest nucleic acids can be released via high adenosine triphosphate (ATP) concentrations. We identified batch crystallization conditions to synthesize uniformly sized CJ microcrystals and successfully loaded, retained, and conditionally released guest nucleic acids from the microcrystals under similar conditions. Furthermore, while guest DNA and RNA remained susceptible to cleavage by nucleases, we demonstrated protection of guest molecules via physical capping of the pores with a known hexamer protein complex. Due to their unique morphological characteristics, size, and the ability to protect guest DNA and RNA from nucleases, we anticipate that such porous protein microcrystals demonstrate potential for a variety of applications, including therapeutic delivery of guest DNA and RNA.

2.2 Introduction

A significant obstacle to the more widespread implementation of therapeutic RNA has been the lack of a robust delivery scaffold, owing primarily to the susceptibility of RNA to environmental degradation. Consequently, a wide variety of methodologies have been

investigated for encapsulating and protecting RNAs during delivery, including polymer nanoparticles[111], lipid-based nanoparticles[112,113], and exosomes[114–116]. However, few of these strategies can simultaneously confer protection of guest nucleic acids, demonstrate high-capacity loading, ensure stringent containment of the therapeutic agent, and enable modular surface modification of the vector to enable tissue-specific targeting.[117,118]

Protein crystals offer unique advantages as a potential therapeutic delivery vector, including a precisely defined nanostructure that does not vary with particle size, and the potential to optimize dose release based on size and shape[119–121]. Protein crystals also display more diverse morphological characteristics compared to traditional nanoparticles, liposomes, or exosomes. As described in chapter 1, CJ crystals consist of an array of large axial solvent channels (~13 nm diameter) across their hexagonal faces (Figure 2.1), which allows them to accommodate a wide range of guest molecules, including DNA, RNA, and proteins. CJ crystals have a high potential capacity for guest macromolecules due to their high solvent content, as well as high surface area-to-volume ratio.[122] After cross-linking, CJ crystals remain remarkably stable when transferred to new solution conditions. These crystals display the remarkable property of concentrating nucleic acids within the crystal volume. Furthermore, guest nucleic acids can be released via high adenosine triphosphate (ATP) concentrations, such as those found within the cytoplasm.[123,124] These characteristics position CJ crystals as a potentially unique therapeutic platform,

particularly as a delivery vector for nucleic acids.

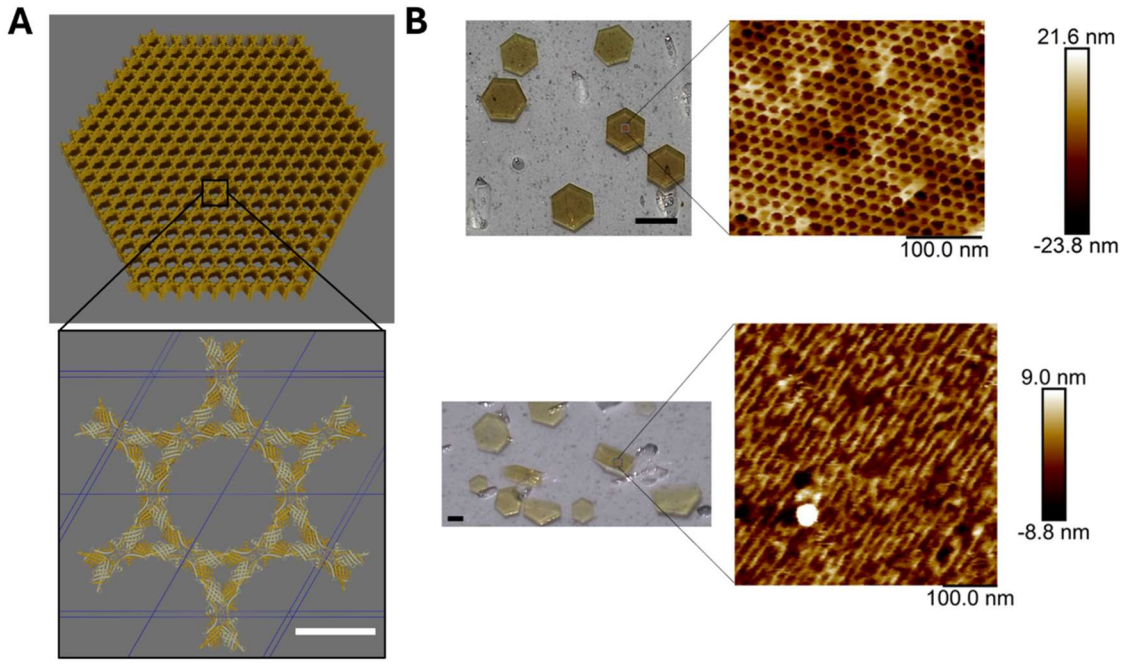

Figure 2.1: A, CJ forms a highly stable domain-swapped dimer, which crystallizes to form regular P 6 2 2 crystals (PDB: 5W17), characterized by large diameter (~13-14 nm) pores along their hexagonal face (scale bar = 100 Å). **B,** Atomic force microscopy (AFM) of cross-linked CJ crystals reveals the expected pore size and pattern along the hexagonal face (top), while half-channels are visible along the sides of the crystals (bottom) (scale bar = 0.5 mm in both images).

Previous work has demonstrated that rapid growth of sub-micrometer protein crystals is primarily influenced by total protein concentration, precipitant concentration, and pH;[33] the method for synthesizing CJ protein crystals used in this study was influenced by earlier studies which focused on batch crystallization of submicron lysozyme crystals.[33,125–127] Protein concentration in particular has been shown to dramatically influence both crystal size and the fraction of total protein crystallized. As demonstrated by Falkner et al., at protein concentrations greater than 8 mg mL^{-1}, lysozyme microcrystals measured less than 1 μm while displaying minimal morphological defects.[33] We tested similar batch crystallization conditions to favor smaller crystals, with protein concentration, salt concentration, and pH as independently tested parameters. In this chapter, we describe a reproducible method for synthesis of uniformly-sized CJ

microcrystals, and also demonstrate successful loading, retention, and conditional release of guest nucleic acids from the microcrystals under similar conditions. Due to their unique morphological characteristics and size, we anticipate that such porous protein microcrystals may demonstrate promising applications beyond therapeutic delivery of small RNAs, including pathogen biosensors, and as host scaffolds for enzymes.

2.3 Methods

2.3.1 Cloning, protein expression and purification

All primers used in this study were obtained from Integrated DNA Technologies. All chemicals used in protein expression, protein purification, crystal growth, crystal cross-linking, and buffer preparation were strictly ACS grade or higher (>95% purity). His-tagged CJ protein was expressed in BL21-DE(3) Gold cells, purified, and dialyzed as described previously[14–16]. The purified protein was concentrated using centrifugal concentrators (Amicon Ultra- 15, 10 kDa MWCO) to between 40 and 50 mg mL^{-1} in storage buffer (10 mM HEPES, 0.5 M ammonium sulfate, 10% glycerol, pH 7.4). The concentrated protein was then aliquoted and stored at -80 °C long-term.

The D2 domain of human NSF was amplified from cDNA from human blood. Total RNA was extracted from human blood with Monarch Total RNA Miniprep Kit (New England Biolabs, T2010); cDNA libraries were prepared via reverse transcription using SuperScript IV Synthesis Kit (Invitrogen, 18090010). The D2 domain from NSF was amplified by PCR (New England Biolabs, M0492L) with the following primers: NSF forward (5'-TTTTGTTTAACTTTAAGAAGGAGATATACAATGAAACCAGCCTTTGGCACAA-3') and NSF reverse (5'-

TCAGTGGTGGTGGTGGTGGCCGCCCTGAAAATACAGGTTTTCGCTGCCGC CTTCTCTTAAGAGGGCCAAGAATTT-3'). The resulting 828 bp amplicon was assembled in the pSB3 backbone via HiFi assembly (New England Biolabs, E2621S).

NSF cap protein was overexpressed in BL21-DE(3) Gold cells (Agilent, 200132) in 5 liters of TB media, supplemented with 50 mg mL^{-1}, in baffled shake flasks, at 25 °C, 250 RPM, over 30 hours. Cultures were induced at an optical density of ~0.8 with 0.4 mM isopropyl-1-thiogalactopyranoside (IPTG) (GoldBio, I2481C). Following induction and overexpression, cells were harvested by centrifugation, then resuspended and sonicated in lysis buffer (20 mM HEPES pH 7.0, 500 mM NaCl, 20 mM imidazole, 0.1 mM ATP, 1 mM $MgCl_2$, 5 mM tris(2-carboxyethyl)phosphine (TCEP)). After sonication, the lysate was clarified by centrifugation, and purified via metal-affinity chromatography with HisPur Ni-NTA resin (Thermo Fisher Scientific, 88221). NSF was subsequently eluted with a high-imidazole buffer (50 mM HEPES pH 7.4, 500 mM NaCl, 10% glycerol, 300 mM imidazole), and dialyzed for 12 hours at 4 °C in storage buffer (20 mM Tris pH 8.0, 0.1 mM ATP, 1 mM $MgCl_2$, 5 mM TCEP, 100 mM NaCl, 10% glycerol). After exchanging the buffer, NSF was dialyzed for an additional 12 hours at 4 °C. The resulting protein was concentrated via Amicon filtration, to a final concentration of approximately 5 mg mL^{-1}, as determined on a Qubit 4 fluorometer (Thermo Fisher Scientific, A51292). NSF cap aliquots were stored at -80 °C long-term.

2.3.2 CJ crystallization and cross-linking

Vapor diffusion plates were prepared with a range of salt concentrations (3.10 to 3.60 M ammonium sulfate) and two different pH values (100 mM Bis-Tris, pH 6.0 or 6.5). One µl of CJ protein (concentrated to 15 mg mL^{-1}) was combined with 1 µl of buffer from

each well; after sealing the wells, plates were incubated at room temperature for >24 h. Following crystal growth, crystals greater than 100 μm were individually looped and cross-linked with 1% glyoxal, as described previously.[11,34]

Batch crystallization of CJ microcrystals was performed by quickly adding 5 volumes of precipitant buffer (3.40 – 3.60 M ammonium sulfate, 100 mM Bis-Tris or HEPES, pH 7.0) with 1 volume of concentrated CJ protein (~40-50 mg mL^{-1}). The combined volume for each batch crystallization was between 240 μl and 720 μl. In most cases, the mixture became turbid and viscous almost instantaneously. Batches were then placed on a rotator and allowed to incubate at 4° C for 18-24 h. After crystallization, microcrystals were pelleted by centrifugation (2,000 g for 3:00 min). After removing the supernatant, the crystal pellets were resuspended in 0.5 mL of 4.2 M trimethylamine-N-oxide (TMAO), pH 7.5 by light vortexing. Crystals were allowed to soak for 5 minutes, then centrifuged and resuspended in fresh TMAO. This wash step was repeated once more. After washing, the crystals were resuspended in 1 mL of cross-linking buffer (4 M TMAO, 25 mM *p*-dimethylaminobenaldehyde (DMAB), 1% glyoxal), and incubated on a rotator at room temperature for 1 hour. The cross-linking reactions were then quenched in 1 M hydroxylamine, pH 5.0, with 100 mM DMAB, for 30 minutes. After quenching, the crystals were pelleted and resuspended in 1X PBS, pH 7.5, and stored at room temperature long-term.

2.3.3 Size, concentration, and measurement of guest loading in CJ microcrystals

Scanning electron microscopy was performed on a JEOL 6500 scanning electron microscope. Crystals were deposited on an aluminum substrate and dried under vacuum, gold sputtered to 10 nm thickness, and imaged with 15 kV beam. Dynamic light

scattering and zeta potential were measured using a Zetasizer Nano ZS (Malvern Panalytical). Tunable resistive pulse sensing was performed on a qNano Gold particle counter, using a nanopore suited for particles between 185 nm and 1100 nm (Izon Science, NP400).

For loading experiments, total CJ microcrystal concentrations (in crystals per milliliter) were determined using tunable resistive pulse sensing. pNZ052 plasmid DNA (6.0 kbp) was incubated with 10 μM DiYO-1 (AAT Bioquest) for 1 hour at room temperature. Following incubation, the resulting plasmid DNA was separated and washed by ethanol precipitation. To the 200 μL solution, 430 μL of 100% ethanol was added, followed by 70 μL of 3 M sodium acetate. The DNA-ethanol-salt mixture was then incubated overnight at -20 °C, then pelleted by centrifugation at 14,000 x g for 30 minutes. The resulting DNA pellet was washed twice with cold 80% ethanol, before drying and resuspending in 100 μL of nuclease-free water and storing at 4 °C for no more than 1 week.

Concentrated microcrystals were added to fluorescently labeled DNA, RNA, or DiYO-1-labeled plasmid DNA (in multiples of 5 μL, up to 25 μL), and incubated for 15 minutes at room temperature. The crystals were then pelleted by centrifugation at room temperature (2,000 x g for 3:00 minutes). The supernatant was transferred into a fresh microcentrifuge tube, then spun again at > 20,000 g for 5:00 minutes to remove any remaining microcrystals. The concentration of remaining DNA and RNA in the supernatant was then measured via fluorescence on a Synergy H1 multi-mode plate reader (BioTek), alongside a standard curve of known DNA and RNA concentrations. Alternatively, plasmid DNA was quantified by measuring absorbance at 260/280 nm. All

measurements were performed in triplicate; error bars indicate standard error from the mean.

For the time-based ladder loading experiments, 40 µL of cross-linked CJ microcrystals (containing ~4x10^7 microcrystals) was combined with 60 µL of O'Generuler 1 kbp pre-mix DNA ladder (Thermo Scientific, #SM1163); this mixture was then divided into 9 x 10 µL volumes. Each tube was then centrifuged for 2 minutes at 2,000 x g at a different time point (5, 10, 15, 30, 60, 120, 240, and 360 minutes post-mixing), and the resulting supernatant was pipetted into a fresh tube. The supernatants for each sample were subsequently run on a 1.0% agarose-TAE gel (containing Gel Red at a 1X concentration), at 11 V/cm for 90 minutes. Densitometry was performed using GelAnalyzer 19.1. Relative changes in band intensities were calculated by dividing the integrated peak areas of the bands in the samples by the integrated peak areas of the bands in the control lane (6 µL of DNA ladder, diluted to 10 µL with 1X TAE).

For the pH-based ladder loading experiments, 2 µL of crystals (~ 3.6 x 10^7 crystals per sample) were combined with 1 µL of one of the following buffers: 100 mM acetate buffer (pH 4 or pH 5), 1 M MES (pH 6), 1 M HEPES (pH 7 or pH 8), or 0.25 M CHES (pH 9) at room temperature for 30 minutes, before adding 7 µL of DNA ladder and incubating overnight at room temperature. After incubating, the crystals were pelleted by centrifugation as before, and 5 µL of the supernatant was run on an agarose gel as described above, alongside 5 µL of DNA ladder diluted 7:10 in TAE buffer.

For NSF cap protein loading, both large crystals and microcrystals were loaded as described previously.[34] In short, crystals were soaked for 30 minutes to overnight at room temperature in buffer A (50 mM HEPES, 300 mM NaCl, 10 mM nickel sulfate, 10%

glycerol, pH 7.5); after soaking, crystals were washed once in buffer A, sans nickel sulfate, before soaking in NSF cap (0.1 mg mL^{-1}) at 4 °C overnight. After soaking, the crystals were washed again in buffer A, sans nickel sulfate, to remove excess NSF protein.

2.3.4 Atomic force microscopy, hydrolysis testing, and confocal microscopy

Large cross-linked CJ crystals (> 0.1 mm diameter) were mounted and immobilized using double-sided tape, and imaged under buffer using atomic force microscopy, as described previously.[30]

Fluorescent DNA (5'-fluorescein-TATCTCCACCATCACCAAGCTTAGTACCCGGAATA-TAMRA-3') and RNA (5'-fluorescein-UAUCUCCACCAUCACCAAGCUUAGUACCCGGAAUA-TAMRA-3') hydrolysis probe oligonucleotides were purchased from Integrated DNA Technologies. Hydrolysis probes were loaded into CJ microcrystals by soaking for at least 15 minutes, then washing in 10 mM Tris, 1 mM EDTA, pH 8 for DNA or TE, pH 6 for RNA (RNase-free). For hydrolysis experiments, crystals were loaded with DNA or RNA FRET probes, then soaked in either NSF cap or 1X PBS, as described above. After washing, the crystals were transferred to a solution containing DNase I (Thermo Fisher Scientific, EN0521), at a final concentration of 0.1 mg mL^{-1}. After allowing the crystals and DNase to equilibrate at room temperature, DNase I buffer (Thermo Fisher Scientific, AM8170G) was added to the crystals. Immediately after addition of buffer, green fluorescence (λ_{Ex} = 490 nm / λ_{Em} = 530 nm) was measured via multi-mode plate reader for microcrystals, or *in situ* on an inverted spinning disk confocal microscope for large crystals. For the microscopy experiments, capped and uncapped crystals were imaged side-by-side, in the same buffer.

The same protocol was used for the RNA versions of these probes, except that RNase A (Thermo Fisher Scientific, EN0531) was added directly after beginning measurements or image acquisitions, and no additional buffer was added.

2.3.5 Image and software analysis, statistical analysis

Primers were designed using the Primer3 plugin for Geneious 9.1.8. Illustrations were generated in PyMOL (version 2.3.1) and Blender (version 4.1). Image editing and analysis, including LUTS configuration, color balance correction, normalization, and image scaling and cropping, was performed in Nikon NIS Elements, version 5.21.00 (Build 1483). Measurement of microcrystals in SE micrographs was performed manually using ImageJ 1.53t (FIJI).

Statistical analysis was performed using RStudio (R version 4.3.2, RStudio version 2023.12.0, Build 369) and Data Analysis ToolPak for Microsoft Excel (Version 2301). Single-factor ANOVA was used to evaluate statistical significance, with $p < 0.01$ considered a threshold for significance; unless otherwise noted, all error bars indicate the standard error from the mean.

2.4 Results

2.4.1 CJ microcrystals can be grown at sub-micron scales

Previous work has demonstrated that rapid growth of sub-micrometer protein crystals is primarily influenced by total protein concentration, precipitant concentration, and pH. The methods for synthesizing CJ protein crystals described in this chapter were inspired by earlier studies, which focused on batch crystallization of submicron lysozyme crystals[33]. In pursuit of conditions for reliable batch microcrystal growth, we optimized protein concentration, salt concentration, PEG concentration, and pH, as independent

variables. Initial screening for optimal salt concentration relied on larger crystals grown in sitting drop vapor-diffusion plates, where crystal size can be measured via brightfield microscopy.

After optimizing batch crystallization on the basis of pH, precipitant concentration, temperature, and PEG, we performed further optimization by varying protein concentration, and found this to be a more significant factor than the previous parameters. As microcrystal diameter decreases below 5 μm, it was no longer possible to quickly assess the crystal size via stereomicroscopy. Therefore, we turned to tunable resistive pulse sensing (TRPS), where the number and size of particles are assessed as they transit a pore. *A priori*, it was not clear how well this method would work for porous protein crystals since it relies on a temporary reduction in the flow of ions through the pore, and typical use has been for spherical particles that completely exclude counterions. Fortunately, so long as the solution conditions prevent microcrystal aggregation, suspensions of CJ microcrystals in phosphate-buffered saline generated TRPS data that was consistent with the expected crystal size distribution. After characterizing size distribution and concentration of glyoxal-cross-linked microcrystals using tunable resistive pulse sensing, we further validated these results by direct imaging using SEM (Figure 2.2A). One caveat of SEM is that this method relies on a vacuum and gold sputtering (approximately 10 nm). The combined effect of the vacuum and sputtering produces a "shrink wrap" effect where nano- and microcrystals aggregate, and the boundaries between the particles become less clearly defined. This effect is likely aggravated by the observed tendency of the microcrystals to flocculate at sufficiently high concentrations. Aggregation issues notwithstanding, crystal sizes obtained from SEM

images (Figure 2.2B), as measured individually in ImageJ, were consistent with dynamic light scattering (DLS) (Figure 2.2C) and tunable resistive pulse sensing (TRPS) data (Figure 2.2D) with respect to microcrystal diameter (mean diameter = 367 nm).

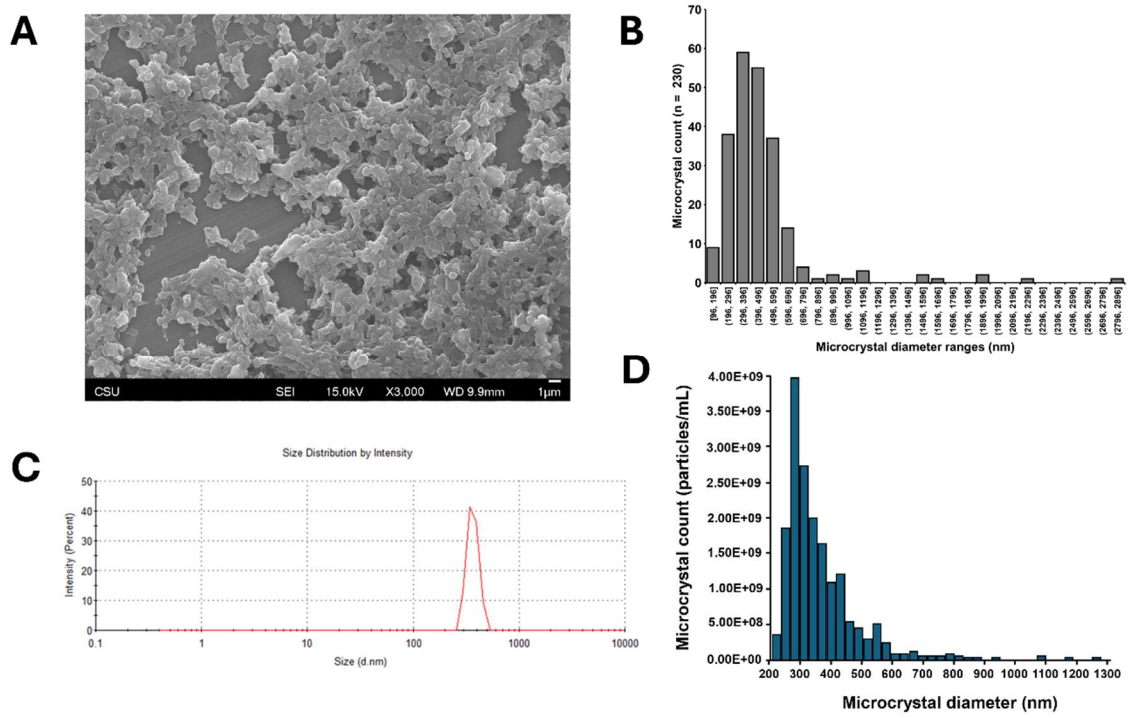

Figure 2.2: A, Representative SEM image of CJ microcrystals. Scale bar = 1 µm. **B,** Size distribution of crystals, as measured manually from multiple SE micrographs of the same crystal batch, using ImageJ (n = 230 microcrystals). **C,** Intensity vs. size for the same batch of microcrystals, as obtained using dynamic light scattering (DLS). **D,** Size distribution of the same microcrystals, as obtained using tunable resistive pulse sensing (TRPS).

2.4.2 Nucleic acid adsorption in CJ microcrystals is both time- and pH-dependent

After determining crystal size and concentration via tunable resistive pulse sensing (TRPS), we sought to test the RNA and DNA adsorptive capacity of CJ microcrystals by incubating increasing concentrations of crystals with fixed concentrations of FAM-labeled, 21-bp siRNA (300 nM), or 6.0 kbp plasmid DNA (~17.9 ng μL^{-1}, or 4.8 nM). As shown in Figures 2.3A and 2.3C, a linear increase in microcrystal concentration correlated with a linear decrease in supernatant concentration for both species, following a 30-minute incubation at room temperature. From this data, we were able to estimate the

number of siRNA or plasmid molecules adsorbed per microcrystal (14,900 ± 720 copies of siRNA, or 353 ± 80 copies of plasmid, per crystal). Incubation of microcrystals with DNA ladder pre-mix, and separating the crystals from the DNA at separate time points, revealed that the crystals preferentially adsorb smaller DNA fragments (Figure 2.3E,F). Loading of small RNA and plasmid DNA was likewise monitored via confocal fluorescence microscopy, using large CJ crystals. Overnight incubation of a large CJ crystal in TAMRA-labeled, 21-nt RNA resulted in near-saturation of the crystal (Figure 2.3B). Conversely, while overnight incubation of a large CJ crystal in DiYO-1-labeled plasmid DNA (~6.0 kbp) still resulted in adsorption to the crystal, capture of the plasmid

DNA was largely restricted to the crystal surface. (Figure 2.3D).

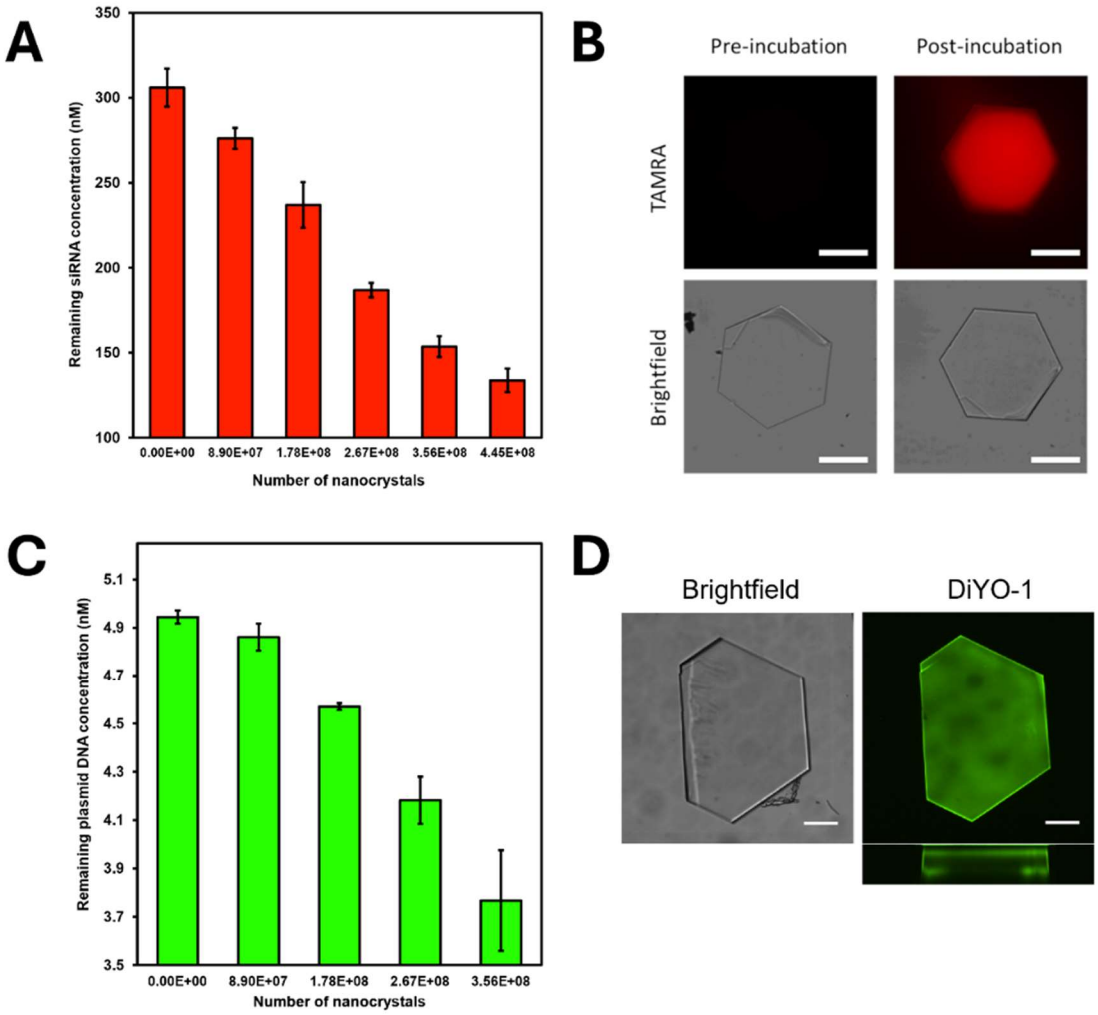

Figure 2.3: A, Supernatant concentrations of FAM-labeled siRNA, after incubating 300 nM siRNA with increasing concentrations of crystals (R2 = 0.988) (error bars = S.E.M.); **B,** Confocal fluorescence microscopy of a large CJ crystal, demonstrating loading of a TAMRA-labeled, 35 nt RNA; **C,** Supernatant concentrations of plasmid DNA, after incubating ~5 nM plasmid DNA with increasing concentrations of crystals (R2 = 0.954) (error bars = S.E.M.); **D,** Confocal fluorescence microscopy of a large crystal illustrating adsorption of DiYO-1-labeled plasmid DNA to the outer crystal surface, as shown via z-stack.

In addition to directly observing uptake of a variety of guest nucleic acids via confocal microscopy, we observed a similar pattern of uptake by CJ microcrystals using agarose gel electrophoresis of DNA fragments, which had been incubated with CJ microcrystals for different lengths of time, and at different pH values. We observed very rapid uptake of dsDNA fragments smaller than 500 bp (within 5 minutes), and almost complete uptake of

fragments 1 kbp and smaller after one hour (Figure 2.4A,B). Additionally, a clear pH dependence was observed using the same approach for crystals co-incubated with DNA at different pH values (pH 4, 5, 6, 7, 8, or 9) (Figure 2.4C,D), following overnight incubation; while there appears to be a modest reduction in uptake at pH < 5 or pH > 8, alkaline conditions appear to be much less favorable, with a large number of fragments remaining in the supernatant following incubation at pH 9.

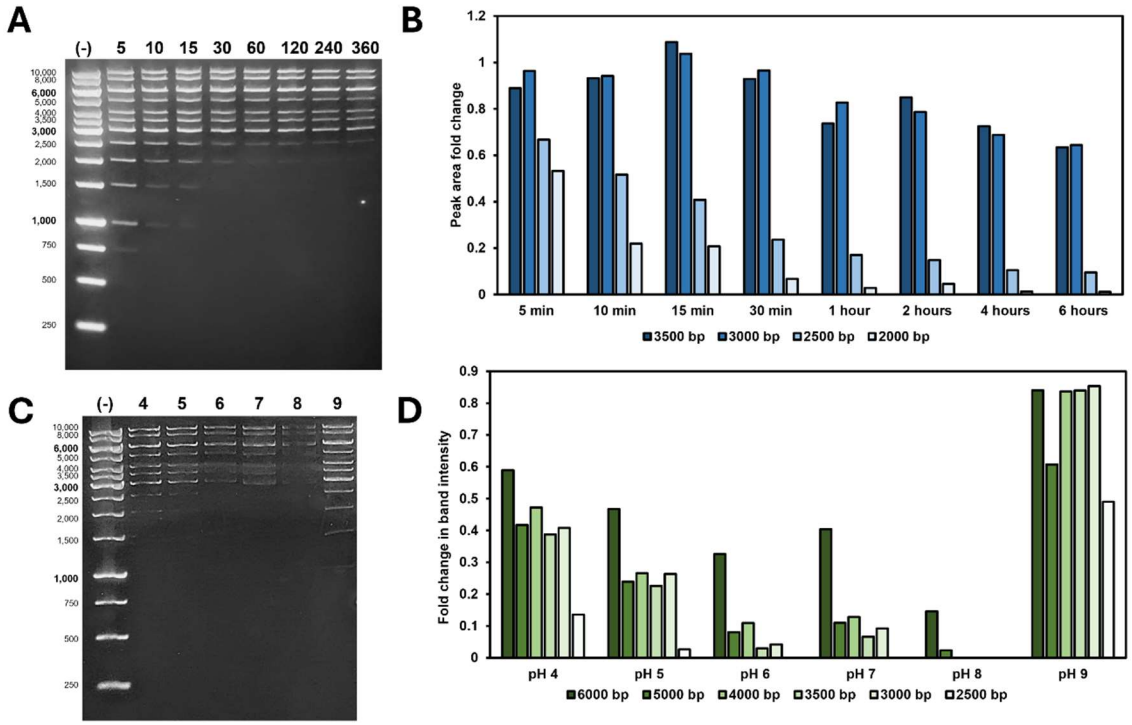

Figure 2.4: A, Gel electrophoresis of remaining DNA ladder fragments, following incubation with CJ microcrystals for 5 minutes to 6 hours. Incubation time (in minutes) is indicated above each lane. "(-)" indicates DNA ladder diluted with 1X TAE buffer in lieu of microcrystals. **B,** Densitometry graph showing relative fold-change in band intensity for 2000, 2500, 3000, and 3500 bp fragments, relative to the negative control, "(-)" at indicated time points. **C,** Gel electrophoresis of DNA ladder, following incubation with CJ microcrystals at different pH values (pH 4 to pH 9, indicated above gel). "(-)" indicates DNA ladder diluted with 1X TAE buffer in lieu of microcrystals. **D,** Densitometry graph showing relative fold-change in band intensity for 2500, 3000, 3500, 4000, 5000, and 6000 bp fragments, relative to the negative control, "(-)" at indicated time points.

2.4.3 Quantification of loading and release of guest DNA from large CJ crystals

While we have previously demonstrated uptake of guest nucleic acids and release via ATP wash in large CJ crystals, loading and release rate quantification has not been

reported. To address this, we designed and constructed a single-channel microfluidic flow cell, which permits continuous buffer exchange and *in situ* monitoring of individual crystals via confocal microscopy. Solutions containing guest molecules or ATP can be flowed over the crystal during imaging, using a paper pump. Using this approach, we were able to monitor loading of a 30-nt FAM-labeled ssDNA, and monitor release of the fluorescent guest DNA by flowing increasing concentrations of ATP over the crystal (Figure 2.5). Furthermore, we were able to measure relative fluorescence over time more quantitatively within a single crystal. Surprisingly, even when washed with very high ATP concentrations (40 mM, pH 6.0), the crystals consistently retained a measurable fraction of guest DNA, challenging our hypothesis that high ATP concentrations will always be sufficient for complete guest release. This result is consistent with a model of multiple modes of binding for single-stranded guests within the crystal pore, with variable affinity.

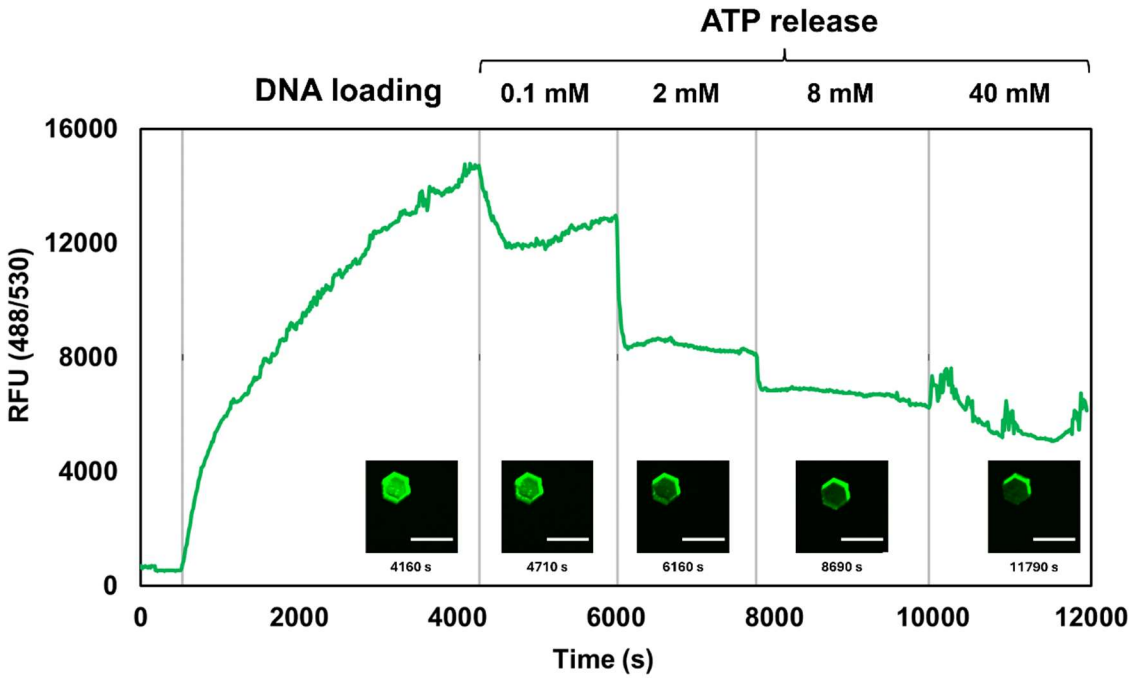

Figure 2.5: Direct imaging of a large CJ crystal loading during loading and release of a FAM-labeled ssDNA (30 nucleotide). Complete saturation of the crystal is observed after approximately 70 minutes. Release of guest DNA was performed by washing successively higher concentrations of ATP (up to 40 mM). Scale bars = 100 μm. Mean relative fluorescence values over the entire crystal face were obtained over the course of loading and ATP-mediated release. Different ATP concentrations are demarcated by gray lines on the graph.

2.4.4 Unmodified CJ pores can be protected from hydrolase activity via pore capping

For many applications, guest DNA and RNA within CJ microcrystals should remain protected from environmental insults. This is particularly salient in physiological settings, in which a number of environmental factors (including pH extremes and environmental nucleases) can promote hydrolysis of guest molecules. Examining the effect of environmental nucleases on guest DNA and RNA integrity was therefore deemed prudent.

We initially tested a RT-qPCR assay for quantifying guest RNA hydrolysis in microcrystals exposed to harsh conditions (exposure to nucleases and a range of different pH values). The assay involved two pairs of primers, each amplifying a small region (~150 bp) at separate ends of a long RNA (~1.8 kbp). Following exposure to hydrolyzing

conditions, the sample RNA was reverse transcribed using the reverse 3' primer, resulting in a mixed population of cDNAs of varying lengths. The sample is normalized in a downstream qPCR by measuring the number of intact 3' amplicons, and the number of intact 5' amplicons in the sample was used to calculate the relative fold change of intact RNA in the sample, using the ΔΔCt method (commonly used to measure relative changes in gene expression)[128]. Unfortunately, the RNA hydrolysis data obtained via RT-qPCR results proved difficult to reliably reproduce.

To monitor hydrolysis more directly inside the crystal, we instead relied on a FRET-based approach (Figure 2.6A). A 30-nt ssDNA probe containing a 5' FAM fluorophore and a 3' TAMRA fluorophore was used for these experiments. For the intact probe, the proximity of the two fluorophores in the intact molecule results in quenching of FAM emission (~520 nm), resulting in reduced green fluorescence when excited at 488 nm; however red fluorescence is still observable for the intact probe, as the emission maxima for the FRET interaction is around ~588 nm. Upon hydrolysis and separation of the two fluorophores, an increase in green fluorescence is observed. After loading this probe into a large CJ crystal, the crystal was excited with both 488 and 561 nm lasers and imaged under FITC (λ_{em} = 530 nm) and TRITC (λ_{em} = 575 nm) filters, respectively. After adding DNase I to a final concentration of 0.1 mg mL^{-1}, followed by addition of DNase I buffer after ~ 20 minutes, we observed a sudden increase in FAM fluorescence within the crystal, consistent with guest hydrolysis (Figure 2.6B). These results indicated that DNase I can function inside the crystals, and that at least a significant portion of the small ssDNA probe adopts a conformation that is susceptible to nuclease activity.

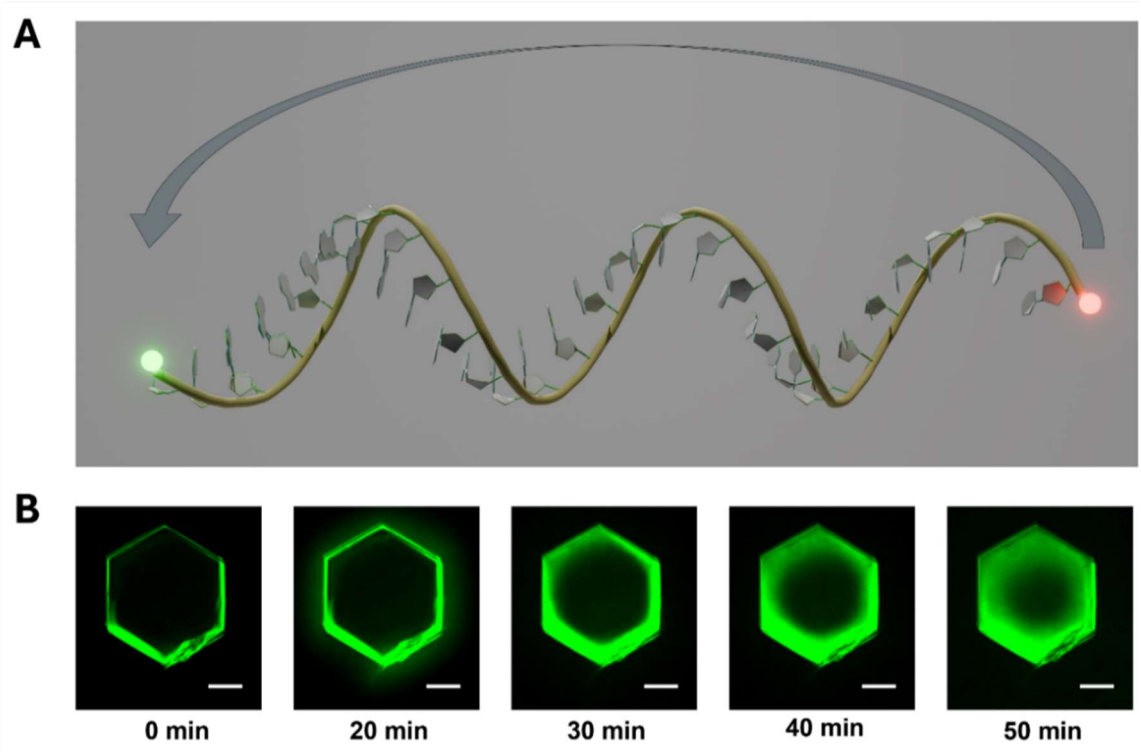

Figure 2.6: A, For an intact DNA oligonucleotide, green fluorescence from fluorescein attached to the 5' end of the molecule is quenched (blue arrow) by a TAMRA fluorophore at the 3' end. Following hydrolysis of the strand, both fluorophores are separated, and green fluorescence is no longer quenched and can be detected via spectroscopy or microscopy. **B,** Time series demonstrating hydrolysis of guest DNA by DNase I, following addition of DNase I buffer at approximately 20 minutes. Scale bar = 100 μm.

The results from the initial hydrolysis testing suggested that an alternative protection strategy was necessary. In particular, a suitably large "capping" protein complex was sought, which could potentially be modified to fit within the CJ pore, while preventing exogenous nucleases from entering the pore space. To this end, we vetted multiple structures within the Protein Databank. Two constraints were imposed on this search – namely, that the assembled structure form a stable hexamer, and that the diameter of the complex be within the range of 10 to 12 nm. The D2 domain from N-ethylmaleimide sensitive factor (NSF) was selected on the basis of these constraints (PDB: 1NSF) (Figure 2.7). NSF is a hexameric AAA ATPase, ubiquitously expressed in eukaryotes, and is primarily involved in membrane fusion via interaction with SNARE complexes.[129] The

D2 domain of NSF, in particular, has been shown to be responsible for the stability of the assembled hexamer, and has previously been reliably expressed in *E. coli*.[130]

We hypothesized that the assembled NSF cap hexamer could be installed in the CJ crystal pore via interactions between the histidine tags of the NSF cap with the histidine tags lining the CJ pore wall, as was previously demonstrated for guest Nanoluciferase (unpublished) and other enzymes.[34] Notably, this represents the first attempt to load CJ crystals with a protein oligomer. We hypothesize that the presentation of six histidine tags by the hexamer might significantly reduce the mobility of adsorbed guest due to avidity effects from 6 hexamer histags with 12 scaffold histidine tags per unit cell. Consistent with this hypothesis, confocal microscopy of CJ crystals incubated with sub-stoichiometric quantities of fluorescently labeled NSF showed a strong increase in the fluorescence of the crystal surfaces, but minimal fluorescence increases within the crystal

interior.

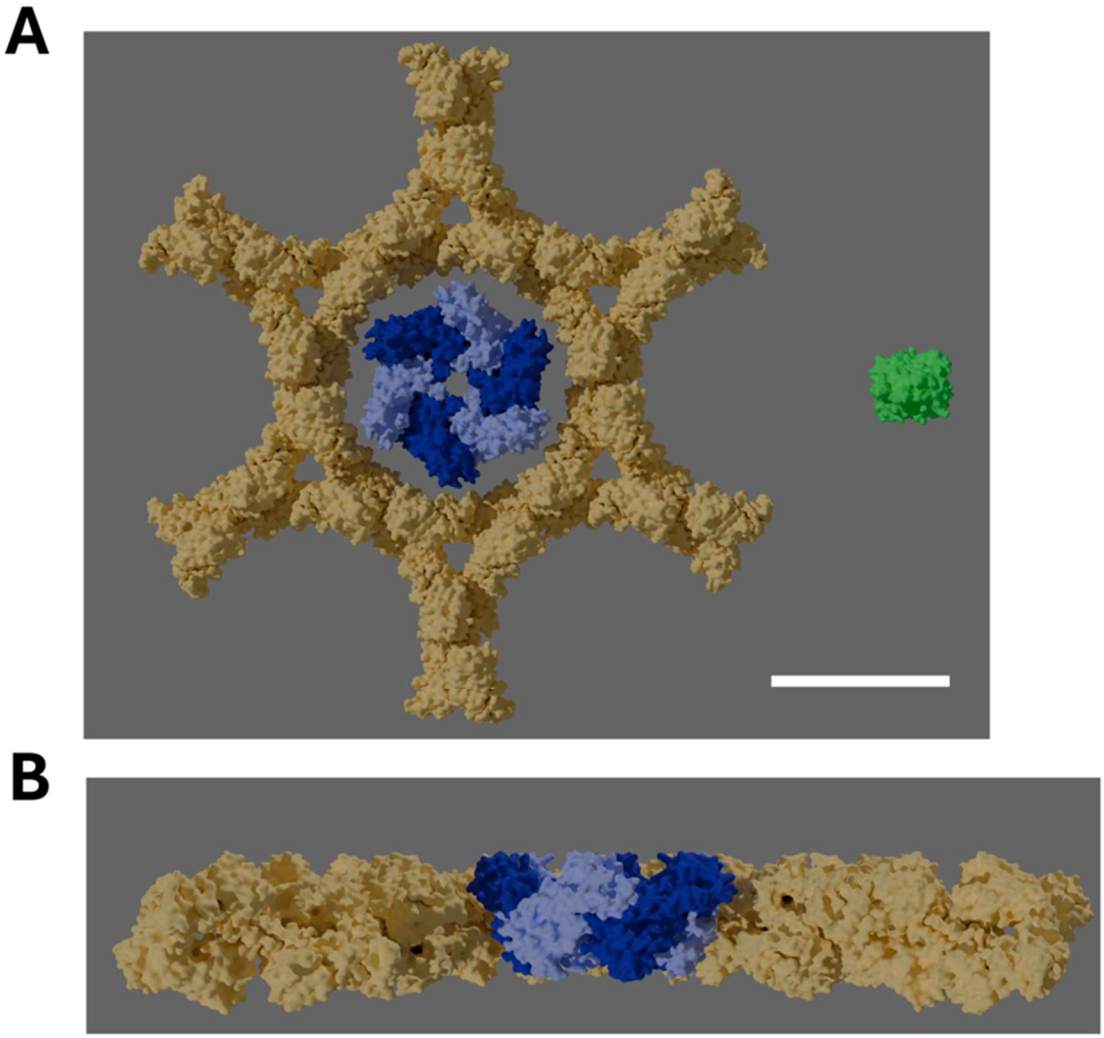

Figure 2.7: A, Size illustration of hexamer from the D2 domain from N-ethylmaleimide sensitive factor (NSF) (blue), relative to the major CJ pore (yellow), alongside a single DNase I monomer (green, PDB: 3DNI) (scale bar = 100 Å). The diameter of the assembled hexamer is ~ 110 Å, while the CJ pore is ~130 Å. The C-terminal polyhistidine tags of each NSF monomer align with the polyhistidine tags extending from CJ within the pore (not shown), allowing for non-covalent tethering of the cap protein via shared metal affinity. **B,** Profile view of NSF cap within the CJ pore; the assembled cap penetrates the pore to a depth of ~ 50 Å, or roughly one CJ unit cell.

We proceeded to attempt cap assembly *in vitro* via incubation of a large CJ crystal (pre-loaded with the aforementioned FRET-based hydrolysis DNA probe) with 0.1 mg mL^{-1} NSF. Via confocal microscopy of large CJ crystals, we observed a robust increase in fluorescence localized to the crystal, following incubation with NSF and DNase I.

Simultaneously, minimal hydrolysis was observed in the capped crystal, while the uncapped control crystal displayed the previously-observed green fluorescence, characteristic of successful hydrolysis (Figure 2.8A).

The same phenomenon was observed in microcrystals that were loaded with the hydrolysis probe, of which half were soaked in NSF cap protein overnight at room temperature; after washing both samples, fluorescence in both samples was monitored on a 96-well plate reader after adding RNase A (0.1 mg mL^{-1}, final concentration), over a 30 minute window. We observed a significant increase in FAM fluorescence across all replicates for the unprotected crystals within the first 5 minutes, along with a modest increase in fluorescence in the crystals capped with hexameric NSF (Figure 2.8B). Even after incubating a different batch of crystals for 1 hour, no statistical significance (as determined via single factor ANOVA) was observed between the capped crystals and the no RNase control ($p = 0.18$); conversely, a significant difference was observed between

the capped and uncapped crystals (p = 0.00046) (Figure 2.8C).

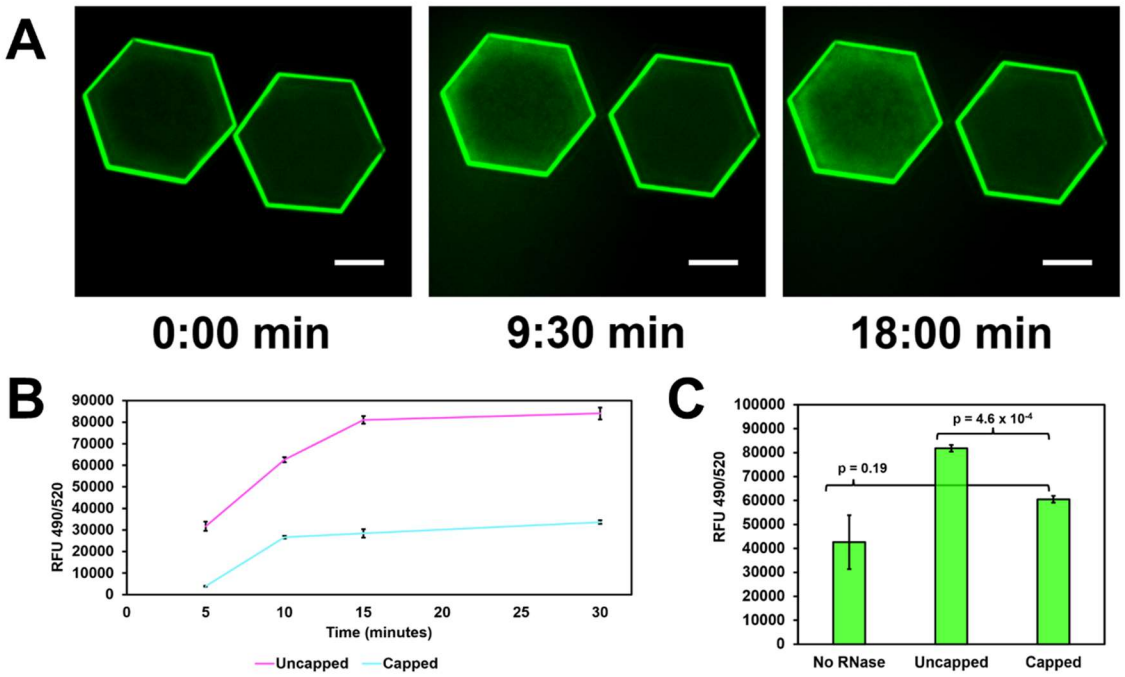

Figure 2.8: A, *In situ* visualization of DNA hydrolysis within a capped CJ crystal (right), compared to an uncapped control crystal (left), following incubation with DNase I, over 18 minutes. Scale bars = 100 μm. **B,** Guest RNA hydrolysis was observed in uncapped CJ microcrystals (magenta), but not in capped microcrystals (cyan), following incubation with RNase A over a 30-minute period (RNA in solution, without RNase A, is shown in blue). **C,** End point fluorescence (after 60 minutes) of capped and uncapped microcrystals loaded with FRET-labeled RNA.

2.5 Conclusions

In this chapter, we have demonstrated a successful and reproducible method for generating porous protein microcrystals from CJ protein, which recapitulate many of the unique phenomena associated with large CJ crystals - in particular, their ability to concentrate guest nucleic acids. Microcrystal size was verified using three different sizing techniques, which were all consistent for a single batch of microcrystals (Figure 2.2). Loading of microcrystals with fluorescently labeled guest DNA and RNA additionally demonstrates that size reduction does not impact their ability to concentrate nucleic acids (Figs. 2.3 and 2.4). On the contrary, it appears that reducing the size of the crystals by several orders of magnitude dramatically enhances the rate at which they deplete guest

biomolecules from the surrounding solution – while complete saturation of large crystals with DNA or RNA was observed on the order of 10 to 15 minutes, time-resolved loading of microcrystals with DNA ladder premix necessitated the addition of 10% glycerol by volume, in order to slow DNA diffusion and resolve the earliest time points. This is likely due to the increased net surface area to volume ratio associated with a large mass of submicron crystals, as opposed to a large individual crystal.[34,122,131] Additionally, we observed a modest pH dependence on nucleic acid uptake by the crystals, with significantly reduced capture observed at pH values greater than 8 (Figure 2.4C). While it is currently unclear what effect pH has on the mode of nucleic acid binding within the crystal, it is known that the C-terminal hexahistidine tags on CJ project to some degree into the pore interior, and histidine-rich peptides and proteins have been shown to interact with nucleic acids in a highly pH-dependent manner.[132–134] In order to evaluate the influence of the C-terminal histidine tags on DNA binding, we treated cross-linked CJ microcrystals with carboxypeptidase Y (labeled with NHS-Texas Red), prior to loading fluorescein-labeled DNA oligonucleotide, alongside untreated control crystals (labeled with NHS-Pacific Blue). Instead of reducing DNA binding, we observed that carboxypeptidase-treated microcrystals were able to load a greater amount of guest DNA than the untreated crystals, suggesting that, if anything, the histidine tags normally interfere with guest DNA binding (Supplemental figure 1). Additional structural investigations are required to determine the canonical mode of nucleic acid binding within CJ crystals, in order to ascertain the influence of pH on binding with any confidence.

An outstanding question remains as to how exactly DNA and RNA are able to bind to CJ crystals with such high affinity. Previous attempts at structure determination via X-ray diffraction of large crystals soaked in either ATP or DNA oligomer have proven inconclusive – while the crystals themselves continued to diffract at resolutions below 3 Å, consistent with previous XRD datasets,[11] no diffraction of guest DNA was observed anywhere within the structure, suggesting that guest DNA and RNA do not concentrate within the crystal in an orderly fashion. Beyond the unknown factors governing the nucleic acid-crystal interactions, it is also apparent (from attempts at loading large or supercoiled DNA) that guest size and secondary structures may be limiting factors for loading. Specifically, when we attempted to load fluorescently labeled plasmid DNA into a large CJ crystal, confocal microscopy revealed that the guest DNA did not penetrate through the interior of the crystal (Figure 2.3D). A similar size-based restriction phenomenon was observed from the gel densitometry results involving CJ microcrystals (Figure 2.3A,B). In that set of experiments, we observed a dramatic fold-reduction in band intensity for the smallest bands at the earliest time points (5- and 10-minutes post-mixing), while at later times (between 1- and 6-hours post-mixing), we began to see a reduction in band intensity for the larger bands (for bands between 3 and 5 kbp). While concentration of larger fragments to the interior of the crystal cannot be ruled out, it is plausible that larger DNA fragments may instead adsorb to the surface of the crystal.[135,136] Indeed, DNA adsorption to protein crystals was similarly observed with lysozyme microcrystals, albeit weakly (data not shown). Given that the major pore size of lysozyme crystals only measures about 17 Å,[137] it is likely that the DNA is bound strictly to the crystal surface. Notably, the estimated radius of supercoiled pUC18 (2.69 kbp) plasmid

can be as high as 8±1 nm.[138] It is therefore remarkable that microcrystals appear to successfully sequester the plasmids away from the supernatant, although it is possible that the pore geometry can constrain the supercoiled plasmid into adopting unusual superhelical pitch angles and plectonemic geometries.[139] This is the first report of a circular dsDNA guest within CJ crystals. To support the claim that plasmids can diffuse into the crystal interior (as opposed to adsorption to the crystal surfaces), we conducted confocal microscopy on a large crystal which had been soaked in DiYO-1-labeled pUC19 plasmid DNA. The resulting images suggest that plasmids are largely adsorbed to the outermost layers of the crystal (Figure 2.3D). Notably, the fluorescence in this case is limited to a zone approximately 16 μm thick at the crystal surface. This might indicate that plasmid uptake time is significantly longer than the time needed to uptake smaller dsDNA; alternatively, the observed limited uptake may be related to steric hindrance and limited diffusion due to size constraints.

In addition to end-point data, relative concentration of a fluorescently labeled guest DNA oligomer was measured in real-time, using a paper-pump driven microfluidic channel (Figure 2.5). We observed almost complete saturation of a ~50 μm CJ crystal after 70 minutes; additionally, we were able to demonstrate controlled release of the guest DNA by washing the crystal with increasing concentrations of ATP (0.1 mM to 40 mM) (Figure 2.5). Interestingly, at very high ATP concentrations (at or above 40 mM), we did not see further reduction in crystal fluorescence. Instead, fluctuations in fluorescence intensity were observed over the crystal, which may suggest that ATP temporarily displaces the guest DNA, only for the DNA to subsequently bind elsewhere within the crystal. Another possibility may be that multiple modes of binding exist between guest

nucleic acids and the CJ crystal, and that displacement by ATP may trigger re-binding elsewhere within the crystal. It is also possible that at very high ATP concentrations, weakly-bound guest DNA is displaced, but the 30-nt ssDNA probe remains bound at high affinity sites or kinetically trapped within the crystal. For example, if crystal nanopores have stochastic occlusions, small enough guest molecules might transit from an open axial nanopore into a closed axial nanopore via the small lateral pores. The irregularly sized lateral solvent channels are likely impenetrable to guests with a minimum diameter above 2 nm. However, a single-stranded guest could move laterally in x and y, albeit with a greatly reduced diffusion constant compared to movement via the 13 nm axial nanopores.

While the capture and concentration of DNA and RNA had until this point been well-known, it remained unclear to what extent the guest nucleic acids would remain protected against hydrolases. We initially sought to test this using a modified RT-qPCR-based assay; briefly, a 2.7 kb RNA was transcribed *in vitro*, and two primer pairs were designed to separately amplify ~150 bp regions at the 5' and 3' ends of the molecule. After soaking microcrystals in the RNA, the crystals were washed and transferred to a solution containing 0.1 mg mL^{-1} RNase A, and incubated overnight. The guest RNA was subsequently eluted by soaking the crystals in 20 mM ATP for 1 hour at room temperature, and after separating from the crystals, the RNA was added to a reverse transcriptase reaction, using a gene-specific primer. Due to the directionality of the reverse transcriptase, any cDNAs generated from RNAs which underwent hydrolysis would be truncated at the 5' end, and by comparing the ratios of 5' and 3' amplicons within a given sample, the relative extent of RNA hydrolysis can be quantified.

The above experimental approach proved difficult to reliably replicate, however, so an alternative strategy involving a FRET-based DNA or RNA oligomer was pursued instead. An additional advantage of using a fluorophore-quencher pair is that hydrolysis can be monitored *in situ* within both large and small CJ crystals. We designed a 35-mer DNA and RNA oligomer, containing both 5' fluorescein and 3' TAMRA fluorophores. Hydrolysis of this molecule results in loss of fluorescein quenching by TAMRA, correlating with an increase in green fluorescence. After saturating a large CJ crystal with the oligomer, and exposing the crystal to DNase I (0.1 mg mL^{-1}), we observed immediate hydrolysis of guest DNA within the crystal (Figure 2.6B). Based on this result, we developed a new strategy which relied on physically obstructing the pores of the crystal. The D2 domain from human N-ethylmaleimide sensitive factor (NSF) (PDB: 1NSF) was selected on the basis of its size and shape. After amplifying from human cDNA, and subcloning and expressing in *E. coli*, the purified NSF protein was incubated with one of two CJ crystals, which had both been soaked overnight in hydrolysis probe. After washing the NSF-soaked crystal, both crystals were imaged together in a solution containing DNase I. After adding DNase I buffer, we observed almost immediate hydrolysis in the un-capped CJ crystal, and little or no hydrolysis in the capped crystal (Figure 2.7C). This result was recapitulated using an RNA version of the same probe, in CJ microcrystals (Figure 2.8B,C). Further experimentation will be required to determine the extent to which NSF can accurately be envisioned as immobile caps for the CJ nanopores as opposed to simply serving as low mobility nanopore obstructing groups. However, significant evidence does suggest that the addition of NSF can dramatically reduce subsequent macromolecule transport into and out of the crystals.

More broadly, the results of this study demonstrate a number of unique practical properties for cross-linked protein microcrystals as a scaffold for biomolecules. Their ease of synthesis, diverse design space, and high surface area-to-volume ratio make them an attractive target for delivery of DNA and RNA in biological settings. Future implementation of specific affinity interactions, such as SpyCatcher/SpyTag[70,72], Barstar/Barnase[140], or streptavidin-biotin binding[141], may likewise expand the utility of porous CJ microcrystals towards increasingly diverse applications, including localized production of small molecules or installation of virus or cell-binding proteins.

CHAPTER 3: Porous Protein Crystals for Selective Adsorption of Viruses from Wastewater

3.1 Overview

Wastewater surveillance has become a critical tool for monitoring the prevalence and spread of viral pathogens at the community level. However, existing virus concentration methods—such as ultrafiltration, polyethylene glycol (PEG) precipitation, and charged membrane adsorption—often suffer from poor recovery efficiency, low specificity, or high operational costs, especially when viral loads are limited. To address these limitations, in this chapter we used CJ crystals modified with the SpyTag/SpyCatcher system to enable covalent and modular installation of viral binding domains. By incorporating high-affinity SARS-CoV-2 spike binders (P8, SpikePlug, and LCB1), the resulting "SpyCrystals" were designed to selectively adsorb viral particles from solution. We verified that as a proof of concept for surface capture guest installation, and that SpyCrystals efficiently covalently host SpyCatcher fusion proteins.

Whereas prior work with CJ crystals focused on the capture of guest molecules to the crystal interior, viral particles are too large to diffuse into the 13-nm diameter pores of the CJ crystals. Thus, we are pursuing a new capture mode that relies on capture of binding partners at the crystal surface. Since this is an unexplored application of CJ crystals, we began with a proof of concept for surface capture, demonstrating that biotinylated crystals can capture streptavidin-coated microspheres as a proof of concept for guest installation, and that SpyCrystals efficiently covalently host SpyCatcher fusion proteins. *In vitro* assays revealed strong adsorption of SARS-CoV-2 virions to SpyCrystals compared to unmodified controls, with subsequent enrichment of viral RNA following lysis. Integration of SpyCrystals into a tangential flow pump-filtration system enabled continuous scavenging of virus from wastewater, resulting in measurable

depletion of SARS-CoV-2 RNA in downstream flowthroughs. While conventional InnovaPrep concentration methods outperformed crystals in total virus recovery, functionalized SpyCrystals consistently exhibited specificity and capture efficiency over unmodified scaffolds. Together, these findings establish porous protein crystals as a promising modular platform for selective virus adsorption. Their adaptability to alternative binders highlights potential applications in wastewater epidemiology, point-of-care diagnostics, and multiplexed detection of emerging pathogens.

3.2 Introduction

Current gold standard assays for nucleic acid surveillance are predominantly quantitative PCR (qPCR) based, the best of which demonstrate limits of detection (LoD) as low as ~100 copies of nucleic acid per milliliter of sample.[142] Nevertheless, considerable variation in the limits of detection for approved assays can result in a substantial increase in false negative rates for every 10-fold increase in LoD.[142] Therefore, upstream methods that can concentrate potentially very small quantities of virus from a large volume of sample may dramatically reduce the rate of false negatives, while simultaneously increasing the limits of detection for less sensitive assays.

One of the primary challenges in enhancing the sensitivity of nucleic acid-based detection assays is the low abundance of viral particles in environmental or clinical samples. There currently exist a variety of concentration techniques that allow for the enrichment of viruses from large volumes of liquid. Some of the more common approaches include sucrose-gradient ultracentrifugation,[143,144] filtration-based methods,[144] and precipitation techniques, such as polyethylene glycol (PEG) precipitation.[144,145] Affinity-based methods, employing charged membranes, antibodies, or nucleic acid-binding materials have been explored to selectively capture and concentrate viruses. Despite their effectiveness, many of these methods are time-

intensive, require specialized equipment, or can introduce sample losses, limiting their practical utility for field-based or high-throughput applications.

In parallel, novel materials are being explored that can enhance capture of pathogens or virus components upstream of detection. Among these, metal-organic frameworks (MOFs) in particular have seen increasing attention. MOFs offer ultra-high surface areas, tunable porosity, and functionalization possibilities; recent work has demonstrated their capacity to capture nucleic acids and protect them from degradation in harsh environments.[146,147] For example, MOF functionalization has been shown to enable uptake and protection of ssDNA or mRNA, preserving integrity under serum exposure.[148] Similar to MOFs, protein crystals exhibit ordered, repetitive structures, which can enable dense, multivalent presentation of binding moieties. The SpyTag/SpyCatcher system has become a workhorse in protein engineering, enabling covalent linkage of proteins of interest onto scaffolds or nanoparticles with high fidelity and orientation control. Studies using SpyTag/SpyCatcher-mediated display have shown enhanced immunogenicity in vaccine contexts, and improved signal in biosensing assays when orientation and density of capture antibodies are optimized. CJ protein crystals possess unique structural and chemical characteristics, such as inherent biocompatibility and extremely high surface area-to-volume ratios, which make them amenable as a scaffold for capturing viruses and environmental nucleic acids (Figure 3.1A-C). As described earlier in chapter 2, one of the unique properties of these crystals is their ability to rapidly concentrate nucleic acids, which can subsequently be released at high ATP concentrations. Furthermore, CJ crystals can be engineered for greater guest modularity; by doping the crystals during growth with a CJ-SpyTag fusion protein, we are able to create a modular scaffold which can accommodate a variety of different SpyCatcher fusion guests. Originally developed by the Howarth lab, “SpyTag” is a 16 amino acid peptide,

containing an aspartic acid residue which reacts with a lysine residue on a 15.2 kDa protein, "SpyCatcher," to form an isopeptide amide bond. This system has been used for a multitude of applications, including enzyme immobilization,[54] antigen presentation,[149] and protein cyclization.[77] The crystals described in this chapter are comprised of roughly equimolar copies of the wild-type CJ protein, and CJ with a third-generation SpyTag variant ("SpyTag003") fused to the C-terminus.

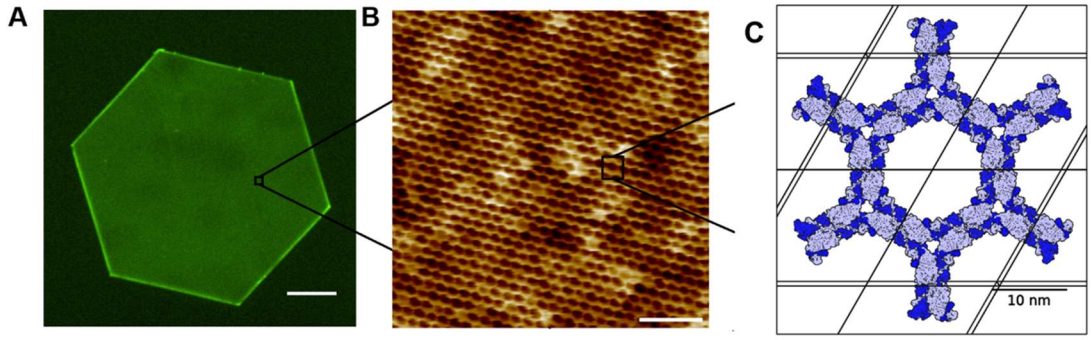

Figure 3.1: Overview of CJ crystal morphology. **A,** CJ crystallizes to form hexagonal P 6 2 2-space group crystals with large solvent channels (13-14 nm in diameter). The size and regularity of the pores can be observed via atomic force microscopy **(B)** and X-ray diffraction **(C)**. Scale bars are 100 μm (panel A), 100 nm (panel B), and 10 nm (panel C).

Parallel to modifying the crystals to display SpyTag, we additionally tested three different fusion proteins, consisting of third-generation SpyCatcher fused to a human ACE2 receptor mimic. Karoyan et al. previously designed a number of small helical proteins mimicking the N-terminal helical domain of hACE2, using a combined computational and rational design strategy;[150] the reported peptide with highest binding affinity (k_d = 24 nM), "P8," was selected for this study. The second guest protein, "SpikePlug," was originally designed by Romano et al. by extracting the ACE2 receptor's key binding helices (H1 and H2), stabilizing them with an additional helix (H3), and introducing further mutations to enhance structural stability and solubility; the reported dissociation constant for SpikePlug was 40 nM.[151] For the third and final guest, we selected "LCB1," developed by Cao et al. from the Baker lab. LCB1 was originally

designed by employing *de novo* computational methods to create a 56-amino-acid miniprotein that binds with high affinity to the receptor-binding domain (RBD) of the SARS-CoV-2 spike protein, effectively blocking its interaction with the human ACE2 receptor and thereby inhibiting viral entry into host cells; the reported dissociation constant was ~0.1 nM.[152]

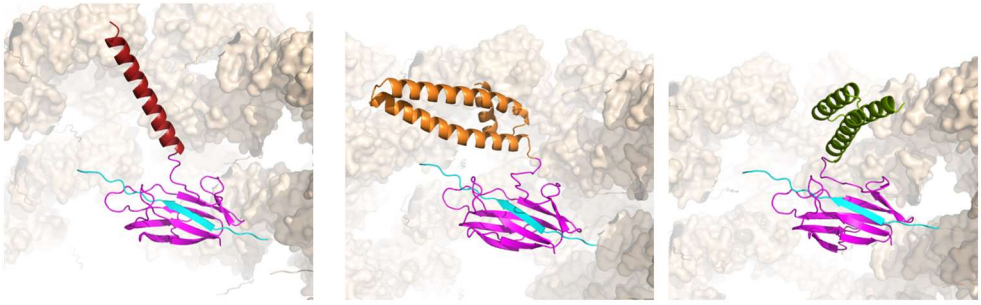

Name	P8	SpikePlug	LCB1
Affinity	24 nM	40 nM	0.1 nM
Reference	Karoyan	Romano	Baker

Figure 3.2: SpyCatcher-spike binder fusion proteins used in this study. SpyCatcher003 (magenta) is fused to the N terminus of one of three known spike binders – P8 (red), SpikePlug (orange), or LCB1 (green). The reported dissociation constant associated with each spike binder is shown in the table below.

As a proof of concept for using the crystals for virus capture, we demonstrate that biotinylated CJ crystals are able to selectively capture streptavidin-coated microspheres. Furthermore, we have demonstrated that crystals modified to covalently host SpyCatcher-SpikeBinder fusion proteins are able to bind SARS-CoV-2 virions with greater affinity than unmodified crystals. This platform was further integrated into a pump housing and upstream tangential flow filter to allow continuous scavenging and concentration of virus spiked into wastewater. Using this system, we observed a significant depletion of SARS-CoV-2 virions from the wastewater using columns containing spike binder-hosting crystals, when compared to columns housing unmodified control crystals. The results described in this chapter strongly suggest that porous protein crystals can serve as a matrix for selective adsorption of viruses or virus-sized particles via specific high-affinity interactions.

3.3 Methods

3.3.1 CJ and CJ-SpyTag003 expression, purification, crystallization, and cross-linking

Wild-type CJ and CJ-SpyTag003 proteins were expressed and purified using a shake flask expression, as described previously.[9,34,153] Following shake flask expression and column purification, CJ-SpyCrystals were synthesized using a batch crystallization method. Briefly, one volume of concentrated CJ protein + CJ-SpyTag003 protein (equimolar concentration) was combined with five volumes of precipitant buffer (3.5 M ammonium sulfate, 100 mM HEPES, pH 7.0) in a single 1.5-mL microcentrifuge tube. The crystals were allowed to grow at room temperature for 24 hours. Following growth, the crystals were pelleted by centrifugation (2,000 x g for 5 minutes), then washed in 4.2 M trimethylamine-N-oxide (TMAO) and then resuspended in a cross-linking buffer (1% glyoxal, 25 mM p-dimethylaminobenzaldehyde (DMAB), and 4 M TMAO) and incubated at room temperature for 15 minutes. The cross-linking reaction was then quenched via washing the crystals in 1 M hydroxylamine, 25 mM DMAB for 1 hour. Biotinylated crystals were prepared by supplementing the cross-linking buffer with 100 mM biotin (final concentration) and cross-linking with 40 mg mL^{-1} 1-ethyl-3-(3-dimethylaminopropyl)carbodiimide (EDAC) dissolved in 4.2 M TMAO for 24 hours, before quenching with 50 mM sodium borate, pH 10.

3.3.2 Capture of streptavidin-coated microspheres by biotinylated microcrystals

Fluorescent, 0.04 μm, streptavidin-labelled microspheres (TransFluoSpheres™, Thermo Fisher, #T10711) were diluted 10,000-fold in 1X PBS (final volume, 50 mL). Meanwhile, CJ-SpyCrystals were diluted to 10 mg mL^{-1} in 4.2 M TMAO, with or without 100 mM biotin, and cross-linked with EDAC as described above. Following cross-linking and quenching, the biotinylated and unbiotinylated crystals were added to separate 1.0 x 5.0 cm gravity columns

(Bio-Rad #7371007EDU), each washed with 3 column volumes of 1X PBS, and 50 mL of the diluted microspheres were flowed over the packed crystal beds. These experiments were performed in triplicate. Following loading, the crystals were washed with 5 mL of 1X PBS, three times. The flow through from each wash was collected for each column, and the fluorescence for each fraction was measured on a 96-well plate reader (λ_{ex} = 488 nm, λ_{em} = 645 nm).

3.3.3 Expression and purification of SpyCatcher-SpikeBinder fusion proteins

The plasmids pET21-SpyCatcher003-P8, pET21-SpyCatcher003-SpikePlug, and pET21-SpyCatcher003-LCB1 were designed and ordered from Twist Biosciences, while pJ404-SpyCatcher003-sfGFP was obtained from AddGene repository (Plasmid #133449), and all were transformed via heat shock into BL21(DE3) Gold competent *E. coli* cells (NEB, #C2527H). Liquid cultures were grown to an O.D. of ~0.6, and expression was induced with 0.4 mM isopropyl-beta-D-thiogalactopyranoside (IPTG). Following induction, cultures were incubated at 25 °C, with shaking at 250 RPM, for 30 hours. The cells were subsequently pelleted via centrifugation at 12,000 g, and the cells were resuspended in 1X PBS, pH 7.5, before sonicating for 5.00 min process time (10 s ON, 30 s OFF). The resulting lysate was clarified via centrifugation, before storing at -30 °C long-term.

3.3.4 CJ-SpyCrystal guest loading, in vitro capture, and pump integration

For the *in vitro* experiments, 2 milligram aliquots of CJ microcrystals were separately soaked in 1X PBS, SpyCatcher-P8, SpyCatcher-SpikePlug, or SpyCatcher-LCB1 lysate (each supplemented with 0.1 μg mL^{-1} of SpyCatcher-sfGFP), and subsequently washed via three solution exchanges of 1X PBS, pH 7.5. The weights of the crystal pellets were measured by difference, and crystals were resuspended to a final concentration of ~2.0 mg mL^{-1}. Crystal concentrations were further normalized via sfGFP fluorescence.

For testing *in vitro* capture, 0.1 mL from each of the four batches of microcrystals (SpyCatcher-sfGFP, SpyCatcher-P8, SpyCatcher-SpikePlug, or SpyCatcher-LCB1) were separately combined with 100 µL inactivated SARS-CoV-2 virions, provided by Dr. Raymond Goodrich and Darragh Heaslip of BIOMARC, diluted to ~1.5 million virions/µL. The crystals were then incubated at 4 °C for 4 hours, before pelleting the crystals at 2,600 g for 5 minutes. Five microliters of supernatant from each were separately mixed with 5 µL of SARS-CoV-2 lysis buffer, using a previously described protocol,[154] and incubated at room temperature for 15 minutes, before diluting 100-fold. The pelleted crystals were likewise washed twice with 1X PBS, pH 7.5, before resuspending in 100 µL of 1X PBS and 100 µL of SARS-CoV-2 lysis buffer and incubated at room temperature for 15 minutes, then diluted 100-fold.

For testing in the tangential flow filter, microcrystals were resuspended to a concentration of approximately 20 mg mL^{-1}, and 0.1 mL of naïve CJ-SpyCrystals were added to separate G-Trap™ 1ml FliQ FPLC columns (G-Biosciences, #786-1292), along with 0.4 mL of stripped NTA resin (Thermo Fisher, #88221). A total of 12 columns were prepared in this way (3 experimental replicates, times 4 guest proteins). For loading Spikebinders, each column was then connected to the outlet of a LifeStraw® filter, used for prefiltering, and flow through the filters was driven by an Arduino-controlled pump. PBS buffer was then pumped through each column for 1 minute at a rate of 50 mL/min, before pumping either 50 mL of 1X PBS, pH 7.5, or 50 mL of sonicated expression lysate (from SpyCatcher-P8, -SpikePlug, or -LCB1), at 1 mL/min. Following loading, all columns were washed with 50 mL of 1X PBS. Then, wastewater spiked with inactivated SARS-CoV-2 virus (1:1000 dilution) was pumped through each set of columns in succession. The sequence for each set of columns was as follows: Guest loading for replicates 1, 2, and 3, followed by PBS wash for replicates 1, 2, and 3, followed by wastewater pumping

for replicates 1, 2, and 3. Triplicates were run in the following order: control crystals, SpyCatcher-P8, SpikePlug triplicates,-LCB1. Fifty milliliters of wastewater were pumped through each set of columns at ~1 mL/min and collected in 50-mL conical tubes, then stored at -20 °C, until further processing. After wastewater tests, the crystals were removed from each column and were diluted to 0.7 mL with 1X PBS and resuspended by pipetting; 500 µL from each test were transferred to fresh 1.5 mL tubes, centrifuged at 2,600 g for 5 minutes, and the supernatant was replaced with 100 µL of 1X PBS, followed by 100 µL of viral lysis buffer. The crystals were incubated at room temperature for 15 minutes, before pelleting again and collecting the supernatant for use in downstream PCR.

Samples were subsequently diluted 2-fold in SARS-CoV-2 lysis buffer and incubated at room temperature for 15 minutes, before diluting 10-fold in nuclease-free water for RT-ddPCR. Samples of each wastewater flowthrough were diluted an additional 20-fold prior to RT-ddPCR.

3.3.5 Reverse transcription droplet digital PCR (RT-ddPCR)

RT-ddPCR was performed using One-Step RT-ddPCR Advanced Kit for Probes (Bio-Rad #1864021) for all samples, as well as positive (stock virus diluted 100-fold) and negative (nuclease-free water) control reactions. The master mix contained the following, per reaction: 2.55 µL nuclease-free water, 1.65 µL SARS-CoV-2 N1 primer/probe mix, 5.5 µL supermix, 1.1 µL 300 mM dithiothreitol (DTT), and 2.2 µL reverse transcriptase. After combining 13 µL of master mix with 9 µL of sample, 20 µL of each assembled reaction were combined with 70 µL of automated droplet generation oil (Bio-Rad #1864110) in DG32 droplet generation cartridges (Bio-Rad # 1864108), and the resulting droplets were transferred to separate wells in a 96-well plate. Plates were then sealed, and thermocycling was performed under the following conditions: 50 °C for 60 minutes, 95 °C for 10 minutes, followed by 44 cycles of 94 °C for 30 seconds,

followed by 55 °C for 1 minute. Cycling was followed by final denaturation at 98 °C for 10 minutes, and then held at 4 °C. Droplets were then read on a Bio-Rad QX200 droplet reader, and the fluorescence threshold across all wells was manually set to an amplitude of 2,000 units.

3.3.6 Microscopy

A large cross-linked CJ-SpyCrystal (> 0.1 mm diameter) was soaked overnight in SpyCatcher-LCB1 (0.1 mg mL^{-1}), then washed in 1X PBS and immobilized using marine-grade double-sided mounting tape. The crystal was imaged under buffer using a Bruker atomic force microscope as described previously[30,63], following addition of inactivated SARS-CoV-2 virus (to a final concentration of ~ 5.0 x 10^4 virions mL^{-1}). The soaked crystal was imaged alongside a wild-type CJ crystal. Scanning electron microscopy was performed as described previously.

3.3.7 Data analysis and statistics

Statistical analysis was performed using RStudio (R version 4.3.2, RStudio version 2023.12.0, Build 369). Single-factor ANOVA was used to evaluate statistical significance, with $p < 0.01$ considered a threshold for significance; unless otherwise noted, all error bars indicate the standard error from the mean.

3.4 Results

3.4.1 Biotinylated CJ crystals are able to capture streptavidin-coated particles to their surface

As a proof of concept, CJ crystals were chemically cross-linked with biotin, and then exposed to streptavidin-coated, fluorescent microspheres, to verify the crystals' capacity to bind a target guest via a specific, high-affinity, and non-covalent interaction (Figure 3.3A). After cross-linking biotin to the surface of large (> 0.1 mm diameter) CJ crystals, we observed preferential localization of streptavidin-coated beads to the biotinylated crystal, compared to an

unbiotinylated control crystal imaged alongside it (Figure 3.3B). Additionally, after cross-linking CJ microcrystals (< 20 µm diameter) with biotin, and loading those crystals into a gravity column, we observed capture of the same microspheres by columns containing the biotinylated microcrystals, but not by columns containing unbiotinylated crystals, by comparing fluorescence of 5-mL flow-through fractions for both columns. We observed extremely high fluorescence in the first flow-through fraction for the unbiotinylated microcrystals, while fluorescence was much lower in the first two flow-through fractions for the biotinylated crystal columns, suggesting the microspheres were retained more strongly by the biotinylated crystals. The third flow-through fraction for the biotinylated crystal column displayed a roughly three-fold increase in fluorescence, compared to the first two washes. After performing the washes, the crystals in each column were diluted to the same approximate volume (1.0 mL in 1X PBS), and fluorescence measurements of each set of crystals revealed a consistently higher relative fluorescence in the biotinylated microcrystals, versus the unbiotinylated crystals (Figure 3.4B). These experimental results demonstrate that CJ crystals can be modified to selectively entrap virus-sized particles.

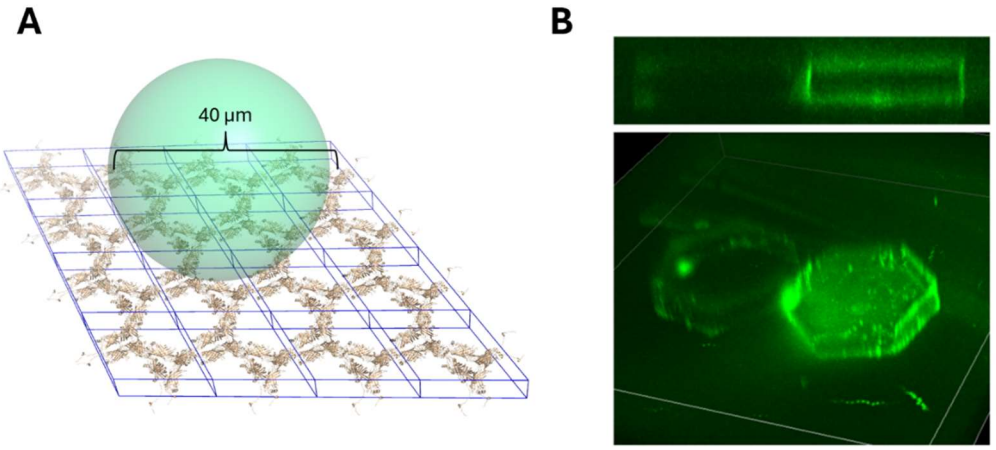

Figure 3.3: A, Diagram illustrating putative interactions between a streptavidin-coated microsphere (green) and the biotinylated surface of a CJ crystal pore (beige). **B,** Confocal fluorescence microscopy reveals preferential localization of streptavidin-coated microspheres to the surface of biotinylated CJ crystals, but not to the unbiotinylated crystals, when incubated in the same solution.

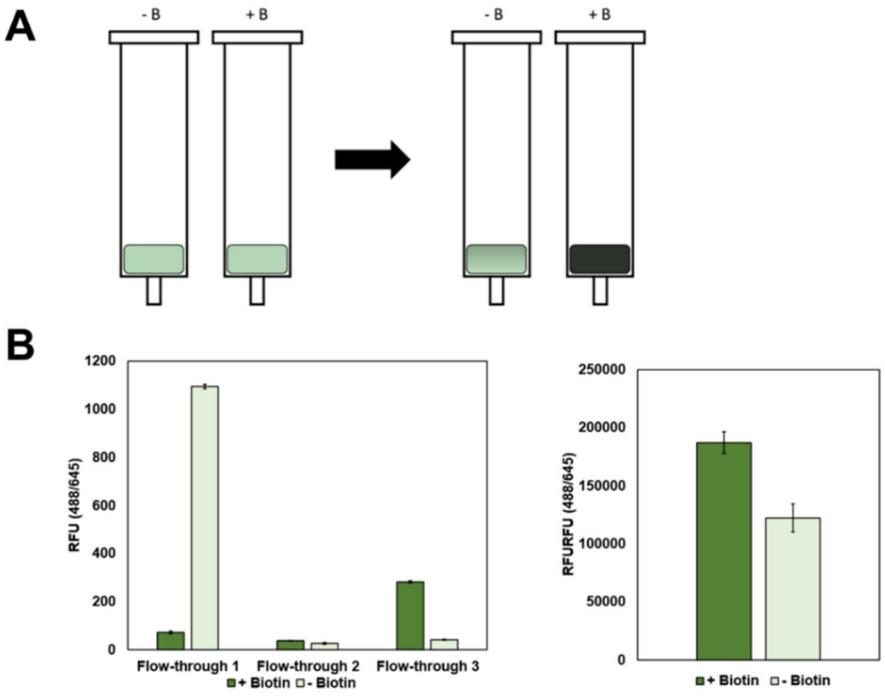

Figure 3.4: A, Schematic of gravity column experiments, in which two columns, one containing unbiotinylated microcrystals ("- B") and another containing biotinylated crystals ("+ B"), are each "fed" a solution containing 0.04 μm, fluorescently-labelled, streptavidin-coated microspheres. **B, Left**: Relative fluorescence of 5 mL flow-through fractions during washing (and following loading) for columns with biotinylated or unbiotinylated microcrystals. **Right**: Relative fluorescence of biotinylated and unbiotinylated microcrystals, following washing and dilution. RFU indicates relative fluorescence units.

3.4.2 SpyCrystals are able to host fusion guest proteins via covalent interactions

As a means of introducing increased guest modularity, CJ crystal growth was modified via introduction of an additional protein, CJ-SpyTag003, which contains a C-terminal SpyTag, at a lower molar fraction than wild-type CJ. Co-crystallization of CJ with CJ-SpyTag003 under these conditions results in the growth of a chimeric co-crystal, which is predominantly composed of wild-type CJ, with SpyTag periodically projecting into the pore space. As a result of SpyTag's accessibility near the wall of the 13 nm major pore, guest SpyCatcher fusion proteins can be rapidly and irreversibly installed, permitting the installation of an unlimited number of possible binding proteins within the same scaffold matrix.

This approach was tested first using a SpyCatcher-GFP fusion protein (Figure 3.5A). In order to validate guest covalent capture, a large (>0.1 mm diameter) CJ-SpyTag003-doped CJ crystal ("SpyCrystal") was grown via sitting-drop vapor diffusion. After growth, both the SpyCrystal and a wild-type CJ crystal were cross-linked with 1% glyoxal, then soaked overnight at room temperature in SpyCatcher-sfGFP (10 µg mL^{-1}, diluted in 1X PBS and 100 mM EDTA). After soaking, both crystals were soaked 3 times, over 3 days, in 1X PBS, 100 mM EDTA, to wash away any uncaptured fluorescent protein. The crystals were imaged side-by-side via confocal fluorescence microscopy before loading, and after the final washing. As shown in Figure 3.5B, localization of SpyCatcher-sfGFP was observed exclusively in the SpyCrystal, but not the wild-type crystal, demonstrating covalent installation of guest SpyCatcher fusion proteins.

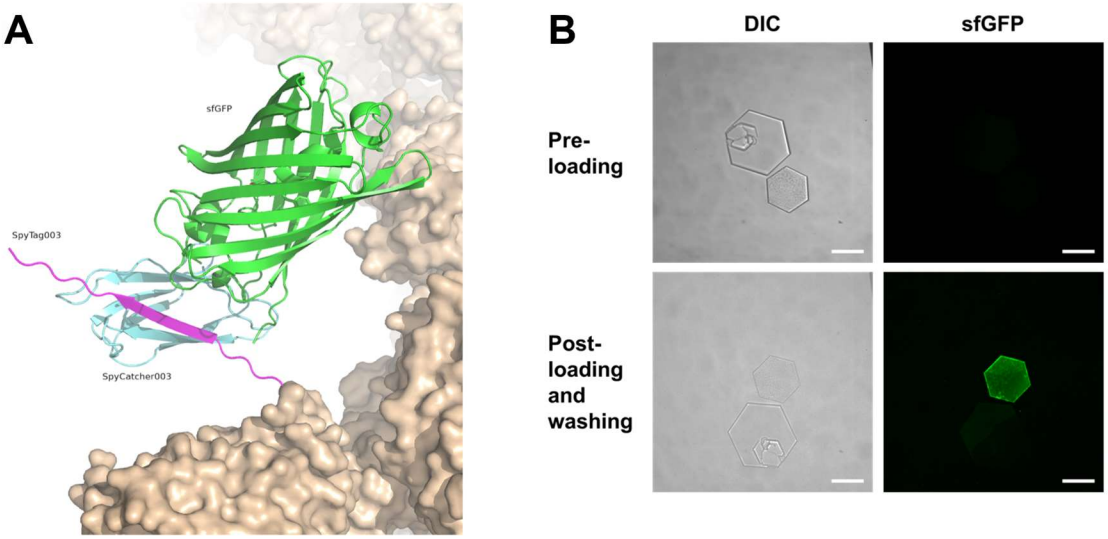

Figure 3.5: A, Putative covalent interaction between SpyCatcher-sfGFP (SpyCatcher in cyan, sfGFP in green), and the pore wall of a SpyTag-doped CJ crystal ("SpyCrystal") (SpyTag in magenta, CJ in beige). **B,** Capture of guest SpyCatcher-sfGFP by a SpyCrystal, imaged alongside an undoped wild-type CJ crystal.

3.4.3 Modified CJ-SpyCrystals adsorb virions *in vitro*, and release viral RNA following lysis

After confirming that CJ microcrystals were capable of capturing virus-sized particles on their surface, and that introducing SpyTag003 to the crystal structure enabled the capture of SpyCatcher-fused guest proteins, we next sought to visualize localization of SARS-CoV-2

virions to the surface of a modified SpyCrystal, using atomic force microscopy. Two large SpyCrystals (> 0.1 mm) were grown under identical conditions, and one was soaked in SpyCatcher-LCB1. After soaking, the latter crystal was washed in PBS, mounted alongside the unmodified crystal using double-sided tape. Inactivated SARS-CoV-2 virions were then added to the immersed crystals (to a final concentration of approximately 5.0 x 10^4 virions μL^{-1}), then washed twice with PBS, and imaged via AFM. We observed extensive occlusion of the surface of the modified crystal (Figure 3.6, right), but not of the unmodified crystal (Figure 3.6, left). The observed puncta inhabited the lower size range of SARS-CoV-2 virions (75.2 nm ± 5.8 nm, as opposed to the reported 60-140 nm in diameter). The near-complete absence of any surface occlusion of the unmodified crystal indicated that surface adsorption to the crystals is selective and dependent on modification via SpyCatcher-LCB1.

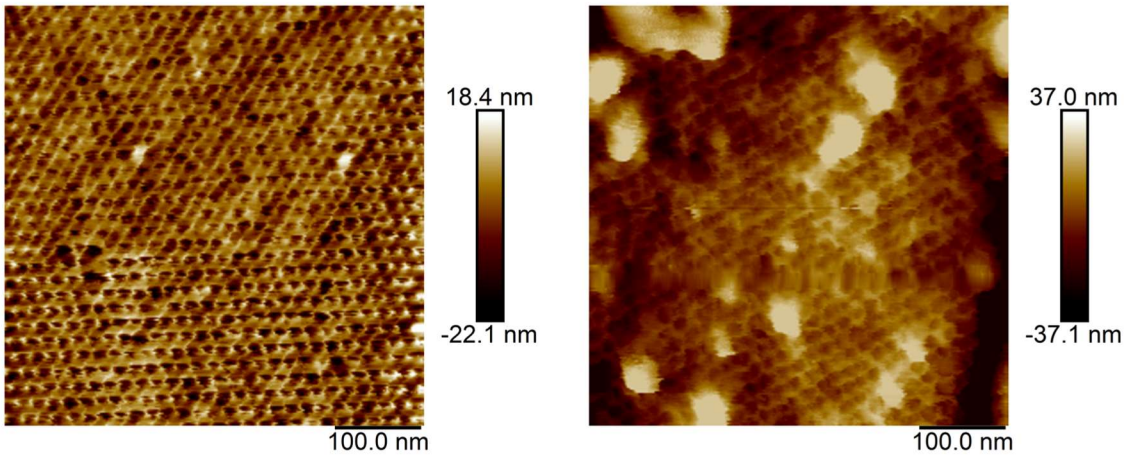

Figure 3.6: Atomic force microscopy reveals surface adsorption of SARS-CoV-2 virions to the surface of a modified SpyCrystal (right), while no adsorption was observed for an unmodified crystal in the same solution (left).

Following the results of this experiment, we performed additional experiments comparing the adsorptive capacity of modified and unmodified microcrystals. A batch of CJ SpyCrystals, 5 to 10 μm in diameter, was split into four aliquots, and soaked in one of four SpyCatcher fusion proteins (SpyCatcher-P8, SpyCatcher-SpikePlug, SpyCatcher-LCB1, or SpyCatcher-sfGFP).

After pelleting and washing the crystals, each aliquot of crystals was incubated for 4 hours with inactivated SARS-CoV-2 virus (~1.5 x 10^6 virions/μL). Afterwards, the concentration of virus was measured in both the supernatants and pellets associated with each sample via RT-ddPCR (Figure 3.7A). We observed a decrease in viral supernatant concentration exclusively in the spike-binding microcrystals (SpyCatcher-P8, -SpikePlug, and -LCB1), while the supernatant concentration in the SpyCatcher-sfGFP-soaked microcrystals remained high (> 1,000 copies μL^{-1}) (Figure 3.7B). Furthermore, quantification of viral copy numbers after isolating, washing, and lysing the crystal pellets themselves revealed the inverse correlation – the putative spike-binding crystals were associated with a higher viral copy number than the non-spike binding crystals. Poisson exact comparisons revealed a statistically significant difference between each of the supernatants for the spike-binding crystals, compared with the controls, but not between

individual spike-binder supernatants (95% CI). Similarly, the difference in copy number between the spike-binder crystal pellets and the associated controls was also significant.

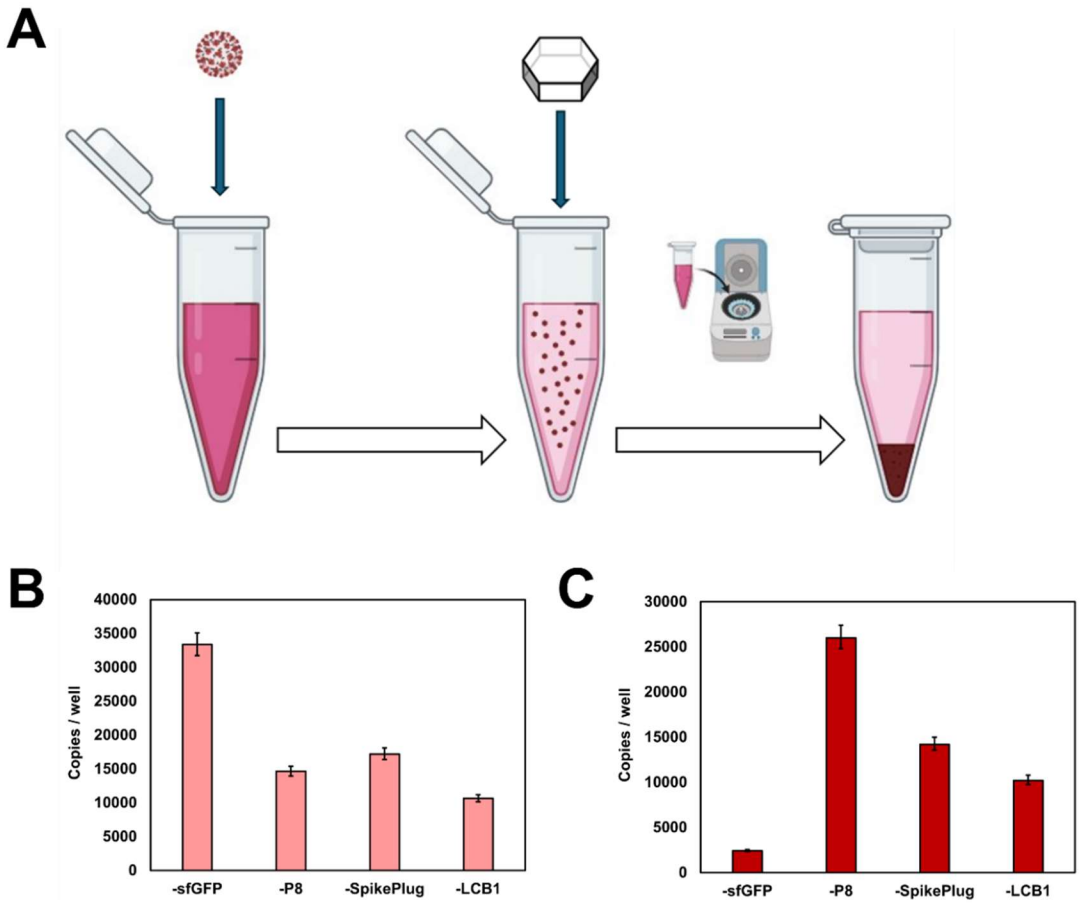

Figure 3.7: A, Experimental workflow for *in vitro* viral capture experiments. SARS-CoV-2 virus was combined with CJ SpyCrystals (either unmodified, or modified with one of three spike binders), incubated at room temperature, after which microcrystals were pelleted by centrifugation, separating captured and uncaptured virus. **B,** RT-ddPCR of the supernatants revealed depletion of SARS-CoV-2 virions from the surrounding solution for the functionalized SpyCrystals (P8, SpikePlug, and LCB1), but not for the unmodified crystals. **C,** RT-ddPCR of the microcrystals resuspended in lysis buffer revealed an enrichment of the virus bound to the crystals. Error bars represent the upper and lower bounds of the Poisson 68% confidence interval.

3.4.4 Hollow-fiber filtration and pumping enables continuous capture of viruses

We next sought to test whether or not the crystals could be integrated with an upstream pump and tangential flow filter, with the crystals immobilized within a packed FPLC column, to enable continuous capture of SARS-CoV-2 from wastewater. After soaking SpyCrystals with SpyCatcher-P8, -SpikePlug, or -LCB1 (or PBS as a control), the crystals were pelleted and resuspended to an equal concentration based on the weight of the pellet. The crystals were then packed into separate FPLC columns along with stripped NTA-agarose resin as an inert filler, then connected to a modified LifeStraw filter. This filter was in turn connected to an Arduino-controlled pump, which was used to pump clarified wastewater which had been supplemented with inactivated SARS-CoV-2 virions (4.8×10^2 copies μL^{-1}, final concentration). Fifty milliliters of spiked wastewater was pumped through each column three times, and the flow-through was collected each time. Viral copy numbers associated with each flowthrough were measured using RT-ddPCR (Figure 3.8B). We observed minimal depletion of SARS-CoV-2 virions from the wastewater in the unmodified crystals (227.5 copies μL^{-1}), while the flowthroughs for the -P8, -SpikePlug, and -LCB1 columns revealed, respectively, a 3.4-, 4.3-, and 6.6-fold reduction over the unmodified crystals from the same wastewater source. Furthermore, the observed trend was more consistent with the reported dissociation constants for

each of the spike binders, with LCB1 (K_d = 0.1 nM) displaying a higher capture rate than P8 or SpikePlug.

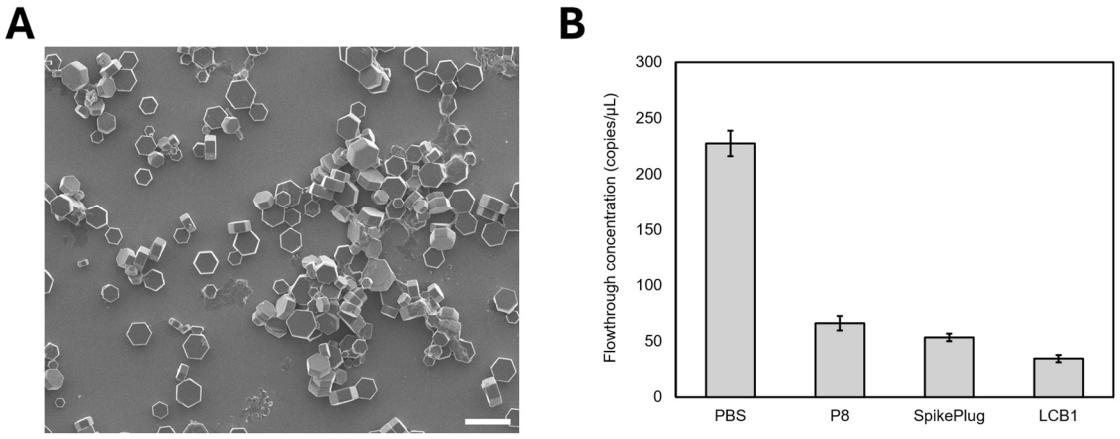

Figure 3.8: A, Representative scanning electron micrograph of CJ SpyCrystals used in the experiment. Scale bar = 20 µm. **B**, Flow-throughs from the integrated pump-Lifestraw system demonstrate a depletion of SARS-CoV-2 copies in functionalized SpyCrystals (P8, SpikePlug, LCB1), but not in the unmodified crystals (PBS) (n=3 replicates).

3.5 Conclusions

In the present chapter, we have successfully demonstrated that modified protein microcrystals can be used to selectively adsorb virions (and other 40-nm particles) from solution in vitro. Furthermore, integration of the crystals into a pumping system resulted in successful capture of SARS-CoV-2 virions from wastewater. While the crystals were outperformed by the traditional method of InnovaPrep concentration in terms of total virus captured, CJ crystals modified to bind SARS-CoV-2 spike protein consistently demonstrated a greater capture rate for SARS-CoV-2 virions over the unmodified crystals, suggesting that future CJ microcrystals could be engineered to display alternative paratopes, to selectively capture any arbitrary virus or antigen from a complex mixture.

While a number of strategies were initially explored for covalently installing a guest protein, including thiol-based chemistries, several challenges were encountered using these approaches, particularly exposure to harsh organic solvents; despite chemical cross-linking, mechanical

deformation of CJ crystals was routinely observed in dimethyl sulfoxide (DMSO) concentrations as low as 20% v/v. Therefore, we sought alternative strategies for guest installation that would enable both high modularity, and compatibility with most aqueous conditions. SpyCatcher/SpyTag interactions are functional over a wide solution pH range and ionic strengths.[54,72,155] Given that the C-terminus of the CJ protein is both pore-facing and does not otherwise participate in protein-protein interactions, we created a variant of CJ which includes a C-terminal, third-generation SpyTag. SpyTag003 was chosen over SpyCatcher003 as CJ crystals are normally cross-linked with amine-reactive dialdehydes, and SpyCatcher003 contains a lysine which participates in the formation of the isopeptide bond16. Furthermore, we hypothesized that SpyTag003, which is 16 amino acids long, is less likely to disrupt folding and interfere with CJ crystallization than SpyCatcher003, which has a molecular weight of ~15.2 kDa. The implementation of the SpyTag003/SpyCatcher003 system within the CJ crystal framework provided a modular and aqueous-compatible approach for covalently immobilizing protein guests while preserving the structural integrity and porosity of the host lattice. This strategy overcame the major shortcomings of earlier chemical conjugation attempts that relied on thiol-reactive linkers and organic solvents, which frequently induced partial dissolution or deformation of the crystals. By genetically incorporating SpyTag003 at the C-terminus of CJ, the reactive site was positioned within the 13–14 nm solvent channels, enabling precise, pore-localized capture of SpyCatcher-fused proteins. The robustness of the SpyTag/SpyCatcher isopeptide linkage allowed guest proteins to remain stably attached under the high ionic strength, variable pH, and mixed organic composition characteristic of wastewater samples. These properties establish CJ-SpyCrystals as a biocompatible and structurally resilient platform for modular functionalization with diverse molecular recognition elements.

Collectively, the results presented in this chapter demonstrate that porous protein crystals can be rationally engineered to achieve selective viral adsorption. Biotinylated CJ crystals served as a proof-of-concept, successfully capturing streptavidin-coated microspheres both in bulk and under flow (Figures 3.3 and 3.4). This confirmed that the chemically cross-linked lattice remained permeable and that reactive residues were accessible within the pore network. The subsequent introduction of the SpyTag003 motif enabled site-specific covalent immobilization of SpyCatcher-fusion guests, as validated by confocal imaging of SpyCatcher-sfGFP capture. Importantly, incorporation of the SpyTag did not disrupt CJ crystal formation or symmetry, highlighting the structural tolerance of the protein framework to modest C-terminal modifications. When fused to SARS-CoV-2 spike-binding domains, P8-, SpikePlug-, and LCB1-SpyCatcher003 facilitated the creation of "SpyCrystals" capable of adsorbing intact virions from solution and of enriching viral RNA following lysis. Integration of these functionalized microcrystals into a pump-driven hollow-fiber filtration setup further demonstrated their potential for continuous viral scavenging from complex matrices such as wastewater.

The selectivity observed for virion adsorption to the functionalized SpyCrystals, and not to unmodified CJ crystals, underscores the importance of molecular recognition rather than nonspecific electrostatic or hydrophobic interactions. Atomic force microscopy revealed punctate features on the surface of LCB1-functionalized crystals with diameters consistent with intact SARS-CoV-2 virions, while unmodified crystals displayed no comparable occlusion (Figure 3.6). These findings are consistent with a mechanism in which virions are captured via multivalent engagement of spike trimers with immobilized binder proteins at the pore entrances. The correlation between observed capture efficiency and the reported dissociation constants of the respective binders (LCB1 ≈ 0.1 nM > SpikePlug ≈ 40 nM > P8 ≈ 24 nM) suggests that the

immobilized binders preserve their tertiary structure and functional binding interface within the crystal microenvironment (Figure 3.8). Moreover, the maintenance of adsorption capability following multiple wash steps and mechanical agitation during pumping suggests that the SpyTag/SpyCatcher bond and the crystal lattice itself are sufficiently robust for repeated use or regeneration.

The hierarchical capture pattern observed across binder variants also provides preliminary insight into kinetic limitations imposed by molecular diffusion through the crystalline network. Because each CJ unit cell presents multiple accessible SpyTags within nanometer-scale channels, binding events are likely diffusion-limited rather than affinity-limited under the tested conditions.[72,156] Increasing the density of SpyTag incorporation, either by adjusting the co-crystallization ratio of CJ:CJ-SpyTag003 or through rational engineering of the scaffold protein, could therefore further enhance adsorption capacity.

Although traditional concentration techniques such as PEG precipitation and ultrafiltration may yield greater total viral recovery, these methods capture both viral and nonviral particulates indiscriminately and require extensive downstream purification steps.[157,158] In contrast, SpyCrystals exhibit specificity conferred by genetically encoded affinity binders, allowing enrichment of target virions directly from heterogeneous solutions. When applied to wastewater, functionalized crystals achieved up to a 6.6-fold reduction in viral RNA within the flow-through relative to unmodified controls. While absolute recovery was several orders of magnitude lower than InnovaPrep-based concentration, the selectivity and modularity of the SpyCrystal platform represent a distinct functional advantage. These attributes could be leveraged in alternative workflows—such as sequential filtration where SpyCrystals first remove target pathogens before broad physical concentration—to enhance throughput and diagnostic sensitivity.

However, several limitations became apparent. First, the mass-transfer rate within the crystalline matrix is likely lower[34] than in convective open-pore polymeric materials,[159,160] which may constrain capture kinetics during high-flow conditions. Second, crystal growth and cross-linking currently occur at small scale; scaling these processes to multi-gram quantities without compromising porosity or functional uniformity will require optimization of nucleation control and solvent equilibration.[161–163] Finally, while SpyCatcher-based immobilization proved highly effective for protein guests, alternative chemical conjugation schemes may be required for small-molecule ligands or nucleic acid probes that cannot be introduced as genetic fusions.[11,164–166] Addressing these factors will be essential for extending this proof-of-concept to broader applications.

A critical aspect of wastewater surveillance is the ability of the capture matrix to maintain performance in the presence of high concentrations of surfactants and organic and microbial debris. To remove larger particulate solids, we relied on the LifeStraw pre-filter. The experiments described here indicate that hollow fiber pre-filtration (0.05 μm reported pore size) was sufficient to preserve the performance of SpyCrystals without measurable loss of integrity or function over multiple flow cycles. The covalent nature of the SpyTag/SpyCatcher linkage prevented desorption of the guest proteins even after hours of exposure to wastewater. This contrasts with antibody-coated surfaces[167] or electrostatic membranes,[168] which can suffer from fouling and elution of bound molecules. The observed durability suggests that the system could support prolonged field deployment, particularly when integrated into self-contained filtration cartridges. Moreover, the straightforward regeneration of the crystals through washing and re-functionalization provides a path toward reusable biosorbents with consistent performance.

Additional work remains on quantifying adsorption isotherms and desorption kinetics,[159,168] as well as reusability over multiple operational cycles.[169] Additionally, expanding the set of functional binders to include other viral or bacterial targets will validate the generality of the platform.[170,171] From an engineering perspective, integration with microfluidic or cartridge-based systems could enable continuous monitoring of wastewater streams, with on-chip lysis and nucleic acid detection modules for near-real-time readout.[172–174] With respect to crystal robustness, exploring the long-term stability of cross-linked CJ crystals under varying temperature and microbial load will inform storage and deployment strategies.

In summary, this work establishes engineered CJ protein microcrystals as a versatile platform for selective adsorption of viral particles in complex fluids. Through genetic incorporation of SpyTag003 and covalent installation of SpyCatcher-fusion binders, the system represents a step toward molecularly specific, modular, and regenerable virus capture. The combination of structural precision, biochemical compatibility, and adaptability sets these materials apart from conventional polymeric or inorganic sorbents. While further optimization is required to enhance capacity and scalability, the demonstrated SARS-CoV-2 binding and robustness under wastewater conditions validate the feasibility of using protein crystalline frameworks as next-generation bioadsorbents.

CHAPTER 4: Ex Vivo Biocompatibility of CJ Microcrystals in Lung Tissue Slices

4.1 Overview

Non-systemic pharmaceutical delivery to upper and lower respiratory spaces is limited by the temperature sensitivity and molecular interactions of current carrier materials. To eliminate these challenges, it may be possible to use a variably solidified protein structure to protect biologically relevant molecules for delivery. Here, fluorescently labeled porous protein crystals were visualized along with fluorescently labeled guest domains and assessed for tissue modulatory abilities in the novel context of ex vivo lung tissue slices called precision cut lung slices (PCLS). When crystals were administered without an immunostimulant guest tissue health was consistent as demonstrated by a consistent percentage of permeable (apoptotic or mitotic) cells in each slice and no change in CD19+ B cells was observed. The engineered protein crystals had no obvious physical degradation throughout the experiments (5 days), and guest-loaded crystals were introduced to PCLS without evident cytotoxicity. PCLS in the presence of crystals loaded with fluorescently-labeled lipopolysaccharide (LPS) or LPS alone in media resulted in a much larger detectable B cell population than empty or DNA-loaded crystals compared to untreated tissue, suggesting a release of guest LPS from the porous crystals. Release of fluorescently labeled LPS from CJ crystals was similarly observed *in vitro* via confocal fluorescence microscopy. These results demonstrate the potential of porous protein microcrystals as a delivery vehicle for potential therapeutic compounds to generate a tunable immune response.

4.2 Introduction

Improved delivery mechanisms that target the lung are needed to improve therapeutic efficacy, but many existing platforms activate the immune system and require strict

temperature control.[175–178] This immune activation is often an unwanted byproduct which can worsen the condition which needs to be treated. Specifically, delivery to the lung is an existing challenge because of the pathways that administration can take, since current platforms are likely to have irregular dosage to the respiratory cavity, unless an invasive method is used.[175,176,179,180] This knowledge gap in therapeutic delivery is a contributing factor in why respiratory diseases have high mortality and have minimal treatment and prevention delivery options, leading to many respiratory conditions ranking as leading causes of death around the world.[181–183] This study takes the first steps to evaluate a more versatile delivery platform in the form of porous protein crystals as carrier particles for therapeutic delivery by determining the biological activity of porous protein crystals - in particular, their ability to carry biomedically relevant molecules.

There are several models in which introductory research into biocompatibility of crystals can be tested, ranging from cell lines to whole mice. The intent was to choose a model that maintained complexity of structure, function, and cell types, but did not have the challenges of a whole mouse. Here, a precision cut lung slice model was utilized to measure interactions of the crystals and their contents in tissue, which has the advantage of maintaining the three-dimensional structure of the lung, containing the same cell types, and consisting of different compartments, making it a much more viable model than a cell line or organoid system and without the complexity of accurately administering and visualizing in whole animals.[184–188] When administering directly to an animal, there are several barriers preventing quantification, especially in specific organs. For example, the number of crystals and time of release are difficult to control for, and effects in other parts of the body may result in confounding variables. For instance, the agonist may be

released in other parts of the mouse and non-specific effects may be observed. Generally, the goal behind working with a model system is to reduce complexity. However, it is useful to retain the maximum number of variables in a system, in order to ultimately ensure translatability from bench to bedside. These experiments may provide the basis for future utilization of these delivery molecules in live animals.[189,190] The three-dimensional structure present in an organotypic slice cannot be replicated in simpler models such as an organoid or cell line and allows for more normal lung activities to occur. These slices maintain ciliary beat, mucus secretion, immune responses, neural activity, and some compartmentalization which would not be present except for in live animals.[184–188,191] Because of the complex problem of accurately administering crystals in reliable quantities to specific organs in live animals, as well as the increased complexity of signalling in living systems, it was deemed prudent to test crystal viability in an *ex vivo* model prior to attempting *in vivo* studies.

Because this study is intended as a proof of concept for the biomedical usage of loadable crystals, it was important to select a well-studied molecule to demonstrate its known effects in a quantifiable form. Lipopolysaccharide (LPS) is one such molecule which meets this criterion. LPS is a large amphipathic molecule (> 100 kDa) which occurs naturally a glycolipid found in the outer membrane of gram-negative bacteria;[184,192] because of its abundance on the outer membrane,[193] it serves as a potent signal to the vertebrate immune system, in particular through co-activation of TLR4/MD2 complexes and CD14.[194] Because of its strong immunostimulatory properties, LPS has also been explored as a vaccine adjuvant.[195–197] Furthermore, because LPS is known to induce immediate B cell activation and proliferation, and because the B cell response can

be correlated with LPS dose,[198] it was deemed a suitable reporter guest molecule, for generating a metric of comparison in the tissue.[199–201]

It has been previously shown that CJ readily crystallizes into P622 crystals at high salt concentrations.[9,34] As described earlier in chapters 2 and 3, CJ crystals can be reliably grown with a diameter as large as 0.5 mm, to as small as 280 nm, by altering batch growth conditions (i.e., total protein concentration, precipitant concentration, and pH).[153] Whereas most protein crystals feature relatively small solvent channels.[202] CJ crystals possess unusually large solvent nanopores with a diameter of ~13 nm. As a result, CJ crystals can be loaded with diverse guest molecules, enabling diverse potential biological applications. It was also previously observed that CJ crystals adsorb nucleic acid guests with strong binding affinity,[44] and can also be loaded with enzymes,[34] fluorescent proteins,[9] and small molecules.[11] However, the applicability of porous CJ nanocrystals for guest delivery and other biomedical applications in the context of living biological tissue has not previously been tested, particularly with respect to any off-target immune responses to the crystals themselves.

CJ crystals possess unique properties which may make them an ideal therapeutic guest carrier. Specifically, their porosity lends them remarkably high guest capacity, and the precisely known periodic structure of the nanopore array can enable structure-guided approaches to tune or trigger guest release. While CJ crystals are known to retain guest nucleic acids following solution transfer and washing, they have not previously been tested for their ability to hold other therapeutically relevant molecules such as glycolipids. The aim of this chapter is to evaluate the crystals' ability to retain and release a biologically potent small-molecule guest, by observing local responses within

organotypic slices, as well as to identify off-target immunomodulatory responses to the crystals themselves.

4.3 Methods

4.3.1 Animals

Young male and female adult C57BL/6J mice were used for all experiments. Mice were housed by Laboratory Animal Resources in the Pathology Building at Colorado State University. Mice were multi-housed in plastic cages with aspen bedding (autoclaved Sani-chips; Harlan Teklad, Madison, WI) with a 12:12-hour light-dark cycle and access to water and food (no. 8640; Harlan Teklad). Animals were cared for and utilized according to the Colorado State University institutional animal care and use committee protocol #1413.

4.3.2 Precision Cut Lung Slice (PCLS) preparation

Slices were prepared similarly to previous work[187,203]. Adult C57BL6/J Thy1-YFP mice were anesthetized using isoflurane and decapitated. Animals were perfused through the heart with warm phosphate buffered saline (PBS). The lungs were inflated using 1ml of 40°C 2% low melting point agarose in MQH2O until the lung was visibly inflated to the edge of the lung without rupturing it. A lung lobe was sliced at 250µm using a vibrating microtome (VT1000S; Leica Microsystems, Wetzlar, Germany). Slices were cultured in phenol red-free lab-made adult neurobasal culture media made with 4mM glucose and L-cysteine reduced to 175µm[204] with 2% B27 supplement (Life Technologies; 17504044; CTS+B27 cell culture media) with a collagen overlay composed of vol/vol: 10.4% 10× MEM, 1.9% PS, 4.2% sodium bicarbonate, and 83.5% collagen (PureCol; Inamed, Fremond, CA). Slices were cultured for up to five days with

daily media changes. To account for biological variability between mice of the same sex, slices from three animals were used to generate experimental values for male and female mice.

4.3.3 Tissue health

Tissue health was assessed by visual inspection of morphology in each experiment. Slices were phase bright and did not contain dark patches indicative of necrosis; they also did not show any signs of tissue degradation such as fraying edges or visible loss of epithelial or endothelial cells. These morphological consistencies indicate that cells are healthy, undergo some metabolic processes, and are maintaining 3D structural integrity. To quantify any toxicity leading to cell death, acridine orange (AO) was used to visualize nuclear membrane permeable cells (in which AO bound DNA and emitted red fluorescence) and all cells (where AO bound cytosolic RNA and fluoresced green)[205]. Slices were incubated at 37°C with 2μM AO (A1301; Invitrogen, Thermo Fisher Scientific) followed by 3x10-minute washes with lab-made adult neurobasal + B27 media. Slices were then imaged live using a Nikon Te2000 for acridine orange binding to DNA using a Texas red filter set (fluorescent emission 656) and for binding to RNA using a fluorescein/GFP filter set (emission 533). Acridine orange is a biochemical assay which allows for quantitative analysis of cell death by image analysis of the number of cells with the number of nuclear permeable cells with DNA binding compared to the number of cells with bound RNA. A baseline of red cells indicates a normal level of either cell death or mitosis, which provide dye access to exposed DNA.

4.3.4 Expression, purification, crystallization, and cross-linking of CJ

CJ protein was expressed and purified as described previously[9,34]. Large (>50 μm diameter) CJ crystals were grown via sitting-drop vapor diffusion. Briefly, 2.5 μl drops, containing approximately 30 μg of purified CJ protein in a storage buffer (50 mM HEPES, pH 7.4, 0.5 M ammonium sulfate, 10% glycerol), were mixed with 2.5 μL of sitting-drop well buffer, before sealing the well and incubating at 4°C for several days. Each well contained approximately 400 μL of buffer; precipitant concentrations ranged from 3.1 M to 3.6 M ammonium sulfate, 100 mM Bis-Tris, at pH 6.0 or 6.5. Following growth, large crystals were individually looped from the mother liquor and washed multiple times in 4.2 M trimethylamine-N-oxide (TMAO). Crystals were transferred to a cross-linking solution composed of 40 mg mL^{-1} 1-ethyl-3-(3-dimethylaminopropyl) carbodiimide hydrochloride (EDAC), dissolved in 4.2 M TMAO, for at least 24 hours, and up to 7 days, at room temperature. After cross-linking, the crystals were looped into a quench solution (50 mM sodium borate, pH 9.0) and incubated at room temperature for 30 minutes to 1 hour, before storing long-term in 20 mM HEPES, pH 7.4 at room temperature. Microcrystal batches were synthesized using a minimally modified cross-linking as compared to previously described[44,153]; in short, one volume of purified CJ protein, concentrated to between 40 and 50 mg mL^{-1}, was combined with 5 volumes of precipitant buffer (3.2 M – 3.5 M ammonium sulfate, 100 mM HEPES or Bis-Tris, pH 7.0). The total volume of crystals grown using this method ranged from 240 μL (i.e., 40 μL of protein combined with 200 μL of precipitant buffer) to 720 μL. Cross-linking of microcrystals was achieved by first pelleting the crystals via centrifugation (5 minutes at 2,000 x g) and replacing the mother liquor/supernatant with 4.2 M TMAO. After

centrifuging again, the supernatant was replaced with 0.5 - 0.75 mL cross-linking buffer (40 mg mL^{-1} EDAC, dissolved in 4.2 M TMAO) (Figure 4.1D), supplemented with NHS-Pacific Blue dye (Thermo Fisher, P10163) or NHS-Texas Red dye (Thermo Fisher, T20175) at a final concentration of 5 μg mL^{-1}. The crystals soaked in cross-linking buffer for > 18 hours at room temperature, with constant inversions. Microcrystal cross-linking was quenched by pelleting the crystals and replacing the supernatant with EDAC quench buffer (50 mM sodium borate, pH 9), then incubating at room temperature with constant inversions for >30 minutes. The crystals were then pelleted a final time, and the supernatant was replaced with 1X PBS, pH 7.5. Microcrystals were stored for up to 1 year at room temperature. All crystals were sterilized via UV irradiation in a CL-1000 ultraviolet cross-linking oven (Artisan Technology Group), at 100 μJ cm-2 for 5 minutes, prior to *ex vivo* live tissue exposure. Crystal surfaces were visualized using atomic force microscopy, as described previously.[30]

4.3.5 Guest DNA and lipopolysaccharide (LPS) loading

For loading of guest nucleic acids, crystals were soaked for greater than 1 hour at room temperature in 1 μM, 5' fluorescein-labeled ssDNA (5'-TAGGCGACTCGACGGTCTTACGCGTTACGT -3'), and subsequently washed in nuclease-free water. Guest fluorescence within the crystals was validated on an Eclipse Ti-E series inverted spinning disk confocal microscope (Nikon), prior to crystal addition to tissue slices. For LPS testing, crystals were incubated at room temperature with 0.1 mg mL^{-1} Alexa Fluor 568-LPS conjugate for > 1 hour. After soaking, the crystals were washed once and resuspended in nuclease-free water.

4.3.6 Crystal addition to lung tissue slices

Using a sterile biosafety cabinet, 8 µl of CJ microcrystals (~$8x10^7$ microcrystals) were added atop each of two lung slices in dishes containing 800 µl adult neurobasal + B27 media except for in one set of control experiments in which large single crystals (200-800 µm diameter) were used instead of the microcrystals (~200-400nm) crystals which were used in all other experiments. In these control experiments, large crystals were added selectively to the bronchiole, superior to the tissue over the collagen overlay; where the microcrystal suspensions were delivered via pipette, large crystals were individually placed using a microscopic loop (Hampton Research) to assess crystal position as a factor in effect. One feature of crystalline delivery materials is scale invariance. The nanostructure of a crystal with diameter 1 micron is identical to the nanostructure of a crystal with a diameter of 1 mm. Dishes with crystals and lung slices were maintained in a standard tissue culture incubator (100% humidified, 37 degrees, 5% CO2) for 24, 48, 72, and 96 hours. Changes in crystal location, interaction, and guest were then assessed by fluorescence microscopy using a Nikon TE2000-U inverted microscope spinning disk confocal microscope, or a Zeiss LSM 880 confocal microscope with an Axiocam 503 mono camera (Carl Zeiss, Inc., Thornton, NY).

4.3.7 Visualizing crystal movement through collagen

To assess crystal penetration of a collagen gel, microcrystals were introduced on top of 40 µl of polymerized collagen in dishes containing 800 µl of culture media. Crystal movement through the collagen was then observed via time resolved images at 0-, 5-, 10-, 45-, and 120-minutes (data not shown). Subsequently, crystals were applied to dishes

containing lung slices with collagen gel overlay and imaged live over 120 minutes at 5-time points; at 0 h, 24 h and 96 h using a Nikon Te2000-U inverted microscope.

4.3.8 Quantifying LPS retention in and diffusion from CJ microcrystals

Lung slices from male and female mice were exposed in parallel to culture media containing 10 µl ml^{-1} microcrystals (~280 nm in diameter) soaked in LPS (L23352 Thermo Fisher Scientific), crystals without LPS, or LPS for 48-hours. Slices were then processed immunohistochemically to visualize the number of CD19+ immunoreactive B cells to determine if an immunomodulatory change may have been made by released LPS. The diffusion of fluorescently labelled LPS guest was measured *in vitro* in crystals by monitoring the surrounding fluorescence of individual crystals loaded with LPS. Following cross-linking, large CJ crystals between (between 185 and 220 µm in diameter) were soaked overnight in 50 µg mL^{-1} Alexa Fluor 568-LPS conjugate (in 1X PBS, pH 7.5). Following soaking, the crystals were individually transferred to a 35 mm culture dish, in 50 µL of the LPS solution. After an initial round of imaging, 450 µL of fresh 1X PBS was added to the drop. Immediately following dilution of the crystals, fluorescence was monitored over a circular region of interest (ROI) within each crystal over a ~15-minute period. The crystals were then soaked overnight (about 13.5 hours) in 1 mL 1X PBS in the dark, before imaging for a final time.

To estimate the rate of diffusion of guest LPS from CJ microcrystals, 20 µL of LPS-saturated microcrystals (~10^{10} microcrystals mL^{-1}, as measured by tunable resistive pulse sensing (TRPS)) were added to three separate wells in a modified 96-well plate. Briefly, the inner rings from 0.2 mL PCR tube caps were carefully sliced off, and directly glued to bottom of the well, near one of the edges. After drying and curing, LPS-saturated crystals

were pipetted into the crescent-shaped gap (Figure 4.5D), before slowly pipetting 180 µL of 1X PBS, pH 7.5 to the center of the well. This ensured that the crystals remained out of the light path of the instrument during data collection. Fluorescence (λ_{ex} = 568 nm, λ_{em} = 603 nm) was measured every 5 minutes, over a 12-hour period, independently for each well; area scans of the wells were performed before dilution, after dilution, and after data collection, to ensure that the area within the plastic ring remained clear of crystals. The difference in LPS concentration was also measured after soaking in crystals to quantify the total amount of LPS loaded. The resulting fluorescence values were then converted to concentration (in µg mL^{-1}) using a standard curve ranging from 0 to 50 ug mL^{-1} (200 µL volumes per well). The concentrations were averaged across all three replicates at each time point, and the standard error of the mean was calculated for each time point.

4.3.9 Immunohistochemical analysis

In preparation for immunohistochemical analysis, PCLS were fixed via 15-minute exposure to 4% paraformaldehyde. After fixation, the lung slices were placed in 1% sodium borohydride for 2-hours followed by 3X 10-minute PBS washes. The tissue was blocked using a 5% normal goat serum (NGS; Lampire Biological, Pipersville, PA), 3% hydrogen peroxide, and 0.3% Tx solution in PBS for 2-hours with a change of solution at 1-hour. Primary antisera, CD19 (14-0199-82 eBiosciences, RRID: AB_467151) was applied in a solution containing 5% NGS, 0.3%Tx, and PBS for 120-hours. Before application of fluorophore-conjugated secondary antisera, Cy3 anti-rat (111-166-045 Jackson Immunoresearch, RRID: AB_2338253), slices underwent 4x30-minute washes in a 1% NGS, 0.2% Tx, and PBS solution. Slices were exposed to secondary antisera for 24-hours followed by 4x30-minute washes in a 0.02% Tx PBS solution.

4.3.10 Image and statistical analyses:

Analyses were performed for number of cells labeled in the red or green channels labeled with acridine orange or labeled immunohistochemically as CD19+ using NIH Fiji (v.2.9.4) in sets of 5 live (AO treated) or 12 post-fixation (CD19+) images (with a 2048-2048-pixel ROI) to account for variability. A one-way ANOVA analysis was performed for number of B cells in untreated, empty crystal, LPS loaded crystal, and LPS treated slices as well as for average number of cells labeled by acridine orange in the green and the red channels of crystal and vehicle treated slices. Post-hoc testing via a Fisher's LSD was performed and data are presented as mean +/- standard deviation. A $p < 0.05$ was considered significant. Data analyses were performed using R. The investigator conducting all quantitative analyses was blinded to the treatment groups. A Kruskal-Wallis test was performed in R to validate the results of the one-way ANOVA. After the Kruskal-Wallis test, a Mann-Whitney U test with a Bonferroni correction was performed to determine which comparisons were significant.

4.4 Results

Unless otherwise noted, the experiments described in this chapter used EDAC-cross-linked crystals. The crystal diameters ranged from ~200-400 nm for quantification of LPS release over time (Figure 4.5D,E), to 2-10 µm for studying crystal-tissue interactions (Figures 4.3, 4.4, 4.6, and 4.7), to 150 to 200 µm for direct monitoring of LPS diffusion from large crystals (Figure 4.5A-C).

Lung slices were maintained *ex vivo* for up to 5 days and brightfield images of lung slices at low and medium magnification are provided here as a reference for readers without a respiratory focus and as a corroboration of some health characteristics. The

health status of lung slices was observed using a variety of characteristics: maintenance of morphological characteristics, ratio of cell permeability (Figure 4.6), and absence of necrosis. If present, necrosis would appear as phase dark regions in the tissue. Macroscopically, lung slices consisted of the alveolar spaces (where breathing would occur *in vivo*), the parietal pleura which is the outside wall of the lung (Figure 4.1A), the airways or bronchioles, and the blood vessels or arterioles (Figure 4.1B). In all cases, the tissue slices maintained their characteristic shapes and sizes without evidence of degeneration regardless of treatment.

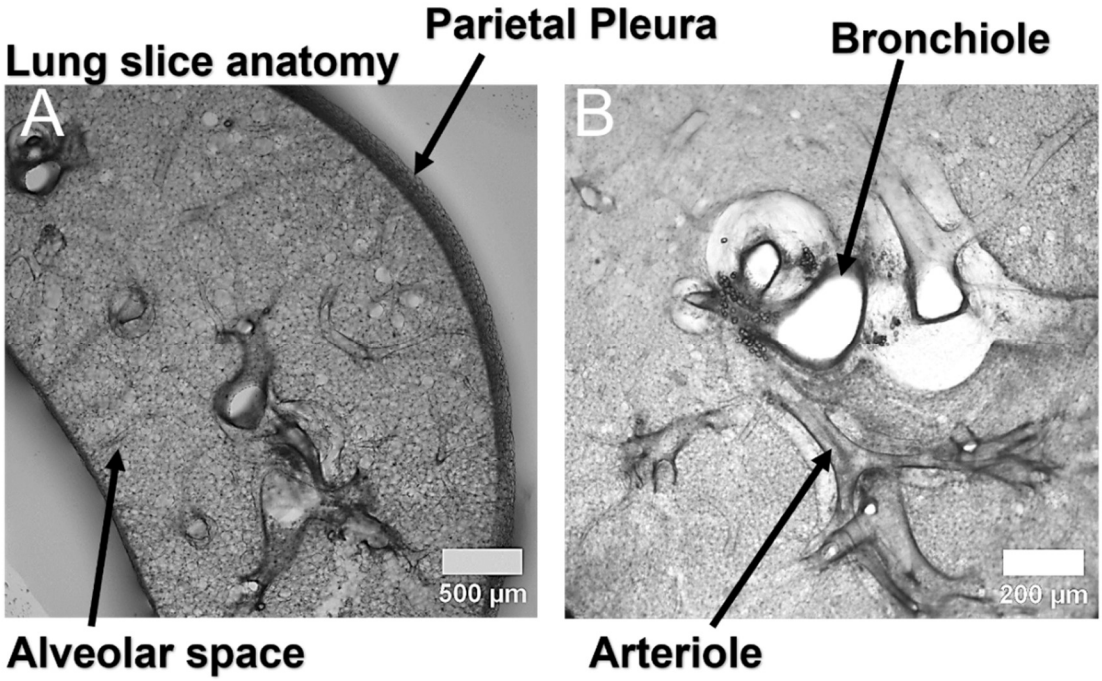

Figure 4.1: Anatomy of a precision-cut lung slice (PCLS). **A,** Alveolar space and parietal pleura with 500µm scale bar. **B.** Arteriole and bronchiole with 200µm scale bar.

4.4.1 CJ microcrystals are capable of penetrating collagen overlay

As a verification of the model, it was necessary to determine whether the crystals could enter the plane of the tissue and maintain contact with the tissue over time. To determine whether the crystals could enter the tissue slices, 8 µL of a suspension of Texas Red-

labelled microcrystals (diameter ~15 μm) were applied with a pipette after resuspension on top of the collagen overlay, and the progression of crystals into the plane of the tissue was observed by sequential imaging. Live images were taken immediately, 24 h, and 96 h after crystal addition. Crystals were visible in the Texas Red channel (Figure 4.2E-H), but not the fluorescein/GFP channel (Figure 4.2A-D), allowing for differentiation of crystals from background autofluorescence. Some crystals sedimented into the plane of the tissue immediately after addition (Figure 4.2A,E). Additional crystals settled into the imaging plane over the next several days (Figure 4.2C,G). Each image contains an airway which can vary greatly in size around which crystals are visualized. After aldehyde fixation, high magnification images of the crystals in the tissue showed no degradation of Texas Red fluorescence or crystal shape (Figure 4.2D-H). In order to control for location effect and obtain a more precise dose estimate, larger crystals (which possessed the same characteristic 13 nm pore structure) were precisely placed by hand using a nylon loop onto tissue slices. No significant difference in measured CD19+ B cell response was

observed compared to addition of numerous smaller crystals.

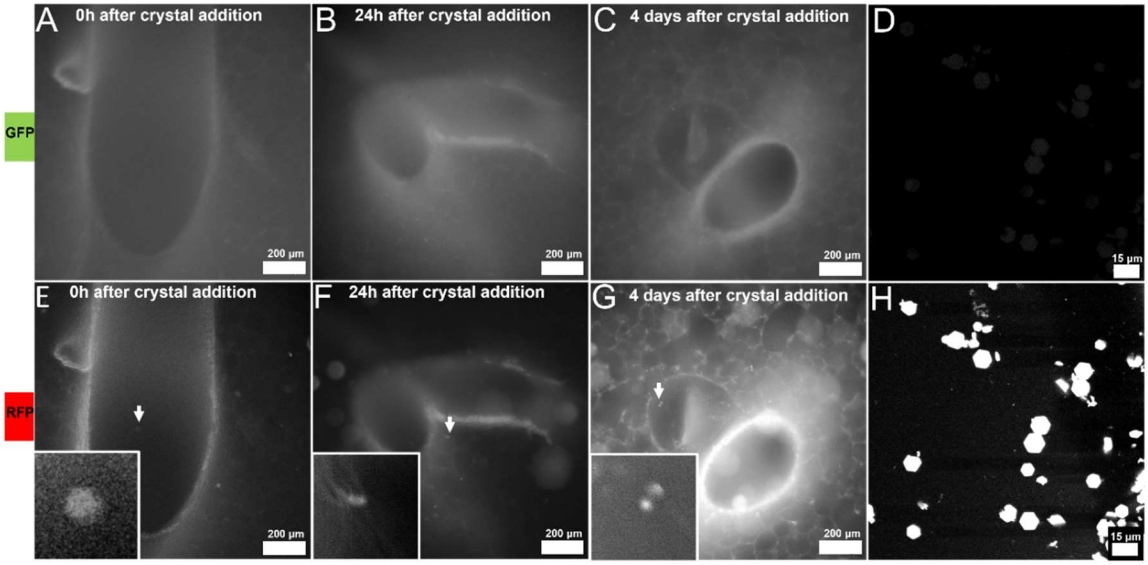

Figure 4.2: Lung slices exposed to unloaded Texas Red-labeled micro/nanocrystals. **A-C,** PCLS imaged live immediately, 24 h, and 96 h after crystal addition show no fluorescence in the green channel and are a control for crystal visualization. Scale bar is 200µm. **E-G,** PCLS imaged live immediately, 24 h, and 96 h after crystal addition are fluorescent in the red channel and demonstrate a greater number of crystals present in the plane of the tissue over time. **D,H,** After fixation confocal images of crystals were acquired showing no fluorescence in the green channel and high fluorescence in the red channel. No degradation of crystal fluorescence or structure was observed compared to pre-experiment crystals. White arrows indicate where inserts were taken. Scale bars are 200 µm for A-C and E-G. Scale bars are 15 µm for D and E.

To show crystal presence in tissue slices, a low magnification image containing Texas Red labeled crystals (Figure 4.3A) was provided alongside a control image (Figure 4.3B) to show variance in size and location. Because images are single plane, many of the crystals are out of phase and therefore difficult to see clearly. Lung slices are 250 µm thick so in this image which is focused in the mid to bottom region of the slice, even out of focus points of light are not visible for all crystals present. With these crystals it was also observable via confocal microscopy after 48 hours that some crystals appear to be within cells resulting in a decrease in fluorescent intensity of the crystals. This decrease in light does not correlate with a deterioration of the crystal, and the fluorophores are covalently attached to the crystal and are not likely to be dimmable, possibly indicating an occlusion of the fluorescent intensity. Furthermore, other experiments demonstrated that

no change in fluorescent intensity was observed in labeled crystals recovered from being cultured with slices for 4 days. However, it was not possible to quantify or confirm this uptake by methods other than microscopy, so no definitive conclusion could be reached. Microcrystals were loaded with a fluorescein-conjugated, 30-nt ssDNA to demonstrate that crystals can be tagged with a fluorophore and loaded with a fluorophore conjugated molecule relevant to biomedical processes. Additionally, crystals were visualized in red and green channels in single plane images for unloaded and loaded crystals allowing for visual confirmation that fluorescently conjugated guest molecules are discernible in the tissue and that loss of guest molecules may be visualizable. In the overlayed images, Texas Red labeled crystals also loaded with fluorescein conjugated DNA appeared yellow in lung tissue.

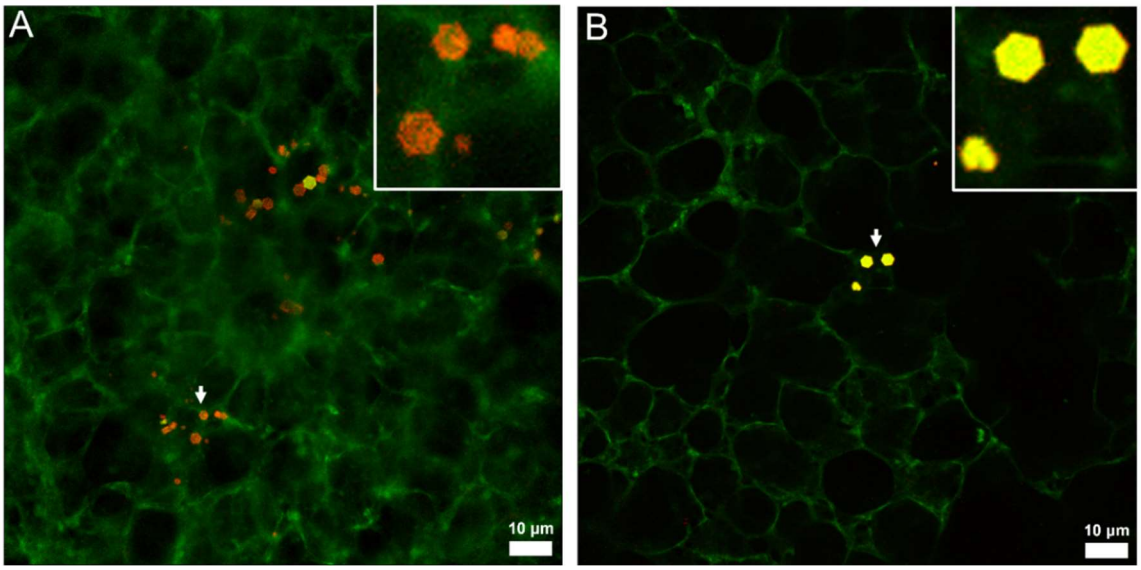

Figure 4.3: Crystals can be loaded with biologically relevant fluorescently conjugated molecules. **A,** Unloaded crystals are labeled with a Texas Red Fluorophore and visualized in a 3D projection. **B,** Loaded crystals are labeled with a Texas Red fluorophore and loaded with a fluorescein-conjugated DNA. White arrows indicate where inserts were taken. Scale bars are 10 µm.

4.4.2 CJ crystals can adsorb and release lipopolysaccharide (LPS) over several hours

The diffusion of guest fluorescent LPS from CJ crystals was further characterized *in vitro* by monitoring fluorescence in multiple LPS-saturated CJ crystals via spinning disk

confocal fluorescence microscopy. It was also initially hypothesized that, due to its high amphipathicity, LPS might potentially bind to CJ crystals with a similar affinity as DNA or RNA, although this was ultimately not observed; rather, guest LPS appears to diffuse steadily from LPS-saturated CJ crystals over a period of several hours in PBS (Figure 4.4B,C); this same diffusion was observed for CJ microcrystals (Figure 4.4D,E). As shown in (Figure 4.4B), normalized fluorescence within 3 crystals begins to decrease very gradually over a 15-minute period. While we observed some increase in normalized fluorescence in crystal 1 between 200 and 500 s, we believe that this is likely due to guest LPS diffusing into the focal plane from the crystal interior and is a consequence of LPS diffusing out of the crystal. Supporting this, following an overnight soak in 0.5 mL PBS, a dramatic decrease in fluorescence was observed in all three crystals (Figure 4.4C). Despite the net decrease in fluorescence, the crystals still retained greater fluorescence following the overnight soak, when compared to the crystal fluorescence prior to loading, suggesting that a detectable amount of LPS still remained within the crystals. In addition to observing diffusion from large CJ crystals (> 0.1 mm diameter), we also observed diffusion of guest LPS from saturated CJ microcrystals (< 1 μm) using a modified 96-well plate (Figure 4.4D). After soaking 100 μL of CJ microcrystals (~109 microcrystals, 280 nm in diameter) in ~46 μg of fluorescently labeled LPS for > 24 h, the crystals were pelleted, and the supernatant removed and measured. From these measurements, we estimated loading to be ~38 μg per 109 microcrystals. After diluting the crystals 1:10 in fresh PBS, the wells were monitored over a 12-hour period; we observed a sharp increase in solution LPS over the first ~2 hours, following dilution (Figure 4.4E). Each well

contained approximately $2x10^8$ microcrystals, and each crystal was approximately 280 nm in diameter.

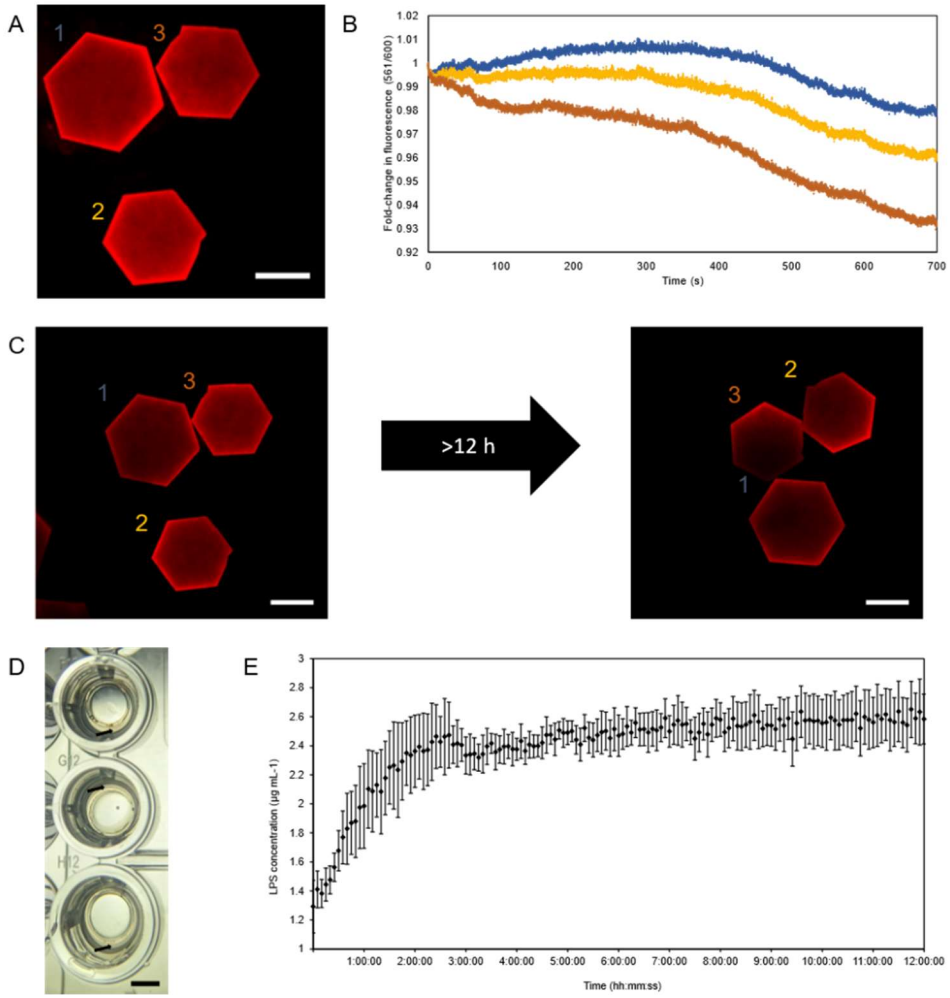

Figure 4.4: A, Three large CJ crystals, which have been soaked overnight in fluorescently labeled LPS. Individual crystals are indicated with a number at the top left. Scale bar = 100 µm. **B,** Relative fluorescence within each region of interest, measured over 700 s, normalized to relative fluorescence at t = 0 s. Colors correspond to individually-labeled crystals in panels A and C. **C,** Global decrease in crystal fluorescence, following a >12-hour soak in the dark in phosphate-buffered saline (without LPS). Scale bar = 100 µm. **D,** For measuring LPS diffusion from microcrystals, crystals were sequestered to the outer perimeter of the wells (black arrows), in order to keep the crystals out of the light path, while still allowing LPS to diffuse throughout the buffer in the well. Scale bar = 3 mm. **E,** LPS concentration in solution, following 10-fold dilution of LPS-loaded crystals in 1X PBS (200 µL final volume), as measured by plate reader. Diffusion was monitored across three replicate wells over 12 hours. Error bars indicate the standard error of the mean.

4.4.3 CJ crystals display no cytotoxic or immunogenic effects on their own

To demonstrate the health of the tissue, live slices exposed to unloaded NHS-pacific blue conjugated crystals (~2-10 µm diameter) were treated with acridine orange (Figure 4.5).

Acridine orange has fluorescent visibility in both the red and the green channels and thus it was necessary to use crystals conjugated to a non-Texas red fluorophore. DNA in cells with permeable membranes was visualized in the red channel (Figure 4.5B,E) and cytoplasmic RNA in the green channel (Figure 4.5A,D). Because acridine orange can cross cellular but not nuclear membranes, the red channel visualizes the consequences of porous nuclear membranes of dead or mitotic cells. No changes in the average number of permeable cells (LPS treated = 34 n=9, control = 43, n=9; p=0.624) or RNA positive cells (LPS treated = 291, n=9, control = 272, n=10; p=0.321) per ROI were observed with crystal addition. Red and green overlays (Figure 4.5C,F) were generated to show localization of the labeled DNA and RNA populations. CJ crystals were distinguished from the background via DAPI illumination (Figure 4.5G). The average percentage of total cells with permeable membranes was between 10-15% for both vehicle and crystal treated slices (Figure 4.5H). Cross-linked CJ crystals were previously found to have no observable toxicity when incubated with HDFa cells[44], but had yet to be tested in tissue.

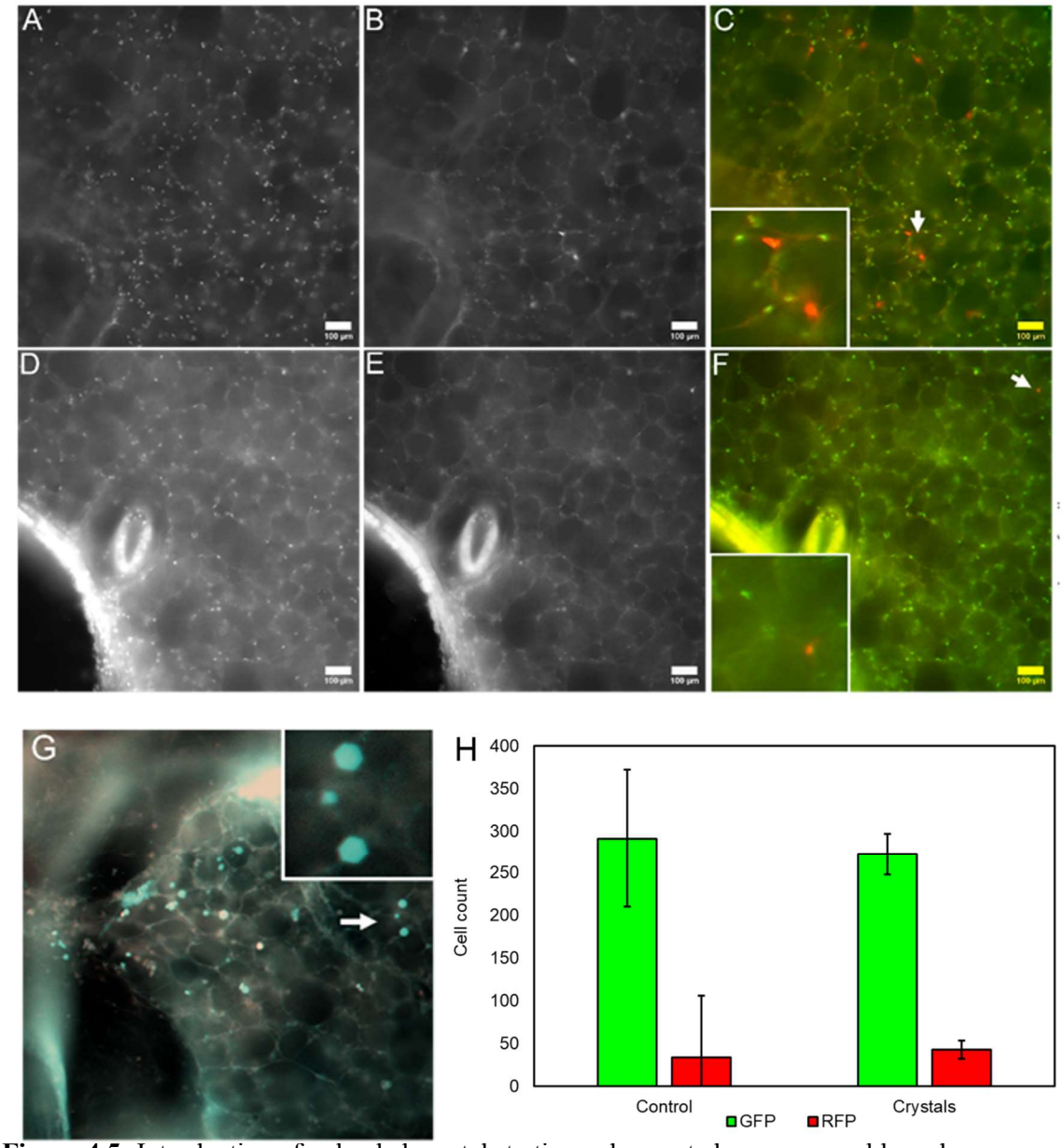

Figure 4.5: Introduction of unloaded crystals to tissue does not change permeable and non-permeable cell ratios. **A-C,** Precision cut lung slice containing unloaded crystals. **A,** RNA positive cells. **B,** Cells with permeable nuclear membranes. **C,** Composite image of **A** and **B. D-F,** Precision cut lung slice containing no crystals. **D,** RNA positive cells. **E,** Cells with permeable membranes. **F,** Composite image of **E** and **F**. **G,** Crystals labeled with NHS-pacific blue to prevent fluorescent overlap with acridine orange. **H,** Graphical representation of average RNA positive cells and cells with permeable cell membranes in ROIs from untreated slices (control) and slices exposed to unloaded crystals. Permeable cells (LPS treated = 34 n = 9, control = 43, n = 9; $p > 0.05$) or RNA positive cells (LPS treated = 291, n = 9, control = 272, n = 10; $p > 0.05$). **** indicate $p < 0.0001$. White arrows indicate where inserts were taken. Scale bars are 100 μm.

The addition of unloaded crystals did not significantly alter B cell populations in lung slices compared to tissue without crystals (56.9 ± 5.2 vs. 54.2 ± 15.7; $p > 0.1$) (Figures 4.6, 4.7). In contrast, slices treated with LPS-loaded crystals (77.2 ± 10.4, n=6) or an LPS

bolus applied in solution (111.9 ± 14.0, n=8) exhibited higher B cell populations than slices treated with unloaded crystals, with significant increases observed for both comparisons ($p < 0.05$ and $p < 0.01$, respectively). Furthermore, LPS in solution induced significantly greater B cell expansion than LPS delivered via loaded crystals ($p < 0.05$). Vehicle controls were not significantly different from any other condition. These results were confirmed by Kruskal–Wallis testing across all groups ($p = 1.8 \times 10^{-4}$), with post hoc Mann–Whitney U tests identifying the specific pairwise differences noted above. Finally, slices from female mice exhibited a greater increase in B cell numbers in

response to both LPS treatments compared to slices from male mice (data not shown).

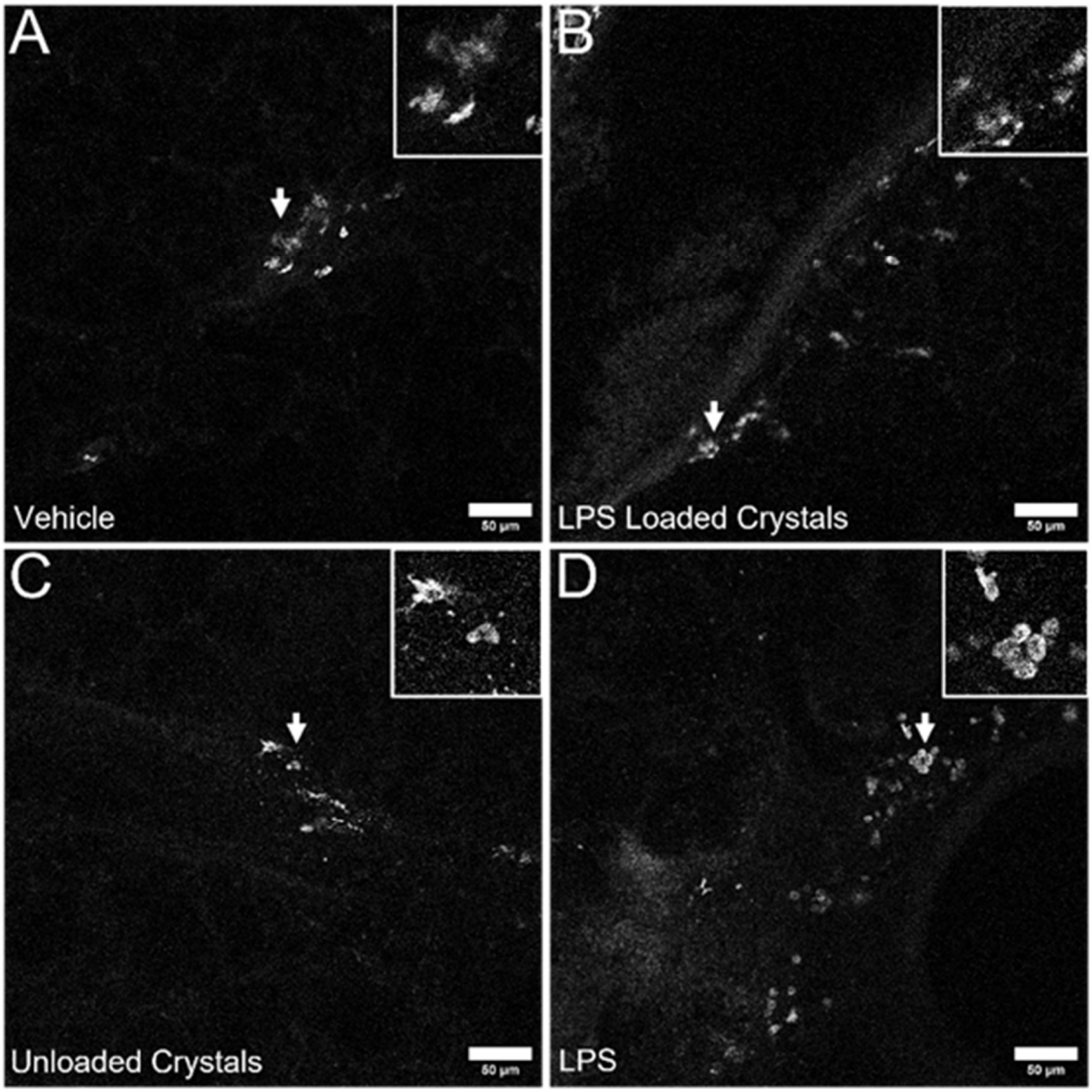

Figure 4.6: Loading LPS into crystal pores changes the CD19+ B cell immunomodulatory effects of crystals. **A,** B cell population 48h *ex vivo* in PCLS not exposed to crystals (n=5). **B,** B cell population 48h ex vivo in PCLS exposed to LPS loaded crystals (n=6). **C,** B cell population 48h ex vivo in PCLS exposed to unloaded crystals (n=7). **D,** B cell population 48h *ex vivo* in PCLS exposed to LPS with no crystals in culture solution (n=8).

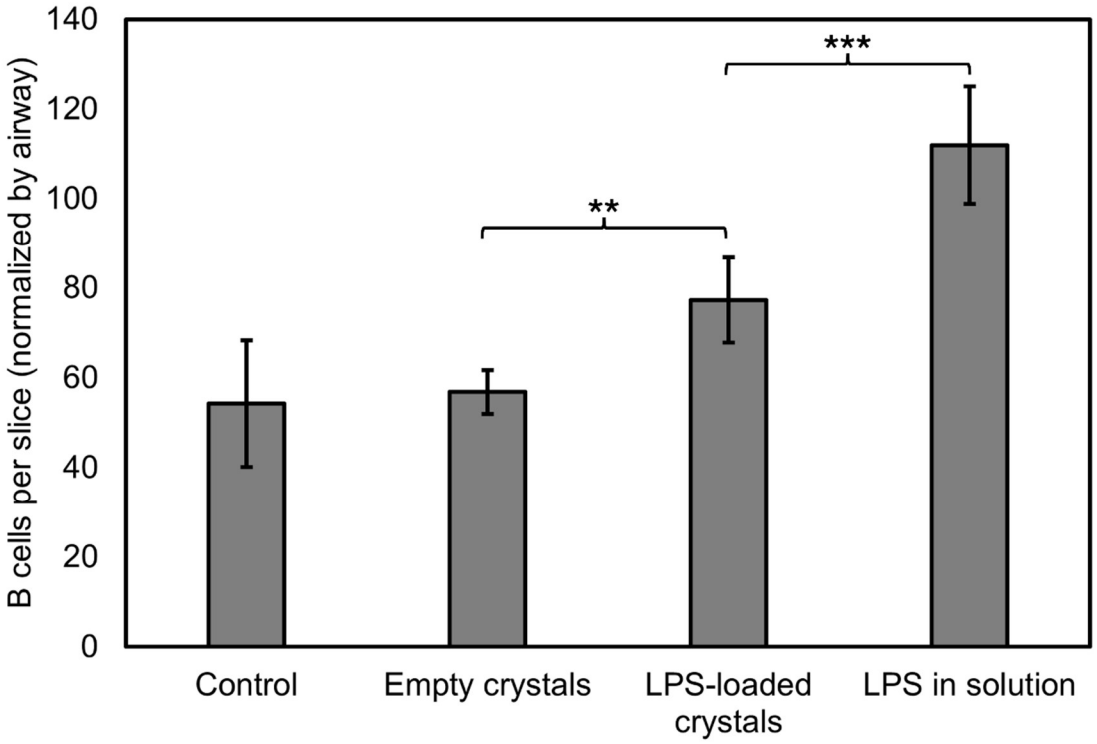

Figure 4.7: B cell counts per tissue slice, normalized by airway size. LPS administered in solution resulted in a higher B cell response when compared with an equivalent amount of LPS administered via crystals, suggesting that guest molecule release from the crystals is more gradual. ** = $p < 0.05$, *** = $p < 0.01$, as determined by Mann-Whitney U test.

4.5 Conclusions

As a vessel for biomolecules, crystals like the CJ crystals have several potential advantages that are not present in currently existing platforms. Being a rigid hollow structure, their loading capacity is much larger than that of spherical inorganic particles, such as gold nanoparticles; furthermore, the crystals themselves can be modified to display different surface and interior components via amino acid substitutions in CJ, which may have future implications for complex delivery. As demonstrated in this chapter, the crystals can be conjugated to fluorophores which will not disperse when they encounter a membrane, thereby permitting longer imaging timescales in living systems. The crystals are not visibly damaged after days of exposure to a complex tissue model, nor was any decrease in fluorescence observed, and no cytotoxicity from the crystals was

detected following their exposure to tissue. Another potential benefit of immunologically inert crystals for lung delivery is that they would not contribute to the overactivated immune system pathology common to many respiratory diseases. CJ crystals can be loaded with a broad range of biologically relevant substances, such as nucleic acids, proteins, and enzymes, enabling delivery of a diverse spectrum of pharmaceuticals. While the large pore size of CJ crystals permits their use as a carrier for macromolecules, such as DNA, RNA, and proteins, it also does not preclude small molecule guests, as evidenced with LPS in this chapter.

A priori, we considered several potential mechanisms for adverse effects from the crystals themselves: I) Because the crystals are composed of a protein derived from *C. jejuni*, they might negatively interact with tissue due to the proteins' microbial origin and the repetitive surface of the crystals; II) Because CJ is a putative polyisoprenoid binding protein, it is conceivable that CJ crystals could uptake and bind small molecules found in mammalian tissue, including a range of steroid molecules and sex hormones; III) Since the CJ protein was expressed in *E. coli*, it was possible that the crystals would be contaminated with endotoxin. Fortunately, crystallization in very high ammonium sulfate concentration is a strong form of purification, and the downstream cross-linking, quenching, and washing of the CJ crystals were likely to further remove any contaminants. This was reinforced by our observation within this study, that *E. coli*-derived lipopolysaccharide diffuses from CJ crystals on the order of minutes to hours; IV) Finally, the chemical cross-linking of the crystals could result in carryover of toxic cross-linkers, though compared with traditional aldehyde cross-linkers such as formaldehyde and glutaraldehyde, the EDAC cross-linker used in this study was considerably less

reactive. Furthermore, Hartje et al. discussed methods for limiting cytotoxicity for building blocks of EDAC cross-linked CJ crystals in a previous review.[119] Finally, in the present study, the host crystals appeared to be biologically inert; only LPS-loaded crystals induced a noticeable and significant physiological response. To determine whether there were any adverse effects of CJ crystals, *ex vivo* tissue slices were evaluated for number of permeable cells compared to total number of cells as a measure of cell death. No change in tissue health measured by cell death was observed in crystal treated slices. Additionally, the innate B cell population was compared in untreated slices to slices treated with unloaded crystals, LPS-loaded crystals, or LPS alone. Only crystals loaded with LPS and LPS by itself had an effect on the B cell population. These experiments establish the feasibility of using the crystal platform as a delivery system for biologically active small molecules. LPS was selected as a test compound due to its well-characterized and potent immunostimulatory effects, providing a sensitive readout of delivery efficacy rather than a candidate therapeutic payload. The finding that crystal-loaded LPS increased B cell populations relative to unloaded controls confirms that the vehicle is capable of delivering functional cargo to lung tissue. Although the magnitude of response was lower than that elicited by soluble LPS, this difference likely reflects the distinct release kinetics of the crystal system, which may distribute the stimulus over a longer time frame rather than producing a sharp peak in exposure. Importantly, unloaded crystals did not alter B cell numbers, supporting their suitability as a neutral carrier. Taken together, these data highlight the potential of crystal-based delivery to modulate tissue responses in a controlled fashion and establish a foundation for testing other small molecules with translational relevance.

Here, PCLS were used for initial basic feasibility and biocompatibility testing of CJ crystals with live organ tissue. When LPS was loaded into crystals, lung slices that were treated with those crystals displayed an increase in the number of CD19-imunoreactive B cells, consistent with previous literature.[195,206,207] Because animals were perfused through the heart with warm PBS after death, no recruitment from the vasculature could have occurred, indicating that the increase in B cells was likely a result of proliferation. This B cell population increase was smaller than the population increase generated by treating PCLS with LPS in the media, and may indicate a more gradual release (i.e., lower dose) mechanism from the crystals. Conversely, unloaded crystals added to PCLS did not influence CD19+ B cell populations, consistent with a lack of immune response from the host crystals over 48 h. This lack of immune response is particularly important for potential biomedical applications because most existing carrier molecules have innate adjuvant properties, potentially resulting in off-target immune responses.

Similarly, crystals interacted with the PCLS without affecting health as visualized by maintenance of gross morphological characteristics of the tissue, or cell death. Under normal conditions,[187,208] healthy tissue can be maintained over several days without treatment, and the addition of empty crystals did not change any tested aspect of tissue health. Crystals clearly penetrated the porous protective collagen layer that covered the PCLS, with some immediate deposition that increased over time. Across 96 hours, there were no observed increases in cell death, and B cell numbers did not differ in slices treated with unloaded crystals compared to untreated slices. These two factors justify future investigation for the delivery of authentic therapeutic molecules. To directly quantify the rate of release of guest LPS from microcrystals, we diluted LPS-saturated

microcrystals (~ 300 nm in diameter) in PBS ten-fold and monitored guest release into the surrounding solution over a period of 12 hours. We observed a net increase in solution fluorescence, and directly quantified the well concentration, while ensuring that the crystals themselves remained out of the light path (Figure 4.5D,E). Confocal imagery showing a net decrease in fluorescence across three large LPS-loaded crystals (> 100 μm in diameter) (Figure 4.5A-C), along with the increase in LPS concentration in the wells containing diluted LPS-loaded microcrystals (Figure 4.5D), and the observed B cell response to LPS-loaded crystals in tissue slices (Figures 4.6 and 4.7), all suggest that guest LPS diffuses from the crystals over a period of several hours to days (consistent with a burst release profile characteristic of mesoporous scaffolds), after which LPS concentration reaches equilibrium between the crystals and surrounding solution. While this is not consistent with an extended-release profile, it does suggest that the crystals are able to release guest LPS following tissue exposure. The absence of a B cell response to naïve crystals additionally suggests that endotoxin carryover through CJ microcrystals is unlikely. A significant limitation of this study is that it does not evaluate cellular uptake, or intracellular activity, of LPS-loaded CJ microcrystals. Instead, the crystals were evaluated for their ability to release LPS into surrounding tissue, by measuring local B cell responses to LPS. Rational re-engineering of CJ is required to target crystals to specific extracellular domains and retain and release biomolecules on a tunable timescale.

With respect to clinical application, at least two significant obstacles related to intravascular delivery of porous protein microcrystals remain. The first is the ability to precisely control crystal aspect ratio (that is, the ratio of the crystal height to the crystal diameter), which, depending on the batch growth conditions, would result in flatter, more

discoidal crystals, or longer, more cylindrical crystals. This is especially relevant in intravascular transit, as previous work has demonstrated that discoidal nanoparticles remain in circulation for significantly longer periods of time than cylindrical or hemispherical nanoparticles, which are more quickly sequestered into the liver.[90] Aspect ratio appears to be tunable for CJ crystals, and in fact, long, needle-like crystals, have been observed in a number of sitting-drop wells, although this effect remains difficult to reproduce. The second obstacle is precise control over the mechanical deformability and overall stiffness of the crystals. Previous studies have demonstrated that deformability of nano- and microparticle carriers is desirable, as this enables them to squeeze through narrow capillary beds and ultimately traverse them, analogous to red blood cells.[209] Fortunately, the extent to which CJ crystals are chemically cross-linked influences the deformability and overall hardness of the crystals;[210] relatedly, we have previously attempted to loop incompletely cross-linked CJ crystals, and have observed consistencies ranging from gel-like, to rubber-like, to completely non-deformable. Therefore, the choice of EDAC as a cross-linking agent was partly based on the relatively longer time required to fully cross-link the crystals, when compared to glutaraldehyde or glyoxal cross-linkers.

Aside from the protective effects of crystals as a vessel for delivery of therapeutics to tissues and the benefits of the larger pore size, the versatility of this model suggests that there are a large number of unexplored applications for CJ crystals, particularly in the biomedical realm. First, they may be useful as a carrier for tracer dyes. Because they have no demonstrated immunostimulatory properties as demonstrated here and can be engineered to hold such a broad range of compounds it is not unreasonable to think that in

future studies, they could be loaded with tracer dyes to increase the dose that can be given to patients and increase visibility or prolong time that imaging can be performed. Additionally, they could be engineered to uptake high concentrations of unwanted molecules produced in illnesses or possibly by viruses. Additionally, it is possible that CJ crystals could be re-engineered or modified to enhance cellular uptake. For instance, previous work by Yang et al. with Cry3Aa crystals suggests that the introduction of positively charged surface residues can facilitate endosomal escape of microcrystals, following endocytosis.[91] However, to perform these studies, it is important to first determine a baseline for interactions of the crystals in biological systems.

In conclusion, while the results described in this chapter do not suggest that CJ crystals are capable of prolonged, extended release of guest LPS into surrounding tissue, the absence of a specific immune response to the crystals themselves (Figure 4.6), along with the demonstrable release of LPS from the crystals, both *in vitro* (Figure 4.5) and *ex vivo* (Figures 4.6 and 4.7), nevertheless reinforces their potential as a therapeutic delivery platform for biologically-relevant molecules. Rational, structure-guided re-engineering of CJ crystals may allow for more precise guest-crystal interactions for more biomedically relevant molecules, potentially enabling extended release and cell-specific targeting.

CHAPTER 5: Bioluminescent Trace Labeling of Porous Protein Microcrystals for Evaluating Pharmacodynamics

5.1 Overview

This chapter investigates the biodistribution and persistence of cross-linked porous protein microcrystals in vivo using bioluminescence imaging. By coupling the NanoLuc luciferase enzyme to the CJ crystal scaffold, we sought to determine whether these protein-based crystalline materials remain systemically dispersed, accumulate in specific organs, or become locally retained following intravenous injection. Ex vivo imaging of dissected organs at 72 hours post-injection revealed relatively uniform radiance across most tissues; however, persistent signal in the hindlimbs of several animals suggested partial entrapment of crystals within skeletal muscle microvasculature. Statistical evaluation using ANOVA, Kruskal–Wallis, and post hoc testing confirmed that, while organ-level differences were not significant after outlier removal, the spatial pattern of emission observed in whole-animal imaging supports a model of microvascular retention. These results establish the foundation for considering CJ microcrystals as potential localized depot systems capable of sustained, site-specific release of therapeutic payloads. Beyond biodistribution, this chapter highlights the physical and physiological determinants that govern the fate of solid, protein-based micro- and nanoparticles following systemic administration.

5.2 Introduction

Porous micro- and nanoparticles have emerged as highly versatile platforms for therapeutic delivery, offering significant advances in drug loading capacity[211] and controlled release profiles.[212] Innovations in synthesis techniques—such as sol-gel

processing,[213] emulsion templating,[214] and microfluidics[215,216]—have improved particle uniformity and scalability for clinical applications. Additionally, surface functionalization strategies allow for active targeting to diseased tissues,[117,217,218] reducing systemic toxicity,[219] and thereby improving therapeutic efficacy. These features position porous carriers as promising candidates for addressing challenges in oncology, immunotherapy, and regenerative medicine.

Within the larger class of porous particles, porous protein microcrystals have recently gained attention as innovative platforms for therapeutic applications, offering a unique combination of biocompatibility[44] and structural precision.[45,220] Advances in crystallization techniques have enabled the formation of stable, well-ordered protein lattices with defined pore networks capable of encapsulating a variety of bioactive compounds. Large-pore protein microcrystals (pore diameters > 5 nm) can enable sustained release of macromolecular cargo, protect guest therapeutics from degradation, and potentially enable targeted delivery with additional protein engineering of the crystal surfaces. Recent work has demonstrated the successful incorporation of small molecules,[11] peptides,[10] and biologically-active proteins[68,91] into protein crystal matrices.

In chapter 2, we demonstrated that CJ microcrystals can efficiently adsorb and retain single- and double-stranded DNA and RNA, with conditional release triggered by high ATP concentrations. CJ crystals can also be further modified through covalent chemistries or genetic fusion. Given these structural and functional attributes, CJ microcrystal variants represent a potential family of protein-based carriers for therapeutic delivery. The internal crystalline order of these materials permits rational design of the biomaterial to an unusual degree. Crystal growth permits tunable particle geometry to a variety of sized particles, particles that nonetheless share

identical nanostructure. The open honeycomb pore network permits macromolecule uptake without loss of encapsulation capacity. Given these unique properties, it is important to take the first steps in evaluating pharmacokinetic behavior *in vivo*, including biodistribution, clearance, and possible tissue retention. Obtaining initial data for these properties constitutes a critical first practical step before extended studies to evaluate CJ as a potential platform for targeted or sustained-release delivery of biologics and other macromolecular therapeutics.

Trace-labelling of therapeutic nanocarriers is necessary for evaluating their *in vivo* biodistribution, pharmacokinetics, and clearance pathways.[221] A variety of labelling techniques have been developed to enable sensitive and specific tracking, including radiolabelling, fluorescent dyes, and magnetic resonance contrast agents. Radiolabelling with isotopes such as ^{64}Cu, ^{89}Zr, or ^{99m}Tc enables highly quantitative, whole-body imaging using PET or SPECT,[222] but often requires complex handling and raises safety concerns due to radiation exposure. Alternatively, fluorescent labelling using organic dyes or quantum dots[223] provides high spatial resolution for *ex vivo* tissue analysis and intravital microscopy but may suffer from photobleaching or signal quenching in biological environments.[224] Magnetic resonance imaging (MRI) tracers, such as gadolinium complexes[225] or iron oxide nanoparticles,[226] offer non-invasive tracking without ionizing radiation, though their sensitivity is typically lower. To overcome limitations in sensitivity and tissue penetration, bioluminescence-based approaches have gained popularity, particularly through the use of luciferase enzymes. Nanocarriers can be trace-labelled by incorporating luciferase proteins or luciferase-expressing constructs, enabling real-time, non-invasive imaging with minimal background signal. This method is especially valuable for longitudinal studies in small animal models, as luciferase emits light only in the presence of its substrate, allowing temporal control over signal generation. Furthermore,

luciferase-based labelling is amenable to genetic encoding in cell-derived carriers, such as exosomes or engineered extracellular vesicles, facilitating more accurate pharmacokinetic profiling. The high sensitivity, biocompatibility, and dynamic range of bioluminescence make it an ideal tool for evaluating nanocarrier behaviour *in vivo*.

In this chapter we describe engineered CJ microcrystals to enable site-specific covalent installation of guest proteins and enzymes, using SpyCatcher/SpyTag. SpyCatcher and SpyTag are two complementary halves of a re-engineered version of the CnaB2 domain, from *Streptococcus pyogenes*, originally developed by the Howarth lab,[71,72] and which have since been used for biomaterials applications,[227,228] cell-imaging[155] and protein association and localization studies,[229] and conjugation of antigens to therapeutic carriers.[3] The hybrid biomaterials described in this chapter (as in chapter 3) are composed predominantly of wild-type CJ protein, doped with a variant of CJ with SpyTag003 (third generation)[72] at the C-terminus ("CJ-SpyTag") (Figure 5.1D, Supporting Table S1). Appending SpyTag to CJ allows for the modular conjugation of guest proteins outside or inside of crystals, simply via genetically fusing SpyCatcher to either terminus of the guest.[70,72,149]

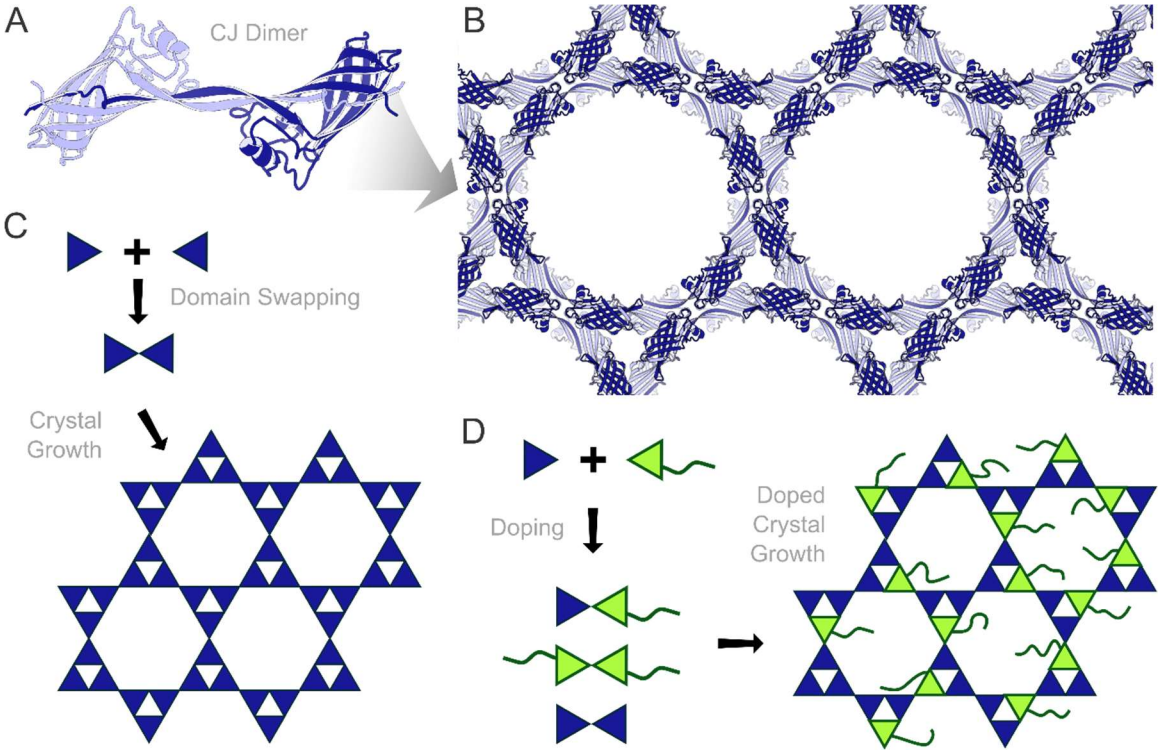

Figure 5.1: A, CJ readily dimerizes via domain swapping at the N-terminus. **B, C,** This domain swapping by CJ facilitates the growth of P 6 2 2 crystals, characterized by large, 13 nm axial pores. **D**, Doping of CJ crystals with the fusion protein CJ-SpyTag003 results in random incorporation of CJ-SpyTag003 alongside wild-type CJ. As a result, the crystal displays SpyTag003 to the major pore interior.

Intravenous administration of NanoLuciferase-labeled CJ microcrystals revealed a distinct pattern of *in vivo* localization. Within minutes of injection, bioluminescent signal was detected in the pulmonary region of all animals, indicating rapid first-pass accumulation in the lung vasculature. Over the following hours, this pulmonary signal declined markedly. The signal in the hindlimbs also decayed with a short half-life but became the dominant site of emission by 8 hours post-injection due to a higher end-time signal. This description was consistent across all six mice. The elevated end-time luminescence in the distal skeletal muscle beds (relative to lungs) suggests that these tissues might retain a small fraction of the microcrystals for extended times. These observations provide real-time evidence that micron-scale protein crystals can access multiple tissues after systemic delivery and suggest the importance of vascular geometry in determining their ultimate fate. It is also important to mention that the tail injection sites

remained quite luminescent, suggesting that a population of the crystals remained near the injection site, either due to size or geometry. Consistent with a baseline biocompatibility for particles composed of proteins, no change in mouse behavior or health was noted between the initial injection, and sacrifice at 72 hours post-injection.

5.3 Methods

5.3.1 CJ SpyCrystal growth, cross-linking, and conjugation testing

Both wild-type CJ and doped CJ SpyCrystals were grown using both sitting drop vapor diffusion and batch crystallization, as described previously.[9,34,122] Briefly, one volume of concentrated CJ protein + CJ-SpyTag protein (equimolar concentration) was combined with five volumes of precipitant buffer (3.5 M ammonium sulfate, 100 mM HEPES, pH 7.0) in a single 1.5 mL microcentrifuge tube. The crystals were allowed to grow for 24 hours at room temperature. Following growth, the crystals were pelleted by centrifugation (2,000 x g for 5 minutes), then washed in 4.2 M trimethylamine-N-oxide (TMAO) and then resuspended in a cross-linking buffer (1% glyoxal, 25 mM p-dimethylaminobenzaldehyde (DMAB), 4 M TMAO) and incubated at room temperature for 15 minutes. The cross-linking reaction was then quenched via washing the crystals in 1 M hydroxylamine, 25 mM DMAB for 1 hour. Following growth, cross-linking, and quenching, the crystals were resuspended in sterile 1X PBS, supplemented with 0.1 mg mL^{-1} SpyCatcher003-NanoLuciferase. The crystals were then allowed to soak overnight at 4 °C, after which they were washed and resuspended in sterile 1X PBS. Crystal size distribution was obtained using scanning electron microscopy (SEM) on a JEOL JEM-2100F Transmission Electron Microscope and tunable resistive pulse sensing (TRPS) by qNano Gold (Izon Science) (Supplemental Figure 5.1).

5.3.2 Validation of *in vitro* SpyCatcher-SpyTag-mediated guest capture

Following synthesis, cross-linking, and glyoxal quenching, a single large wild-type CJ crystal was soaked overnight at room temperature in a buffer containing nickel ("Buffer A," 50 mM HEPES, 300 mM NaCl, 10 mM nickel sulfate, 10% glycerol, pH 7.5). After soaking in this buffer, the crystal was looped and moved into 6XHis-Nanoluciferase (~5 mg mL^{-1}) and soaked overnight at 4 °C. After overnight loading, the crystal was then washed by looping twice through 0.3 mL of buffer A, then imaged under confocal microscopy with a blue light filter. Furimazine (~50 μM) was added to the buffer, and the crystal was imaged over a 13 minute window.

To validate the feasibility of in-crystal SpyTag-SpyCatcher conjugation we expressed a fusion protein: SpyCatcher003-superfolderGFP and performed a multistep protocol. First, both wild-type CJ and doped CJ SpyCrystals were grown using sitting drop vapor diffusion; the crystals remained un-cross-linked following growth. Following growth, two large crystals of each type were looped twice through 0.3 mL of wash buffer (3.6 M TMAO, 50 mM HEPES pH 7.5), before incubation in 0.5 mg mL^{-1} purified SpyCatcher003-sfGFP for 1 hour at room temperature. After this incubation, the crystals were washed three times in 0.3 mL of the growth buffer (3.4 M ammonium sulfate, 100 mM Bis-Tris pH 6.5). The crystals were then each individually dissolved in 20 μL of nuclease-free water and run in separate lanes (one crystal per lane) on a pre-cast Mini-PROTEAN 4–20% polyacrylamide gel (Bio-Rad, # 4561095) for 90 minutes at constant 120 volts. The gel was then imaged directly through the transparent plastic sheath via GFP transillumination.

5.3.3 Intravenous injections of luminescent CJ SpyCrystals

To evaluate the *in vivo* biodistribution of CJ microcrystals, CJ microcrystals labeled with SpyCatcher-Nanoluciferase were injected into the tail vein of BalbC mice (n=6). Prior to the start

of the experiment, mice were marked on their ears and/or tail for identification and weighed. A solution of 100 μg of CJ microcrystals, labeled with SpyCatcher-Nanoluciferase, was pre-mixed with furimazine (50 μM final concentration) and suspended in a final volume of 100 μL of 1 x phosphate buffered saline at pH 7.5.

For injection and imaging, mice were anesthetized with isoflurane. Mice were injected with 100 μL in the tail vein of this solution immediately after it was mixed. Mice were then placed in an IVIS Spectrum (Revvity Inc, Waltham, Massachusetts) within 5 minutes of injection to obtain distribution images (time=0). Anesthesia was maintained during imaging by delivering isoflurane via a nose cone in the IVIS instrument and held in a chamber with constant 37ºC. The animal was placed in a cassette to secure it, allowing for it to be moved during imaging without the risk of injury or dislodging it from the anesthesia. Whole body images were taken with mice in the supine and prone positions. Multiple fields of view were taken to include all of the organs and regions of the body. Chemiluminescence was monitored via IVIS imaging at 0, 1, 4, 8, 24, and 48 hours post-injection. Mice were injected with additional furimazine (50 μM in PBS, 0.1 mL) at 8, 24, and 48 hours prior to imaging. Following image acquisition, mice were placed back in cages and continually monitored until they were ambulatory. Single IV injection volumes did not exceed 100 μL and the daily injection volume did not exceed 2 mL/kg/hour. Two mice were injected with furimazine alone to serve as negative controls following the above procedures. All animals were humanely euthanized 72 hours after the initial injection. Tissues (heart, kidney, liver, lung, skeletal muscle, and spleen) were removed and placed in a Petri dish for further imaging. Once excised, 100 μL of furimazine (50 μM) was applied to the outside of all tissues. The tissues were then placed in the IVIS imager and chemiluminescence was measured. All

animal work in this study was completed under Colorado State University IACUC approved protocol #5056.

5.3.4 Statistics

Background-corrected total radiance (photons s^{-1}) from *ex vivo* organs was analyzed using both parametric and nonparametric statistical approaches. Data were first log_{10}-transformed to correct for skew and heteroscedasticity. Normality within each organ group was then evaluated using Kolmogorov–Smirnov test, and homogeneity of variance was assessed using Levene's test. For each experimental condition (with or without furimazine substrate), differences in the mean log-transformed radiance among organs were evaluated by one-way ANOVA, followed by Tukey's HSD post hoc test to identify pairwise differences. Results were additionally confirmed using the Kruskal–Wallis test. All statistical analyses were conducted in Python using the SciPy and Statsmodels libraries.

5.4 Results

5.4.1 CJ SpyCrystals modified with Nanoluciferase demonstrate bioluminescence

After soaking CJ crystals in 6XHis-Nanoluciferase overnight in a nickel supplemented buffer (Figure 5.2A,C-E, then washing and adding furimazine under confocal (without illumination), we observed light production along the outer surface of the crystal, demonstrating the feasibility of Nanoluciferase activity and light production within the CJ crystal scaffold (Figure 5.2E-H). Furimazine solubility remained low over the course of the imaging, resulting in some precipitation (visible in the image at 4:32). Notably, the crystal interior remained largely dark during the acquisition, as expected for a large crystal due to transport limitations- furimazine must bypass the surface guest NanoLuc in order to react with the interior guest NanoLuc. We anticipate no comparable transport limitations for microcrystals; light production in CJ-

SpyCrystals loaded with SpyCatcher-Nanoluciferase fusion guest (and subsequently washed with 10 mM EDTA) was additionally validated in subsequent experiments (data not shown).

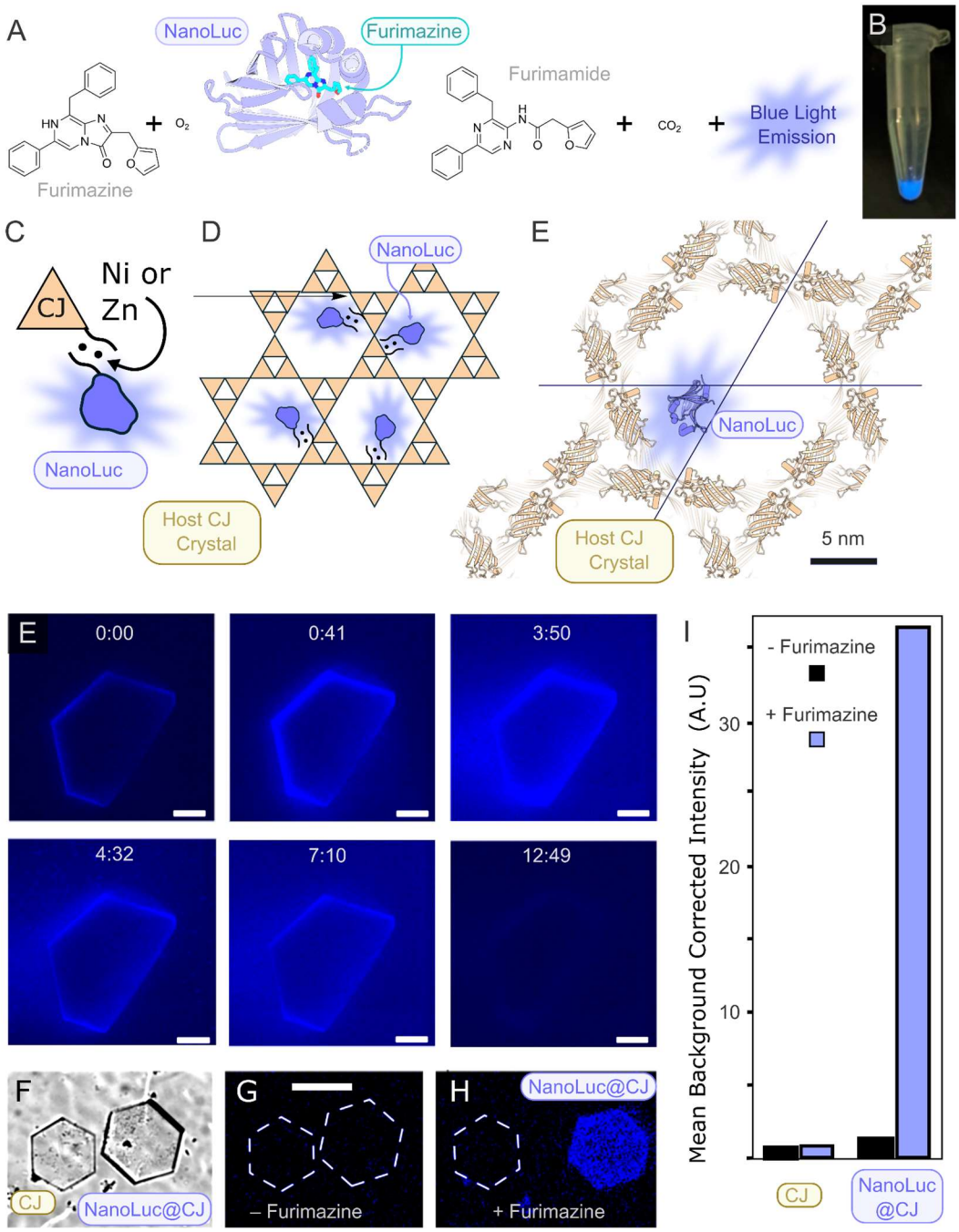

Figure 5.2: A, C-D, Schematic illustrating the overall placement of the Nanoluciferase guest relative to the CJ greater axial pore. In this instance, the guest is held in place via tethering between the histidine tag on Nanoluciferase, and the histidine tag from CJ, via a communal nickel interaction. **B**, Light production from Nanoluciferase is visible by eye, following addition of 50 μM furimazine (Nanoluciferase concentration = 0.5 mg mL^{-1}). **C-D,** Schematic illustrating non-covalent tethering of 6xHis-Nanoluciferase (blue) within a CJ pore (beige). **E,** A single large CJ SpyCrystal, following overnight soak with 6xHis-Nanoluciferase, and imaged via confocal microscopy over a ~13 minute window, following addition of furimazine (50 μM final concentration) at t = 0:00 minutes. Scale bar = 100 μm. **F-H**, Two wild-type CJ crystals (one soaked in 6xHis-Nanoluc, right, and an empty control crystal, left), imaged via confocal microscopy before and after addition of furimazine (50 μM final concentration). **I,** Mean background corrected intensities of both the control and loaded crystals, before (black) and after (blue) addition of furimazine.

5.4.2 *In vitro* validation of SpyCatcher003-sfGFP guest capture by SpyCrystals

To validate the intended *in vitro* capture method for SpyCatcher003-Nanoluciferase, we soaked two large, un-cross-linked wild-type CJ crystals and two large, un-cross-linked CJ SpyCrystals in SpyCatcher003-sfGFP. Following incubation, each crystal was washed multiple times in the mother liquor (supplemented with 10 mM EDTA), then dissolved in 20 μL of nuclease free water. After dissolving, the resulting mixtures were run in independent lanes on an SDS-PAGE gel. For the wild-type crystals, we observed only a single fluorescent band at 42.4 kDa, indicative of SpyCatcher003-sfGFP alone, while for the CJ SpyCrystals, we also observed the appearance of a higher molecular weight band (64.6 kDa), consistent with successful covalent capture of the fluorescent guest (Figure 5.3A-G). For additional validation of in-crystal conjugation, cross-linked microcrystals were used. Specifically, wild-type CJ crystals and CJ SpyCrystals (two separate syntheses of each) were each soaked in SpyCatcher003-sfGFP, then washed multiple times overnight with buffered 10 mM EDTA (to minimize the presence of non-covalent entrapped fluorescent guest proteins). We then imaged directly via blue light transillumination. Higher green fluorescence was immediately obvious in the CJ SpyCrystals, but not the wild-type CJ crystals, indicating that covalent capture only occurs in the doped crystals (Figure 5.3H).

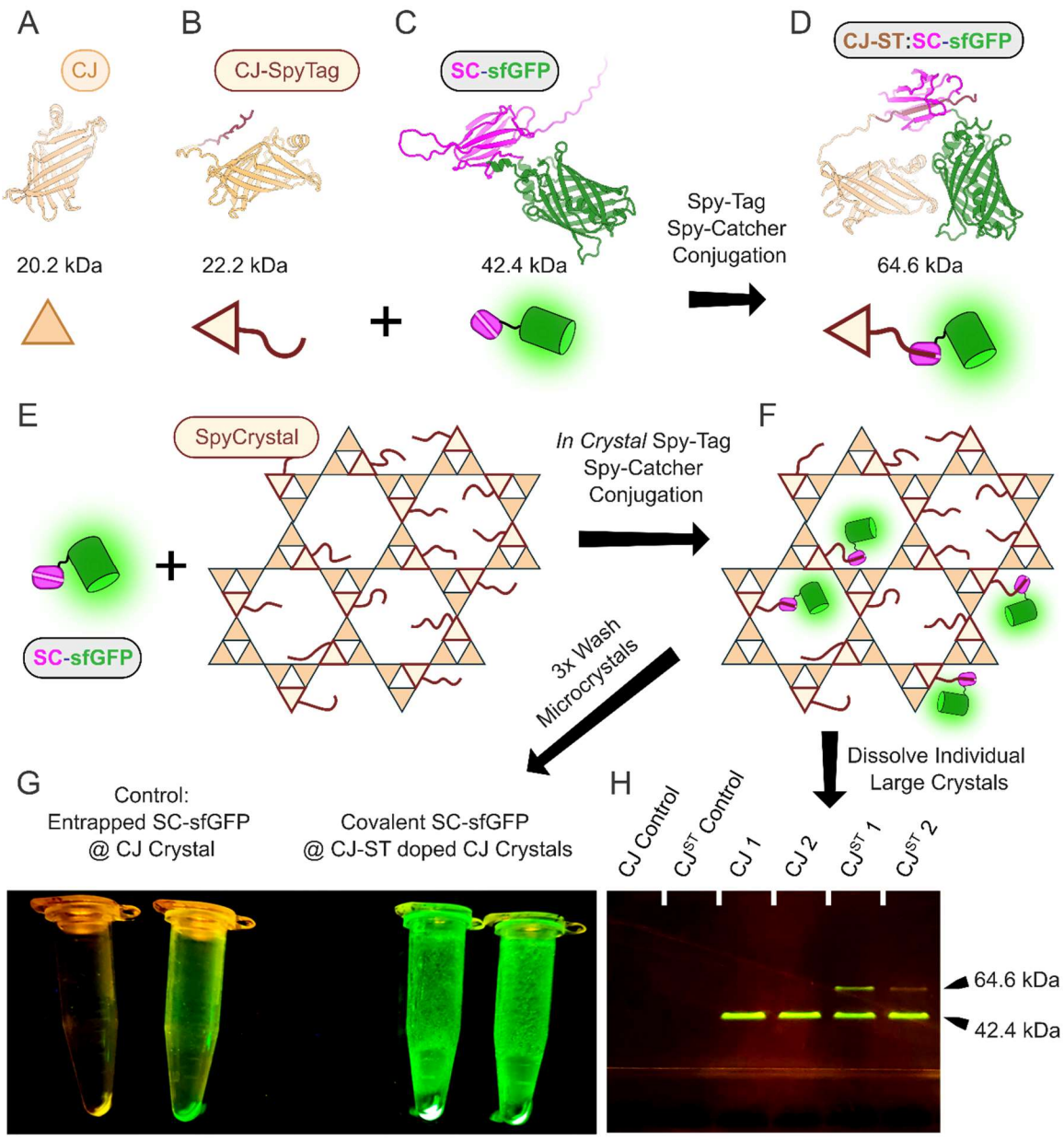

Figure 5.3: AlphaFold3 (AF3) prediction of **A,** wild-type CJ monomer; **B,** CJ-SpyTag003; **C,** SpyCatcher003-sfGFP; and **D,** CJ-SpyTag003:SpyCatcher003-sfGFP fusion product. A covalent bond is rapidly formed upon interaction of the two proteins, resulting in the formation of a higher molecular weight species (~64.6 kDa) with the same fluorescence as SpyCatcher003-sfGFP **E-F,** Schematic of interaction between SpyCatcher003-sfGFP and a doped CJ SpyCrystal. **G**, Cross-linked SpyCrystals, following incubation with SpyCatcher-sfGFP, selectively retain the SpyCatcher-fusion guest (right, in duplicate), while the wild-type crystals do not (left, in duplicate). **H**, SDS-PAGE of dissolved wild-type ("CJ 1," "CJ 2"), or CJ-SpyTag003-doped ("CJST 1," "CJST 2"), following soaking in SpyCatcher003-sfGFP, then washing, and finally dissolution, reveals covalent capture of the fluorescent guest only in the SpyTag-doped crystals, via the appearance of a higher molecular weight band (64.6 kDa).

5.4.3 Injected CJ-SpyCrystals revealed localization to the lungs and skeletal muscle

IVIS imaging of injected, anaesthetized mice demonstrated a consistent temporal sequence following tail-vein injection of luciferase-labeled CJ microcrystals (Figure 5.4). A significant amount of chemiluminescence was observed in the tail vein over the entire 48 hours, necessitating covering the tails during image acquisition. Besides the immobile signal in the tail, chemiluminescence was only observed in the lungs and hindlimbs in live animals. Immediately after injection, all mice exhibited a bright pulmonary signal consistent with first-pass lung exposure (Figure 5.4A).[230] A smaller signal in the hindlimbs was also brightest at the initial time point. The bioluminescence intensity in the lungs decreased rapidly over the first 4–8 hours, corresponding to clearance from the pulmonary tissue and vasculature. Quantitative fitting of the luminescence decay was consistent with the major decay component having an initial half-life of 0.29 hours ± 0.06 hours (Supplemental Figure 5.10). Meanwhile, the smaller signal in the posterior limbs also decayed (0.26 hours ± 0.11 hours half-life) but became more visible (Figure 5.4A,B) due to a higher end-time baseline luminescence. Particularly between 1 and 8 hours post-injection, we observed a strong relative signal emerging in the hindlimbs in 4 of the 6 mice. Quantitative analysis of total radiance in the lungs and hindlimbs demonstrated a strong time-dependent interaction ($p < 0.001$), with luminescence in the lungs declining by more than two orders of magnitude, while hindlimb luminescence decreased by a factor of 17.8. By 24 hours, the difference between thoracic and posterior regions approached, but did not reach, statistical significance (paired t-test, $p = 0.075$), suggesting preferential retention or slower clearance of microcrystals from skeletal muscle vasculature. Notably, the smooth decay in the signal (Figure 5.4B) occurred despite repeated administration of furimazine substrate, consistent with the change in signal reflecting microcrystal localization rather than fluctuations in enzyme activity.

Control animals injected with soluble SpyCatcher-NanoLuciferase showed diffuse, rapidly declining luminescence without focal hindlimb enrichment. Animals injected with furimazine alone, serving as negative controls, did not show any luminescence in either the thoracic or posterior hindlimb ROIs (data not shown).

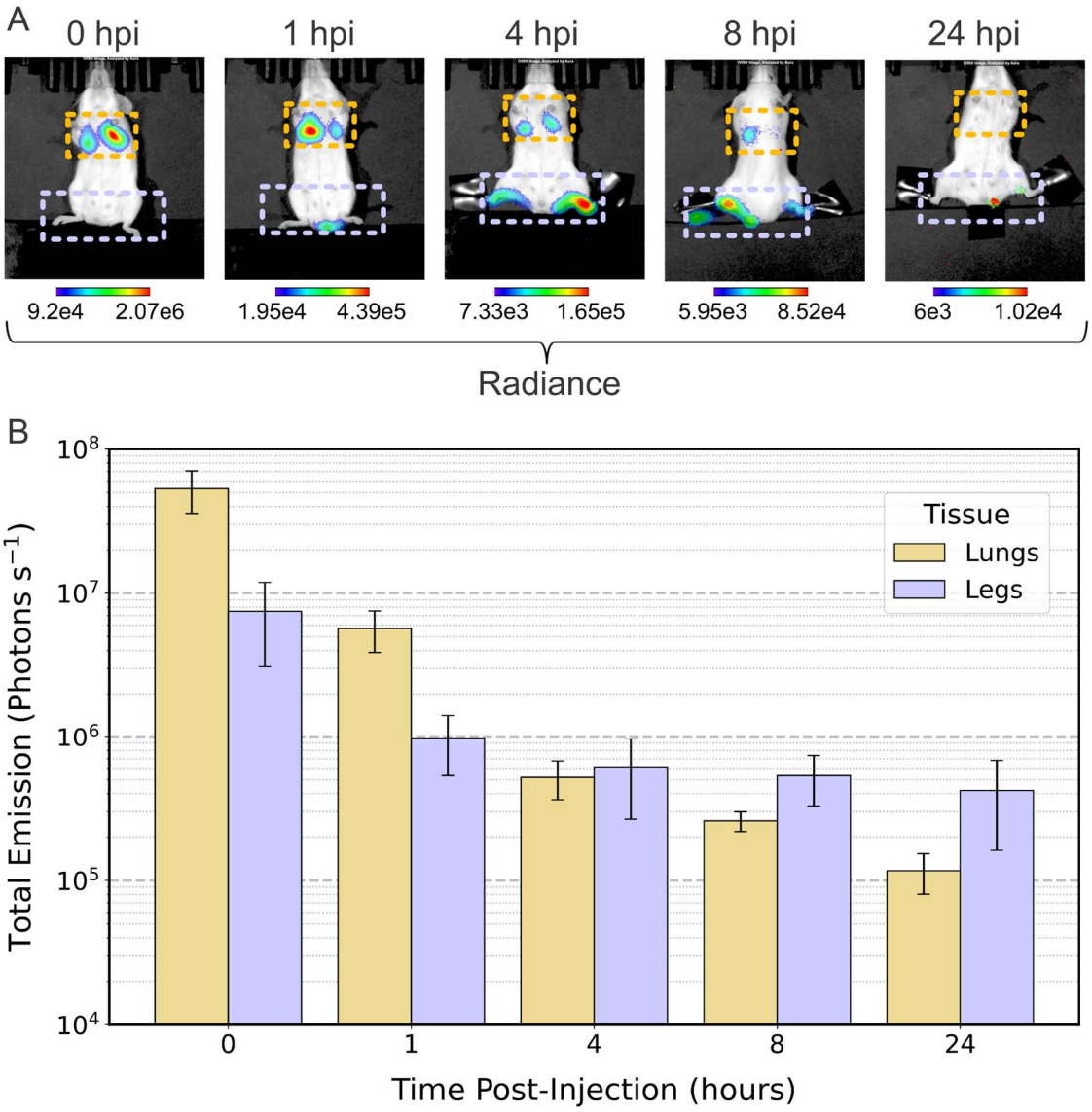

Figure 5.4: A, *In vivo* images and background-corrected radiance of mouse 4, following injection with Nanoluciferase-labeled CJ SpyCrystals, imaged over 24 hours post-injection, demonstrating pulmonary clearance of CJ SpyCrystals over the first 4 to 8 hours, followed by retention in the hindlegs. **B**, Background-corrected, log-scaled emission of both the lungs (beige) and haunches (periwinkle) over a 24 hour period. For full ROI annotation of these images see Figures S2-S3.

Animals were observed multiple times a day post-injection and appeared normal. No changes in behavior were noted; animals displayed typical grooming and social behaviors, indicating that CJ crystals do not cause pain or discomfort in the two days post IV administration, and supporting our hypothesis that CJ crystals have a baseline biocompatibility that warrants further study.

5.4.4 *Ex vivo* organ luminescence reveals higher localization to skeletal muscle

Ex vivo imaging revealed measurable bioluminescent signal in several of the organs, following addition of furimazine substrate. Total radiance was obtained by applying a uniformly-sized, circular region of interest (ROI) around each organ in Aura 4.5.0 (Figures S4-S9). Log-transformed radiance values were normally distributed across all organ groups (Kolmogorov–Smirnov, $p > 0.6$), and variances were statistically homogeneous in both conditions (Levene's test, $p > 0.05$).

Under the no-furimazine condition, total radiance did not differ significantly among organs (one-way ANOVA, $F(5, 27) = 1.58$, $p = 0.20$; Kruskal–Wallis, $p = 0.49$). This confirmed that basal background luminescence was comparable across tissues. Furthermore, after addition of furimazine, the overall model reached significance (ANOVA, $F(5, 27) = 3.03$, $p = 0.027$; Kruskal–Wallis, $p = 0.043$), suggesting organ-specific differences in luminescent intensity (Figure 5.5B). Post hoc testing indicated that the muscle group exhibited substantially higher radiance compared to other organs (notably liver, spleen, and heart). Inspection of raw data, however, revealed a single extreme value corresponding to one mouse with an abnormally bright muscle signal (~2.9×10^7 photons s^{-1}). When this outlier was excluded, the apparent organ effect was no longer significant (ANOVA, $p = 0.089$; Kruskal–Wallis, $p = 0.090$). After outlier removal, radiance values at 72 hr were statistically similar across all tissues, consistent with

clearance of the microcrystals or deactivation of the NanoLuc enzymes sheltered within the host microcrystals.

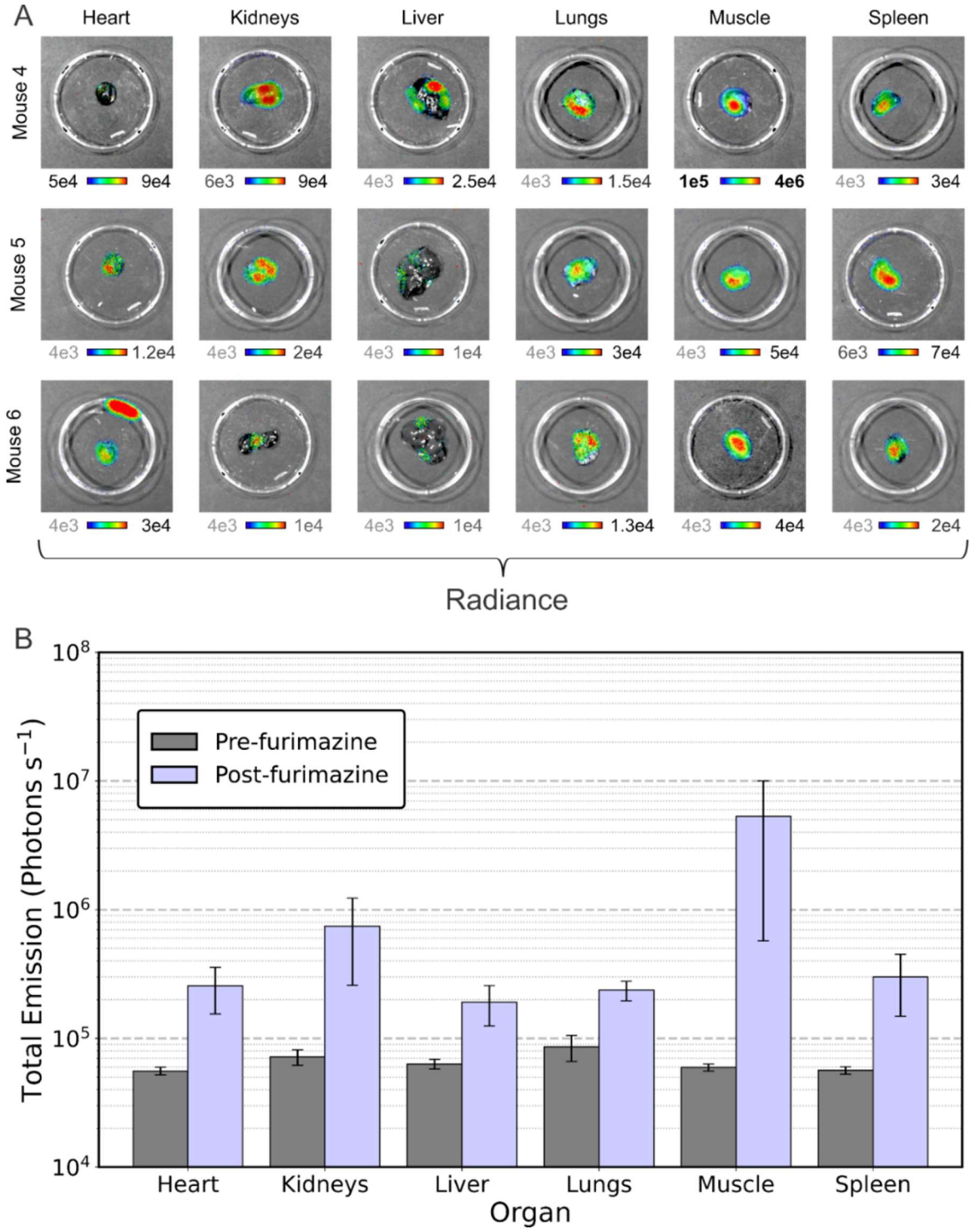

Figure 5.5: A, *Ex vivo* imaging and background-corrected radiance for individual organs excised from necropsied mice (cohort 2), following addition of 1 µg of furimazine in 100 µL of PBS. **B,** Log-transformed, averaged (n=3 for kidneys, n=6 for heart, liver, lungs, muscle, and spleen), background-

corrected radiance by organ type, before (gray) and after (blue) addition of furimazine to each excised organ. Error bars represent the standard error from the mean.

5.5 Conclusions

In this chapter, we describe a method of tagging CJ microcrystals with a NanoLuciferase reporter following tail vein injection, demonstrating both the modularity and versatility of this bioconjugation platform. We initially demonstrated that CJ crystals containing genetically encoded SpyTag motifs could be efficiently functionalized *in vitro* through guest-loading of purified SpyCatcher-fusion proteins, including SpyCatcher-sfGFP and SpyCatcher-NanoLuciferase. These experiments established that the SpyCatcher–SpyTag chemistry proceeds efficiently within the crystals, enabling post-crystallization installation of active protein cargos. Confocal fluorescence imaging, SDS-PAGE, and plate reader assays confirmed covalent guest installation in the crystals, consistent with the 13 nm solvent channels that permit free diffusion of folded macromolecules. Expanding the scope of this chapter beyond *in vitro* work, our focus then shifted toward understanding how labeled microcrystals behave in a living system—specifically, whether their size, geometry, and the biological characteristics of the CJ protein itself influence biodistribution, clearance kinetics, and organ-level localization following systemic administration. The incorporation of a SpyTag fusion protein into the crystalline lattice of CJ microcrystals represents a significant advance in the engineering of modular protein-based materials for molecular encapsulation and delivery. Unlike most previously described porous protein crystals—which typically permit only small-molecule diffusion through narrow solvent channels—CJ crystals possess large, continuous pores measuring approximately 13 nm in diameter,[30] allowing unhindered diffusion of folded proteins and other macromolecular guests (Figure 5.1A-C). This feature distinguishes the CJ system from prior examples, such as the Cry3aa-based SpyTag crystals developed by the Chan group, which possess much smaller

internal channels.[68,70,202] Smaller pore diameter limits access to the crystal interior and confines guest proteins primarily to the surface. By doping the CJ lattice with a SpyTag-bearing variant, this work establishes a modular, covalent anchoring mechanism throughout a structurally open, high-capacity framework, enabling site-specific installation of functional proteins within a highly-ordered crystal scaffold.

While confocal imaging experiments in controlled buffer conditions confirmed efficient guest loading and stable covalent attachment of SpyCatcher-fusion proteins such as SpyCatcher-sfGFP and SpyCatcher-NanoLuciferase, they could not address critical questions surrounding pharmacokinetic behavior, tissue distribution, and clearance pathways in living organisms. The physical parameters of CJ microcrystals—particularly their micron-scale dimensions and faceted geometry—suggest that size and shape may strongly influence how they traverse the vasculature, interact with endothelium, or become sequestered within specific organs.[90] Furthermore, understanding if crystalline particulates circulate freely, become filtered by the mononuclear phagocyte system, or persist as localized depots is essential for evaluating their potential as delivery vehicles. By covalently coupling a guest NanoLuciferase within and on the host crystals, we enabled real-time, noninvasive bioluminescence tracking following intravenous administration, providing direct insight into biodistribution dynamics that cannot be captured by *in vitro* assays.[231] This transition from static guest-loading experiments to *in vivo* imaging therefore represents a critical bridge between materials design and physiological performance, offering the first quantitative view of how large-pore protein microcrystals behave within systemic circulation.

In the first set of experiments, we observed rapid clearance of the crystals from the lungs over the first 8 hours (Figure 5.4). Between 1 and 8 hours post-injection, we observed a strong relative

signal in the hindlegs in 4 of the 6 mice (Figure 5.4A). The rapid decline of the thoracic signal supports efficient clearance from the lungs, likely via mechanical passage into systemic circulation rather than prolonged sequestration (Figure 5.4B). The later persistence of luminescence in the hindlimbs implies physical retention of a subset of particles within skeletal muscle microvasculature. This interpretation is consistent with the size range of CJ microcrystals—with larger crystals often exceeding 2 μm (Supplemental Figure 5.1)—approaching the diameter of capillary lumens (5–10 μm) and therefore capable of transient lodging or aggregation within narrow vascular channels. We hypothesize that the microcrystals may be immobilized and accumulate in the narrow capillaries associated with these regions. The shorter initial half-life associated with pulmonary clearance (0.29 hours ± 0.06 hours) exhibited a terminal half-life of 2.72 hours ± 1.43 hours (attempts to fit the lung ROIs to a single exponential resulted in an R^2 of 0.432). Meanwhile, the half-life (single exponential) associated with the posterior hindlimbs was 0.26 hours ± 0.11 hours ($R^2 = 0.999$). This analysis suggests that the radiance associated with both the lung and hindlimb ROIs smoothly decays, despite reinjection of furimazine. In future experiments, attention to low solubility characteristics of the furimazine and the size of crystals will be needed to ensure that injection solutions do not become entrapped in narrow vessels or vascular cannulas used for dosing.

Animals were observed for 48 hours following dosing and displayed normal behaviors. Because innate immune responses typically occur minutes to hours following IV administration of compounds, it is unlikely that CJ crystals cause innate immune activation; however, for definitive confirmation, additional studies testing cytokine levels 12-24 hours following administration need to be done. The mice in this study were only maintained for 48 hours

following IV administration and therefore were not informative about potential adaptive immune responses; this will be included in future studies as well.

Ex vivo luminescence imaging, following euthanasia and dissection of tissues, provided a quantitative end-point measure of total NanoLuc emission across specific organs (Figure 5.5). The absence of significant differences under no-furimazine conditions confirmed that background signal remained uniform across tissues, consistent with low endogenous photon emission (Figure 5.5B).[231] After furimazine addition, the transient appearance of statistical significance among organs was traced to a single outlier exhibiting unusually high muscle-associated luminescence (mouse 4 skeletal muscle). Excluding this outlier eliminated the effect, indicating that the overall distribution of luminescence among organs was statistically uniform. This outcome suggests that under the tested conditions, substrate availability rather than tissue-specific accumulation governs signal intensity. The extreme outlier may reflect localized substrate pooling,[231] incomplete clearance, or microcrystal aggregation within muscle vasculature. Notably, similar substrate-dependent artifacts have been reported in other luciferase-based biodistribution studies.[231]

Omission of the extreme outlier resulted in a loss of statistical significance between organ types, although the combined evidence from *ex vivo* analyses and live-animal IVIS imaging indicates a non-uniform biodistribution pattern characterized by persistent luminescence in the hindlimbs. The apparent concentration of signal in these regions, even after systemic circulation and clearance from major organs, suggests that CJ microcrystals may become physically entrapped within the microvasculature of skeletal muscle. The diameter of capillaries in mouse skeletal tissue ranges from approximately 3 to 10 μm,[232,233] overlapping with the larger size fraction of the microcrystal preparations, which often exceed 2 μm. This geometric constraint

provides a plausible mechanism for the observed localization; individual crystals or small aggregates may lodge transiently within narrow capillary beds, where perfusion pressures are lower and flow is less pulsatile. Such entrapment would yield a stable, localized bioluminescent signal following substrate administration, consistent with the stationary foci observed in the hindlegs of injected mice.

From a pharmacological standpoint, this behavior has both potential drawbacks and opportunities. On the one hand, vascular entrapment may pose a safety concern if prolonged occlusion were to compromise local perfusion or induce inflammatory responses. On the other hand, controlled microvascular retention represents a potential mechanism for creating a self-limiting depot system. In such a configuration, microcrystals could serve as localized reservoirs for therapeutic payloads, slowly releasing encapsulated agents as the crystal lattice dissolves or undergoes proteolytic degradation. Depot-type delivery is a cornerstone of several long-acting drug formulations—most notably in peptide[234,235] and antibody[236] therapeutics—where sustained release from a fixed anatomical site provides extended pharmacodynamic coverage while minimizing systemic exposure. The structural rigidity and chemical stability of cross-linked CJ crystals may allow similar applications, particularly for delivering macromolecules that benefit from prolonged tissue residence times. Furthermore, size-dependent immobilization of CJ microcrystals could be harnessed intentionally to achieve targeted deposition within specific vascular regions. By tuning crystal size distribution, porosity, and surface charge, it may be possible to balance systemic circulation with site-specific retention, effectively coupling passive mechanical filtration with the intrinsic biocompatibility of a protein-based carrier. Such control could enable long-acting release in muscle or subcutaneous tissue, akin to the “depot effect” achieved with aluminum-based vaccine adjuvants[237,238] or biodegradable microspheres[239]. In the

context of regenerative medicine, immobilized microcrystals could also serve as localized scaffolds for sustained paracrine signaling, wherein gradual release of cytokines, enzymes, or genetic cargo promotes local tissue remodeling. Future studies will investigate the kinetics of crystal clearance from muscle tissue, further assessment of possible immune responses, and explore additional biocompatibility strategies—such as surface PEGylation[240] or size refinement[241,242]—to tune residence time and minimize unintended vascular occlusion.

CHAPTER 6: Conclusions and Future Directions

This dissertation has described porous CJ microcrystals as structurally precise, modular biomaterials for molecular delivery, selective capture, and therapeutic scaffolding. Chapter 1 reviewed large-pore protein crystals as an emerging class of biomaterials, and identified current knowledge gaps regarding their practical use in biomedical contexts. Chapter 2 established that CJ microcrystals can function as host scaffolds for nucleic acids by demonstrating cargo uptake, conditional release using high ATP concentrations, and partial pore-level protection using a hexamer protein cap. Chapter 3 demonstrated that the platform can be extended beyond passive guest loading by engineering SpyCrystals for selective capture of virions and virus-sized particles, including SARS-CoV-2 from wastewater. Chapter 4 evaluated the compatibility of CJ crystals in an organotypic *ex vivo* setting, demonstrating that unloaded crystals do not measurably disrupt lung slice health while guest-loaded crystals can release biologically active molecules. Chapter 5 then investigated the *in vivo* fate of CJ microcrystals through bioluminescent trace labeling, providing initial evidence regarding biodistribution, tissue exposure, and microvascular retention following systemic administration. Collectively, these chapters address key gaps in the understanding of porous protein microcrystals as biomedical materials, and establish a foundation for their continued development as programmable biofunctional scaffolds.

Several important future directions follow from this work. First, further study is needed to define how crystal size, pore accessibility, cross-linking density, and guest chemistry govern transport, loading, and release, since particle geometry and surface properties

strongly influence biological delivery behavior.[243] Second, the SpyCrystal strategy could be extended to alternative binders, enzymes, and sensing modules, particularly as SpyTag/SpyCatcher-based conjugation continues to expand as a general platform for modular covalent assembly.[244] Third, additional testing in tissue-relevant systems remains important, and precision-cut lung slices are increasingly recognized as a translational model for studying integrated tissue responses and refining preclinical evaluation workflows.[245] Finally, recent advances in the computational design of highly porous, stable protein crystals suggest that future generations of crystalline biomaterials may be engineered with even greater control over pore structure, lattice symmetry, and encoded function.[246]

Due to the inherent structural and functional diversity of proteins, the number of possible lattice structures and functionality is limited only by human imagination. The past year alone has seen extremely rapid advances in machine learning-based methods,[247–249] and it is increasingly possible to identify sequences that conform to any desired tertiary structure. In 2023, the Baker group reported designed 3D protein crystals capable of rapid in vitro self-assembly.[246] Additional machine learning tools, such as AlphaFold, have been used to predict allosteric and protein–ligand interactions,[250] and may be used to alter the structure and binding affinities of LPCs. With the advent of reliable protein crystal design, we anticipate rapid growth in the number of engineered crystals with functional applications. Large pore protein crystals such as CJ represent a novel frontier for catalysis, therapeutic delivery, and a host of unexplored applications.

Appendix I: Supplemental Figures for Chapter 2

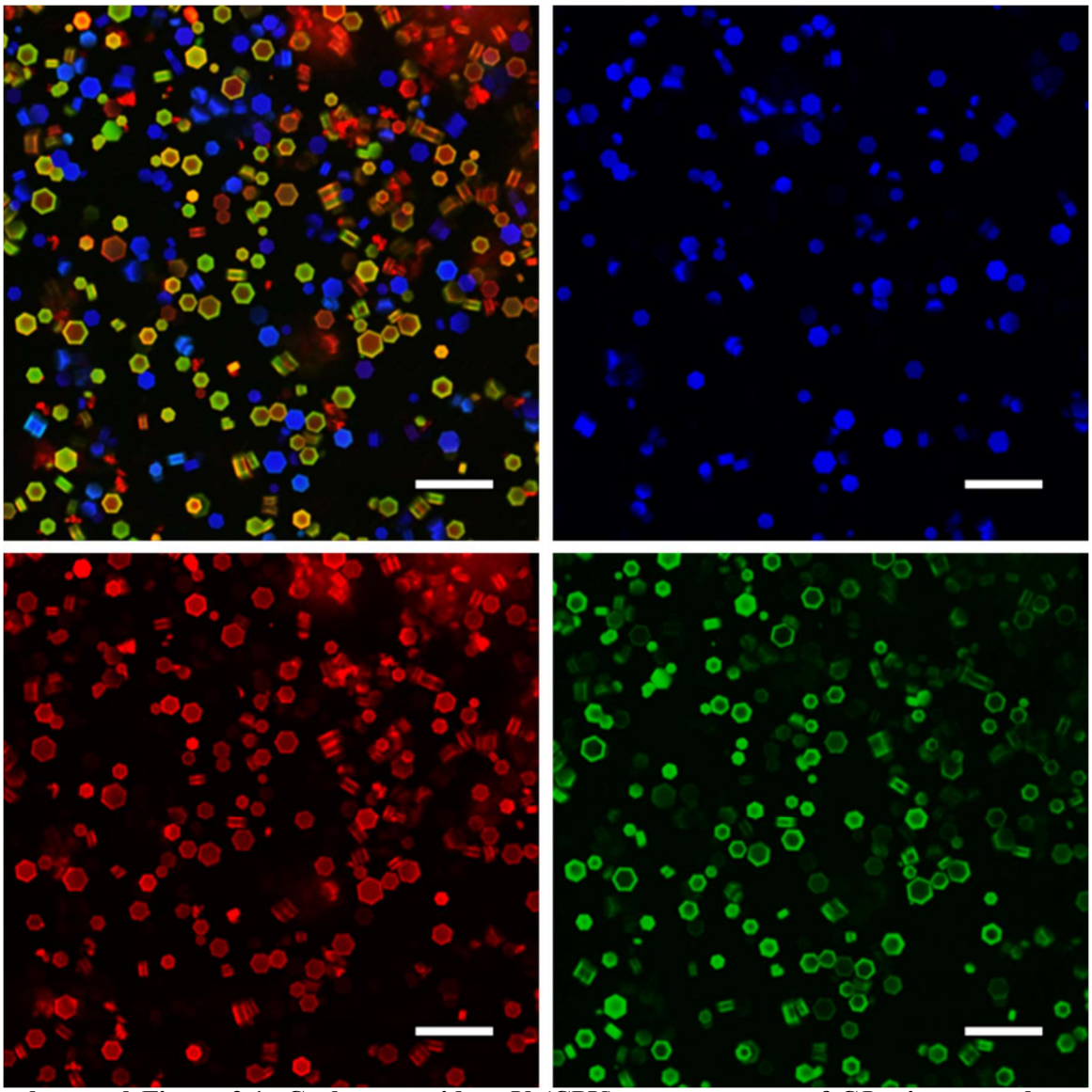

Supplemental Figure 2.1: Carboxypeptidase Y (CPY) pre-treatment of CJ microcrystals enables increased guest ssDNA loading capacity. CJ microcrystals were separately labeled with Texas Red-NHS ester (red channel) or Pacific Blue-NHS ester (blue channel). After labeling, the Texas Red-labeled crystals were soaked in CPY (1 U mL^{-1}) overnight, before washing three times with 1X PBS, pH 7.5. The labeled and un-labeled crystals were then imaged side-by-side after loading of a fluorescein-labeled, 36-nt ssDNA (green channel). Merged channels are in top left panel. Scale bar = 100 µm.

Appendix II: Supplemental Figures for Chapter 5

Supplemental Table 5.1. Pertinent Protein Sequences

CJ	MKEYTLDKAHTDVGFKIKHLQISNVK GNFKDYSAVIDFDPASAEFKKLDVTIKI ASVNTENQTRDNHLQQDDFFKAKKYP DMTFTMKKYEKIDNEKGKMTGTLTIA GVSKDIVLDAEIGGVAKGKDGKEKIGF SLNGKIKRSDFKFATSTSTITLSDDINLN IEVKANEKEGGSHHHHHH
CJ-SpyTag003	MKEYTLDKAHTDVGFKIKHLQISNVK GNFKDYSAVIDFDPASAEFKKLDVTIKI ASVNTENQTRDNHLQQDDFFKAKKYP DMTFTMKKYEKIDNEKGKMTGTLTIA GVSKDIVLDAEIGGVAKGKDGKEKIGF SLNGKIKRSDFKFATSTSTITLSDDINLN IEVKANEKEGGSHHHHHHGS**RGVPHI VMVDAYKRYK**
SpyCatcher003-sfGFP	MSYYHHHHHHDYDIPTTENLYFQGAM VTTLSGLSGEQGPSGDMTTEEDSATHI KFSKRDEDGRELAGATMELRDSSGKTI STWISDGHVKDFYLYPGKYTFVETAAP DGYEVATPIEFTVNEDGQVTVDGEATE GDAHTGSSGSRKGEELFTGVVPILVEL DGDVNGHKFSVRGEGEGDATNGKLTL KFICTTGKLPVPWPTLVTTLTYGVQCF ARYPDHMKQHDFFKSAMPEGYVQERT ISFKDDGTYKTRAEVKFEGDTLVNRIEL KGIDFKEDGNILGHKLEYNFNSHNVYI TADKQKNGIKANFKIRHNVEDGSVQL ADHYQQNTPIGDGPVLLPDNHYLSTQS VLSKDPNEKRDHMVLLEFVTAAGITHG MDELYK
SpyCatcher003-Nanoluciferase	MSYYHHHHHHDYDIPTTENLYFQGAM VTTLSGLSGEQGPSGDMTTEEDSATHI KFSKRDEDGRELAGATMELRDSSGKTI STWISDGHVKDFYLYPGKYTFVETAAP DGYEVATPIEFTVNEDGQVTVDGEATE GDAHTGSSGSMVFTLEDFVGDWRQTA GYNLDQVLEQGGVSSLFQNLGVSVTPI

	QRIVLSGENGLKIDIHVIIPYEGLSGDQ MGQIEKIFKVVYPVDDHHFKVILHYGT LVIDGVTPNMIDYFGRPYEGIAVFDGK KITVTGTLWNGNKIIDERLINPDGSLLF RVTINGVTGWRLCERILALE

Key: Blue shading = NanoLuc. Green shading = sfGFP. Gray shading = core structured region of SpyCatcher003 (per PDB entry 9OJ3). Underlined = TEV protease cleavage site. Orange font = Hexahistag. Bold = SpyTag003.

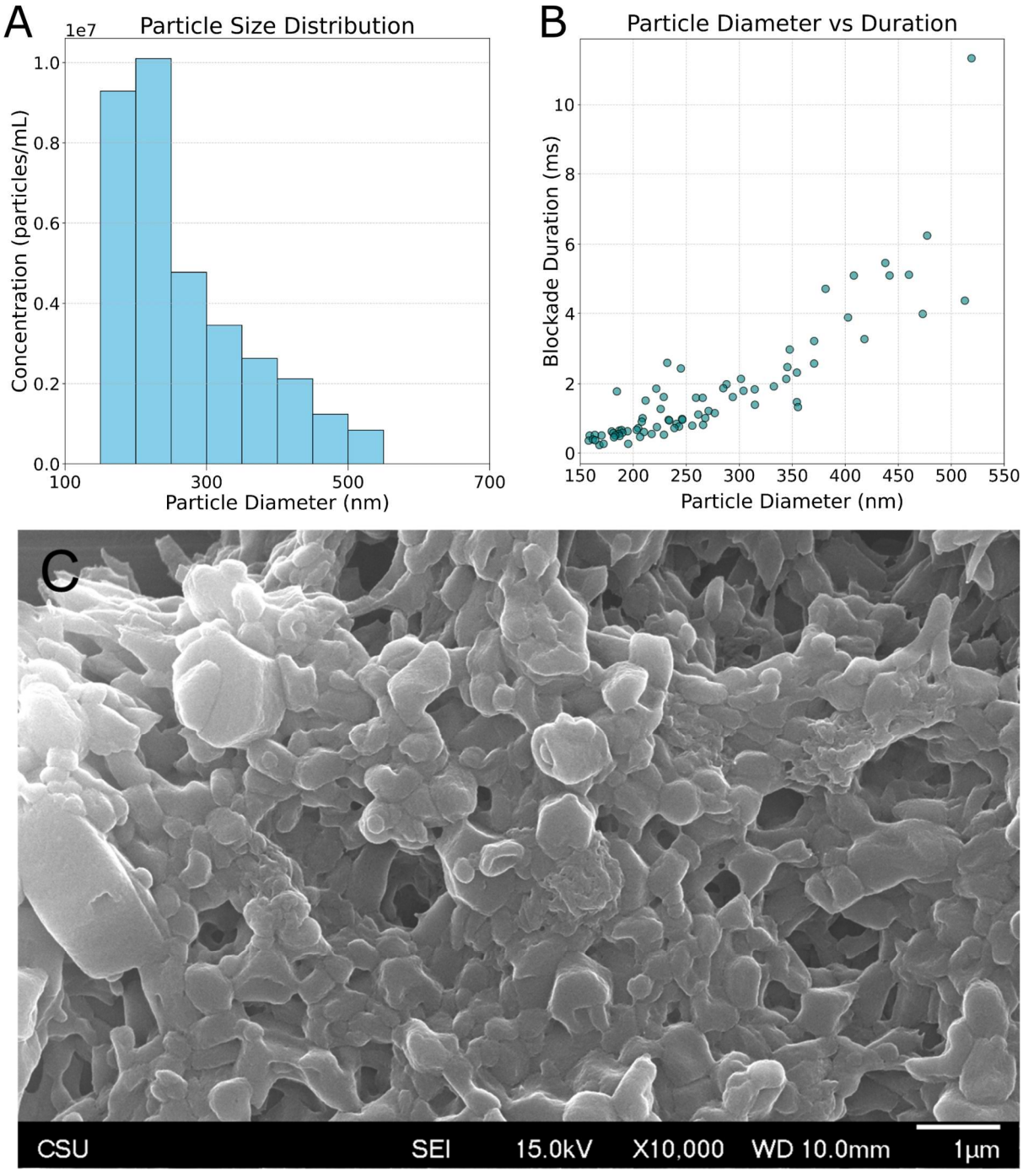

Supplemental Figure 5.1: A, Size distribution of CJ SpyCrystals, as determined via tunable-resistive pulse sensing (TRPS). **B,** Blockade duration as a function of particle diameter, as determined via TRPS. **C,** Scanning electron micrograph of wild-type CJ microcrystals of the same size as CJ SpyCrystals used in this study.

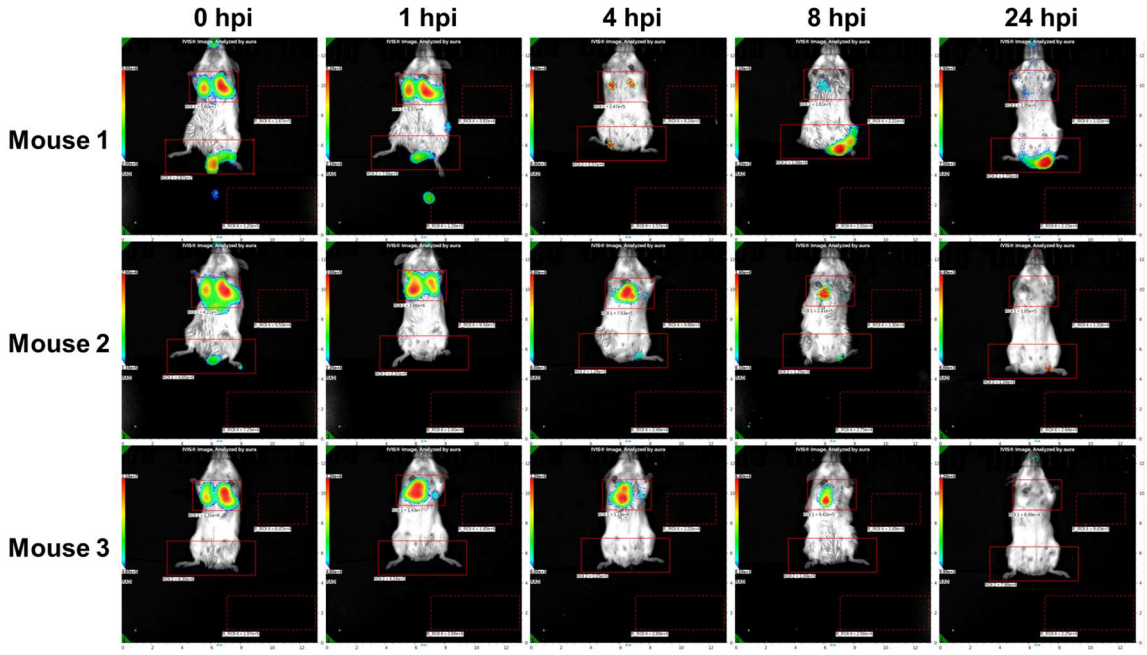

Supplemental Figure 5.2: *In vivo* radiance for mice 1-3 at 0, 1, 4, 8, and 24 hpi. Showing annotated regions of interest.

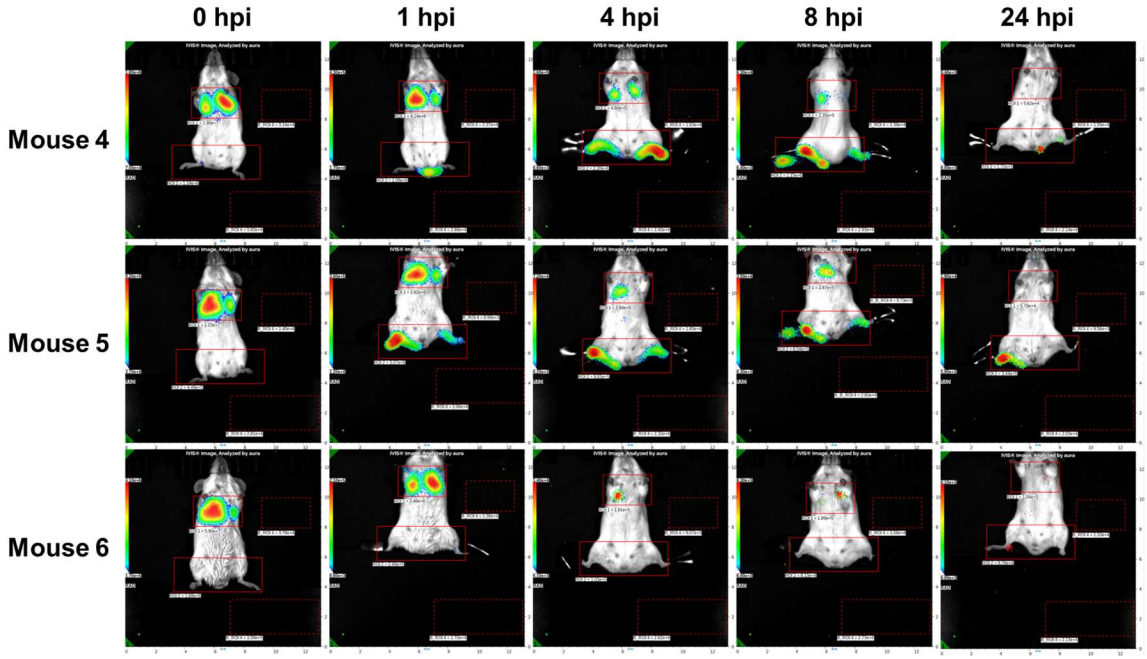

Supplemental Figure 5.3: *In vivo* radiance for mice 4-6 at 0, 1, 4, 8, and 24 hpi. Showing annotated regions of interest.

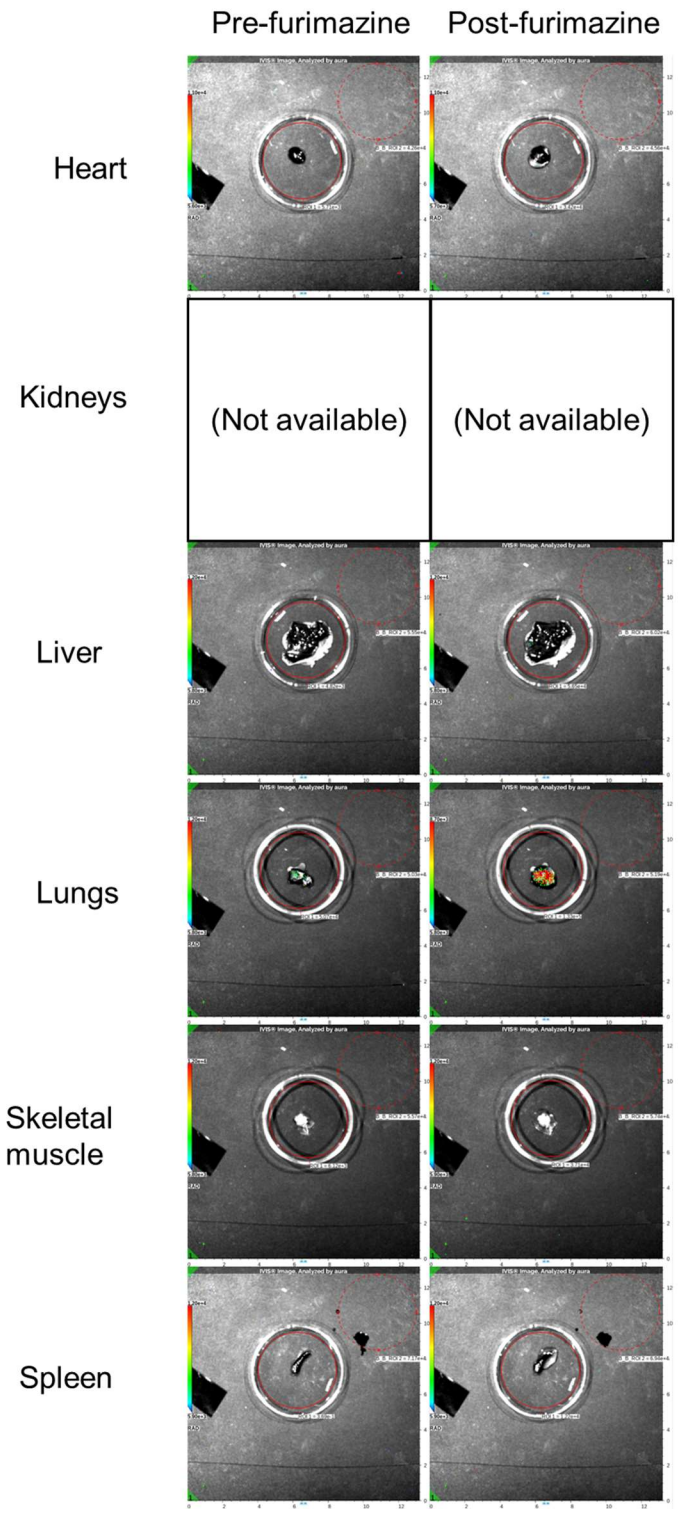

Supplemental Figure 5.4: *Ex vivo* images of individual organs from mouse 1 (before and after addition of furimazine). Showing annotated regions of interest.

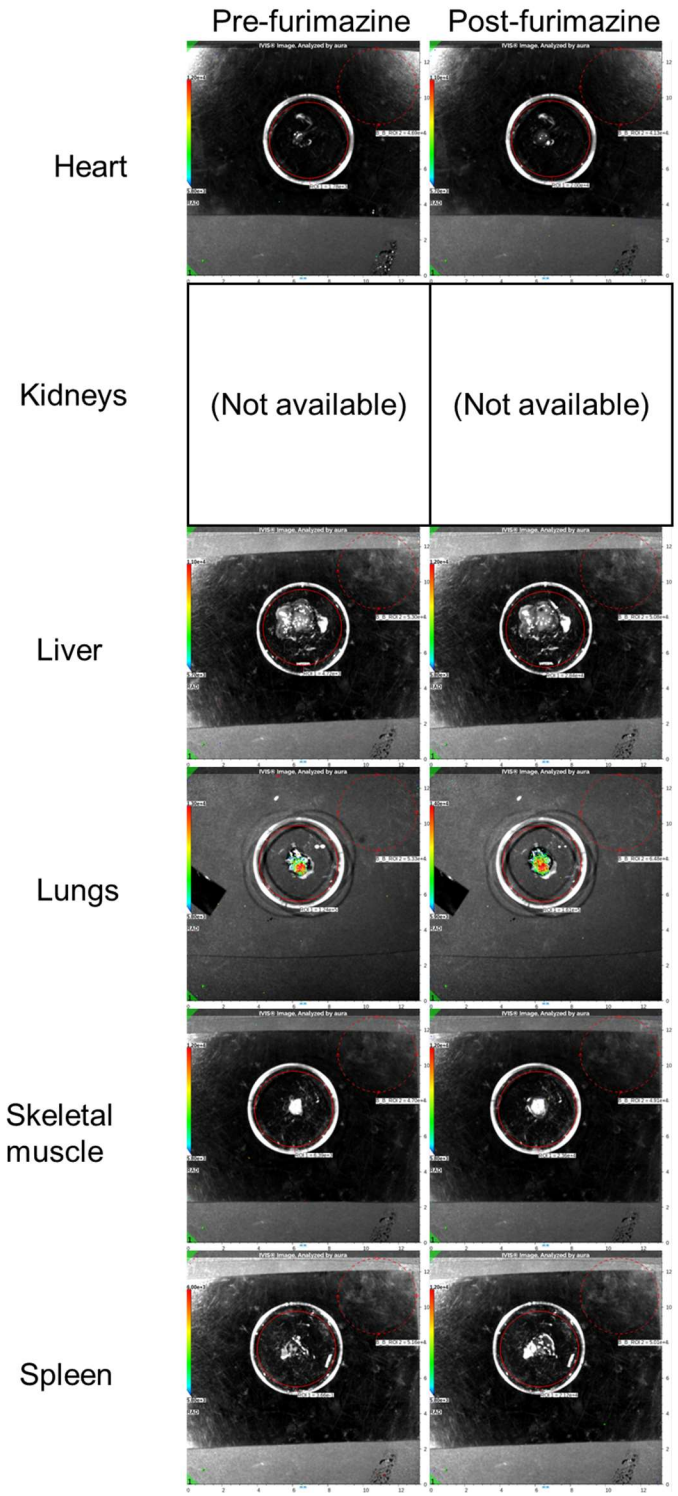

Supplemental Figure 5.5: *Ex vivo* images of individual organs from mouse 2 (before and after addition of furimazine). Showing annotated regions of interest.

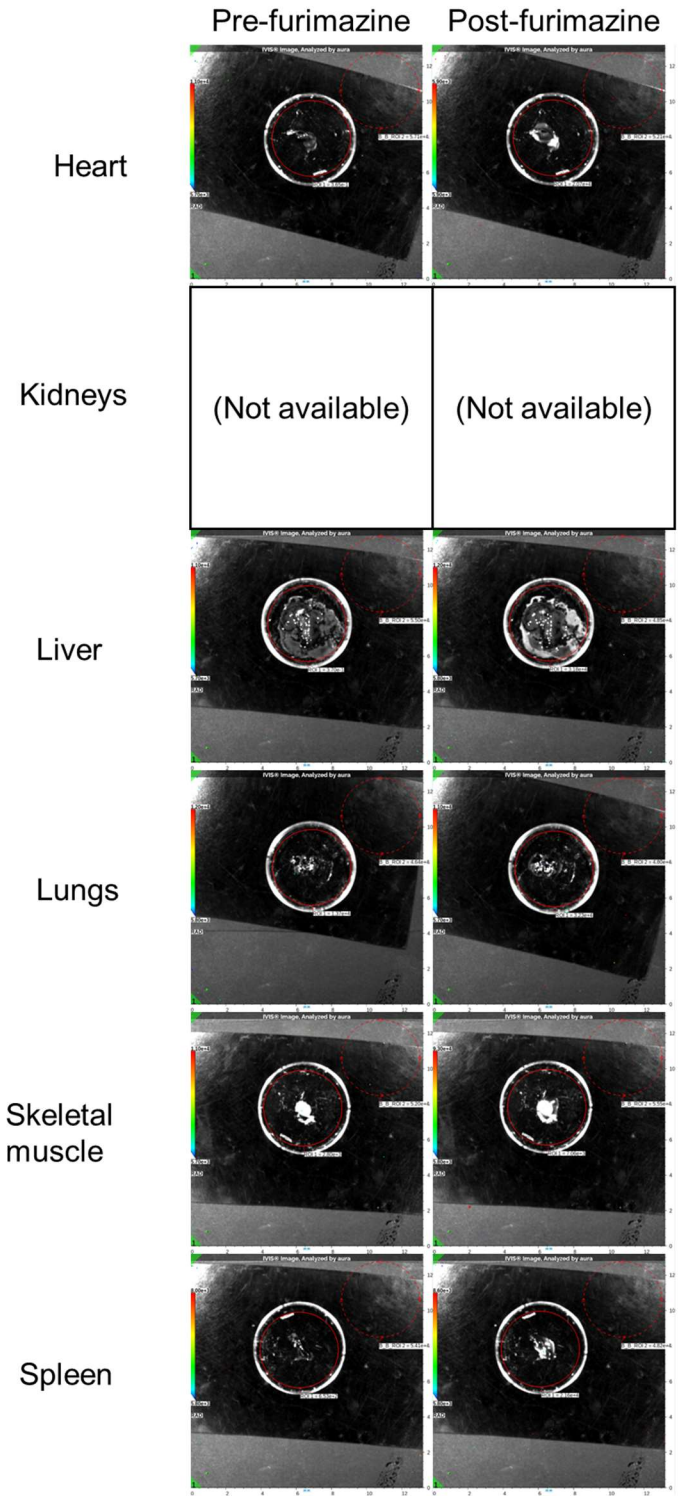

Supplemental Figure 5.6: *Ex vivo* images of individual organs from mouse 3 (before and after addition of furimazine). Showing annotated regions of interest.

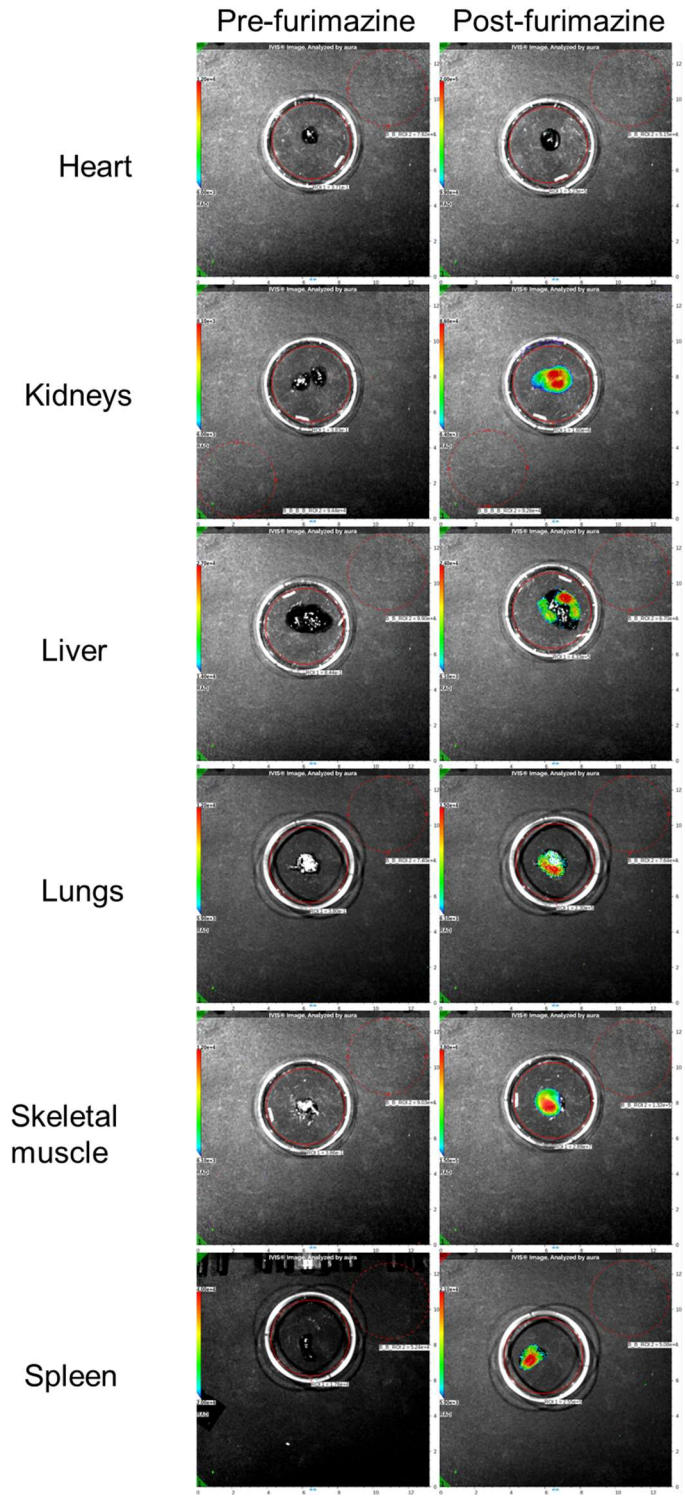

Supplemental Figure 5.7: *Ex vivo* images of individual organs from mouse 4 (before and after addition of furimazine). Showing annotated regions of interest.

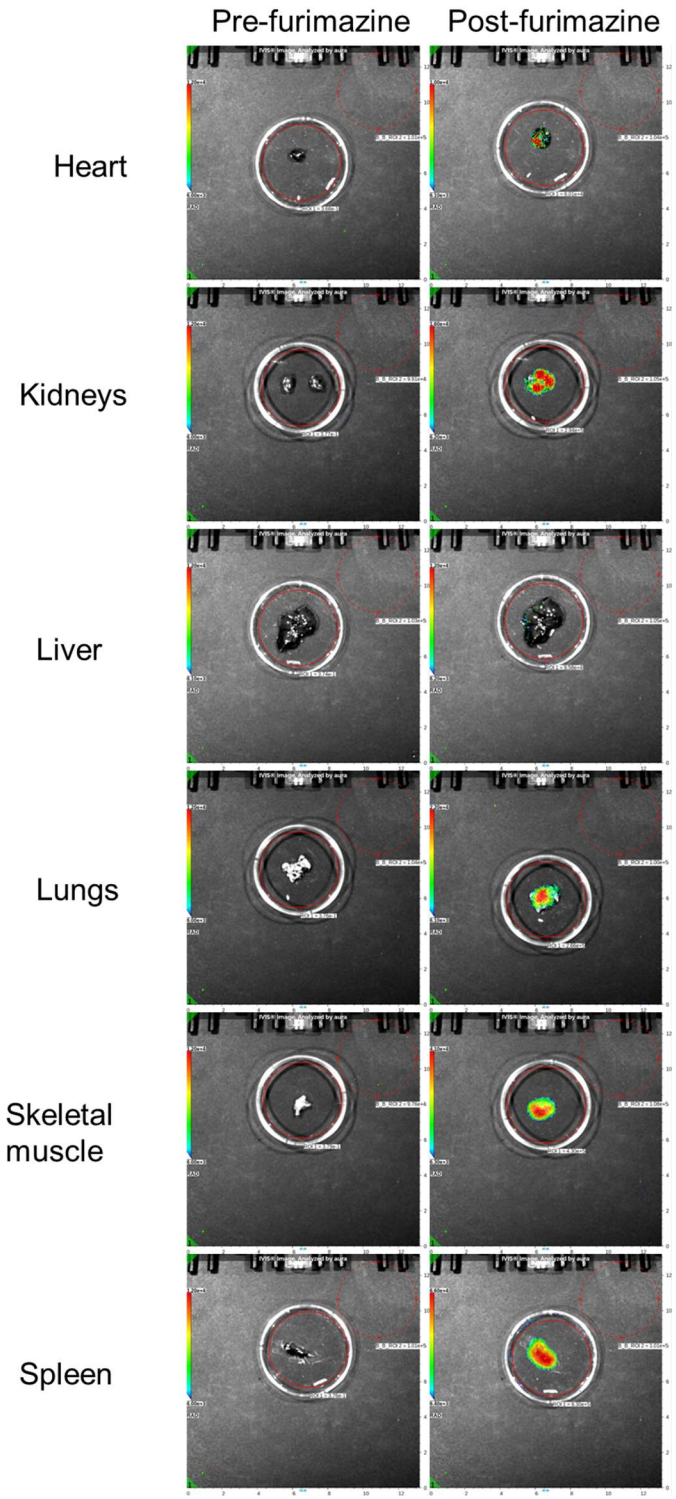

Supplemental Figure 5.8: *Ex vivo* images of individual organs from mouse 5 (before and after addition of furimazine). Showing annotated regions of interest.

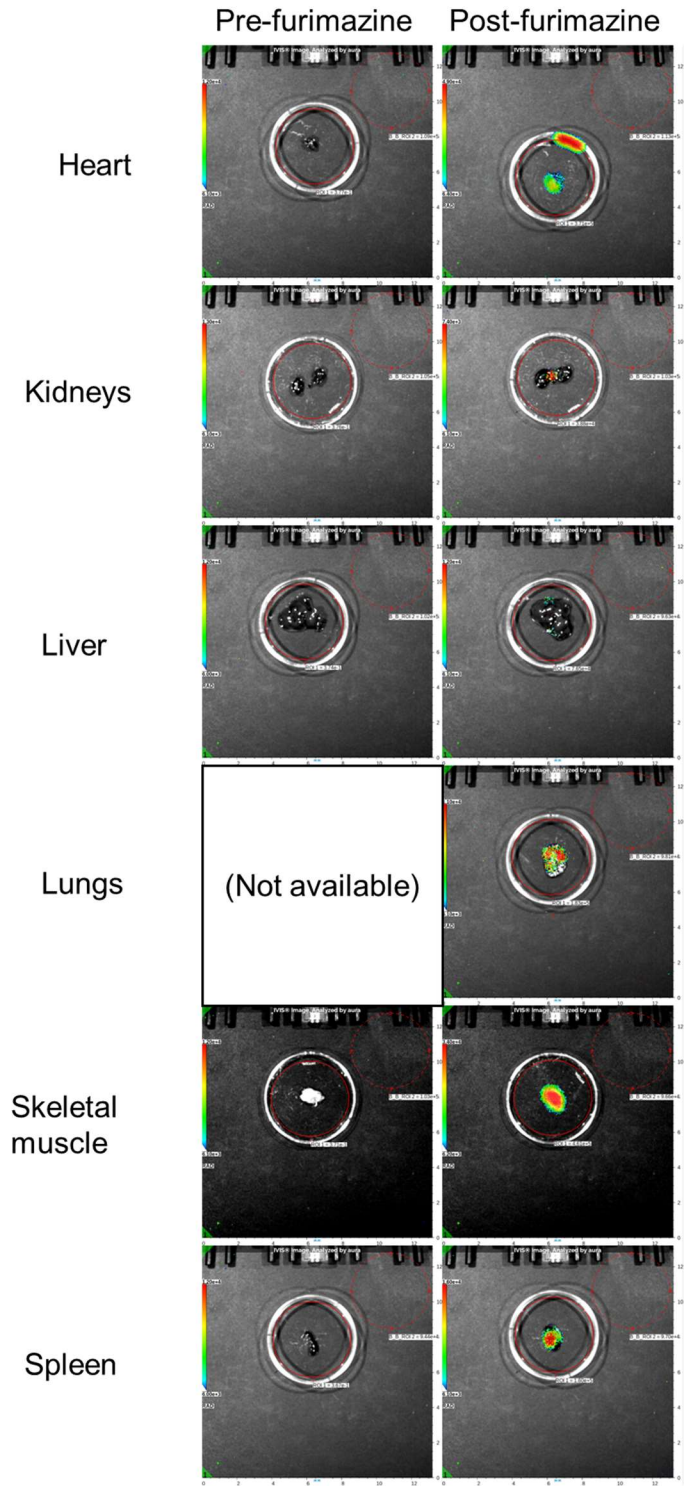

Supplemental Figure 5.9: *Ex vivo* images of individual organs from mouse 6 (before and after addition of furimazine). Showing annotated regions of interest.

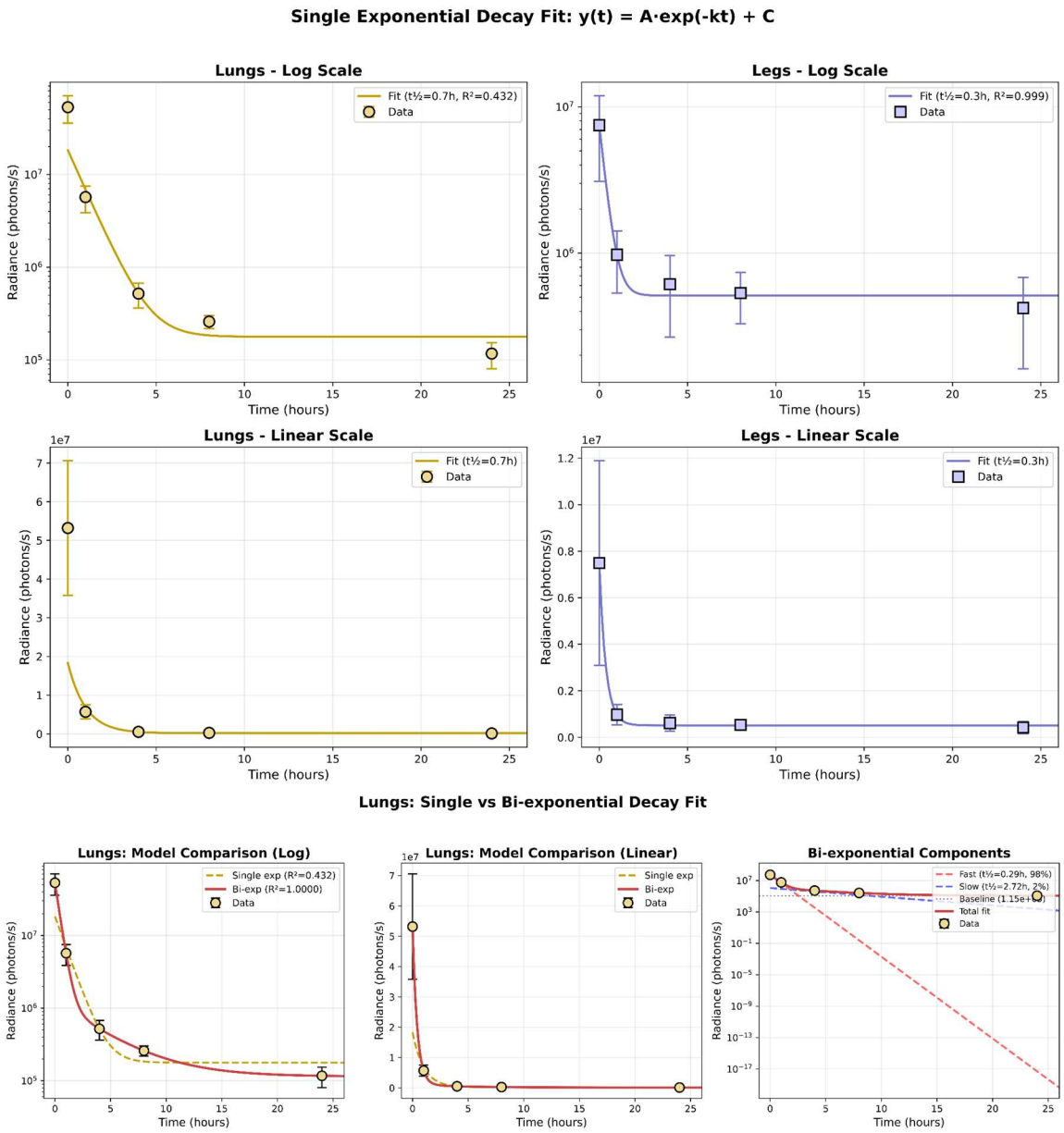

Supplemental Figure 5.10. Quantitative fitting of the *in vivo* luminescence decay data in main text Figure 5.4 revealed that a single exponential fit was suitable ($R^2 = 0.999$) to explain the luminescence decay in the legs with a half-life of 0.26 ±0.16 hr. However, the single exponential fit for the lungs was inferior ($R^2 = 0.432$). A bi-exponential fit for 5 data points is trivially perfect ($R^2 = 1.0$) with 0 degrees of freedom. The bi-exponential fit has 97.9% of the amplitude decaying with a half-life of 0.29 ±0.06 hr, and a small slow phase (2.1% of the amplitude) with a half-life of 2.72 ±1.43 hr. This latter component's amplitude is very small, but does exceed the measurement error at t=4 hr. To confidently assess the slow phase more data would be required. However, the dominant observed fast decay for both regions was quite close, possibly reflecting shared systemic clearance. Theoretically, the apparent higher long-time baseline for the hindlimbs might arise from a small population with a very long half-life. The raw data and the exponential fitting Python script can be found here: https://github.com/cdsnow/AAJ_IVIS_fitting

BIBLIOGRAPHY

(1) Stie, M. B.; Kalouta, K.; Vetri, V.; Foderà, V. Protein Materials as Sustainable Non- and Minimally Invasive Strategies for Biomedical Applications. *Journal of Controlled Release* **2022**, *344*, 12–25. https://doi.org/10.1016/j.jconrel.2022.02.016.

(2) Abascal, N. C.; Regan, L. The Past, Present and Future of Protein-Based Materials. *Open Biology* **2018**, *8* (10), 180113. https://doi.org/10.1098/rsob.180113.

(3) Zhang, B.; Chao, C. W.; Tsybovsky, Y.; Abiona, O. M.; Hutchinson, G. B.; Moliva, J. I.; Olia, A. S.; Pegu, A.; Phung, E.; Stewart-Jones, G. B. E.; Verardi, R.; Wang, L.; Wang, S.; Werner, A.; Yang, E. S.; Yap, C.; Zhou, T.; Mascola, J. R.; Sullivan, N. J.; Graham, B. S.; Corbett, K. S.; Kwong, P. D. A Platform Incorporating Trimeric Antigens into Self-Assembling Nanoparticles Reveals SARS-CoV-2-Spike Nanoparticles to Elicit Substantially Higher Neutralizing Responses than Spike Alone. *Scientific Reports* **2020**, *10* (1), 18149. https://doi.org/10.1038/s41598-020-74949-2.

(4) Tan, X.; Chen, H.; Gu, C.; Zang, J.; Zhang, T.; Wang, H.; Zhao, G. Converting Histidine-Induced 3D Protein Arrays in Crystals into Their 3D Analogues in Solution by Metal Coordination Cross-Linking. *Communications Chemistry* **2020**, *3* (1), 151. https://doi.org/10.1038/s42004-020-00394-x.

(5) Sasaki, E.; Böhringer, D.; van de Waterbeemd, M.; Leibundgut, M.; Zschoche, R.; Heck, A. J. R.; Ban, N.; Hilvert, D. Structure and Assembly of Scalable Porous Protein Cages. *Nature Communications* **2017**, *8* (1), 14663. https://doi.org/10.1038/ncomms14663.

(6) Huerta-López, C.; Alegre-Cebollada, J. Protein Hydrogels: The Swiss Army Knife for Enhanced Mechanical and Bioactive Properties of Biomaterials. *Nanomaterials* **2021**, *11* (7). https://doi.org/10.3390/nano11071656.

(7) Charrier, M.; Li, D.; Mann, V. R.; Yun, L.; Jani, S.; Rad, B.; Cohen, B. E.; Ashby, P. D.; Ryan, K. R.; Ajo-Franklin, C. M. Engineering the S-Layer of Caulobacter Crescentus as a Foundation for Stable, High-Density, 2D Living Materials. *ACS Synth Biol* **2019**, *8* (1), 181–190. https://doi.org/10.1021/acssynbio.8b00448.

(8) Tu, Y.-M.; Song, W.; Ren, T.; Shen, Y.; Chowdhury, R.; Rajapaksha, P.;4.1 Culp, T. E.; Samineni, L.; Lang, C.; Thokkadam, A.; Carson, D.; Dai, Y.; Mukthar, A.; Zhang, M.; Parshin, A.; Sloand, J. N.; Medina, S. H.; Grzelakowski, M.; Bhattacharya, D.; Phillip, W. A.; Gomez, E. D.; Hickey, R. J.; Wei, Y.; Kumar, M. Rapid Fabrication of Precise High-Throughput Filters from Membrane Protein Nanosheets. *Nat. Mater.* **2020**, *19* (3), 347–354. https://doi.org/10.1038/s41563-019-0577-z.

(9) Huber, T. R.; Hartje, L. F.; McPherson, E. C.; Kowalski, A. E.; Snow, C. D. Programmed Assembly of Host–Guest Protein Crystals. *Small* **2017**, *13* (7), 1602703. https://doi.org/10.1002/smll.201602703.

(10) Yang, Z.; Zheng, J.; Chan, C.-F.; Wong, I. L. K.; Heater, B. S.; Chow, L. M. C.; Lee, M. M. M.; Chan, M. K. Targeted Delivery of Antimicrobial Peptide by Cry Protein Crystal to Treat Intramacrophage Infection. *Biomaterials* **2019**, *217*, 119286. https://doi.org/10.1016/j.biomaterials.2019.119286.

(11) Huber, T. R.; McPherson, E. C.; Keating, C. E.; Snow, C. D. Installing Guest Molecules at Specific Sites within Scaffold Protein Crystals. *Bioconjugate Chemistry* **2018**, *29* (1), 17–22. https://doi.org/10.1021/acs.bioconjchem.7b00668.

(12) Tiessen, A.; Pérez-Rodríguez, P.; Delaye-Arredondo, L. J. Mathematical Modeling and Comparison of Protein Size Distribution in Different Plant, Animal, Fungal and Microbial Species Reveals a Negative Correlation between Protein Size and Protein Number, Thus Providing Insight into the Evolution of Proteomes. *BMC Res Notes* **2012**, *5*, 85. https://doi.org/10.1186/1756-0500-5-85.

(13) Privalov, P. L. Stability of Proteins Small Globular Proteins. In *Advances in Protein Chemistry*; Anfinsen, C. B., Edsall, J. T., Richards, F. M., Eds.; Academic Press, 1979; Vol. 33, pp 167–241. https://doi.org/10.1016/S0065-3233(08)60460-X.
(14) Sawada, Y.; Honda, S. Structural Diversity of Protein Segments Follows a Power-Law Distribution. *Biophys J* **2006**, *91* (4), 1213–1223. https://doi.org/10.1529/biophysj.105.076661.
(15) Nepomnyachiy, S.; Ben-Tal, N.; Kolodny, R. Complex Evolutionary Footprints Revealed in an Analysis of Reused Protein Segments of Diverse Lengths. *Proc Natl Acad Sci U S A* **2017**, *114* (44), 11703–11708. https://doi.org/10.1073/pnas.1707642114.
(16) Svensson, O.; Gilski, M.; Nurizzo, D.; Bowler, M. W. A Comparative Anatomy of Protein Crystals: Lessons from the Automatic Processing of 56 000 Samples. *IUCrJ* **2019**, *6* (Pt 5), 822–831. https://doi.org/10.1107/S2052252519008017.
(17) Xu, L.; Benson, S. D.; Burnett, R. M. Nanoporous Crystals of Chicken Embryo Lethal Orphan (CELO) Adenovirus Major Coat Protein, Hexon. *Journal of Structural Biology* **2007**, *157* (2), 424–431. https://doi.org/10.1016/j.jsb.2006.08.017.
(18) Ramberg, K. O.; Engilberge, S.; Skorek, T.; Crowley, P. B. Facile Fabrication of Protein–Macrocycle Frameworks. *J. Am. Chem. Soc.* **2021**, *143* (4), 1896–1907. https://doi.org/10.1021/jacs.0c10697.
(19) Lai, Y.-T.; Reading, E.; Hura, G. L.; Tsai, K.-L.; Laganowsky, A.; Asturias, F. J.; Tainer, J. A.; Robinson, C. V.; Yeates, T. O. Structure of a Designed Protein Cage That Self-Assembles into a Highly Porous Cube. *Nature Chemistry* **2014**, *6* (12), 1065–1071. https://doi.org/10.1038/nchem.2107.
(20) Li, J.; Carroll, J.; Ellar, D. J. Crystal Structure of Insecticidal δ-Endotoxin from Bacillus Thuringiensis at 2.5 Å Resolution. *Nature* **1991**, *353* (6347), 815–821. https://doi.org/10.1038/353815a0.
(21) Miller, J. L.; Coq, J. L.; Hodes, A.; Barbalat, R.; Miller, J. F.; Ghosh, P. Selective Ligand Recognition by a Diversity-Generating Retroelement Variable Protein. *PLOS Biology* **2008**, *6* (6), e131. https://doi.org/10.1371/journal.pbio.0060131.
(22) Kantardjieff, K. A.; Rupp, B. Matthews Coefficient Probabilities: Improved Estimates for Unit Cell Contents of Proteins, DNA, and Protein–Nucleic Acid Complex Crystals. *Protein Sci* **2003**, *12* (9), 1865–1871.
(23) Weichenberger, C. X.; Rupp, B. Ten Years of Probabilistic Estimates of Biocrystal Solvent Content: New Insights via Nonparametric Kernel Density Estimate. *Acta Crystallogr D Biol Crystallogr* **2014**, *70* (Pt 6), 1579–1588. https://doi.org/10.1107/S1399004714005550.
(24) McPherson, A.; Gavira, J. A. Introduction to Protein Crystallization. *Acta Crystallogr F Struct Biol Commun* **2013**, *70* (Pt 1), 2–20. https://doi.org/10.1107/S2053230X13033141.
(25) Abe, S.; Tabe, H.; Ijiri, H.; Yamashita, K.; Hirata, K.; Atsumi, K.; Shimoi, T.; Akai, M.; Mori, H.; Kitagawa, S.; Ueno, T. Crystal Engineering of Self-Assembled Porous Protein Materials in Living Cells. *ACS Nano* **2017**, *11* (3), 2410–2419. https://doi.org/10.1021/acsnano.6b06099.
(26) Ueno, T. Porous Protein Crystals as Reaction Vessels. *Chemistry – A European Journal* **2013**, *19* (28), 9096–9102. https://doi.org/10.1002/chem.201300250.
(27) Kojima, M.; Abe, S.; Ueno, T. Engineering of Protein Crystals for Use as Solid Biomaterials. *Biomater. Sci.* **2022**, *10* (2), 354–367. https://doi.org/10.1039/D1BM01752G.
(28) Tabe, H.; Takahashi, H.; Shimoi, T.; Abe, S.; Ueno, T.; Yamada, Y. Photocatalytic Hydrogen Evolution Systems Constructed in Cross-Linked Porous Protein Crystals. *Applied Catalysis B: Environmental* **2018**, *237*, 1124–1129. https://doi.org/10.1016/j.apcatb.2018.01.046.
(29) Thomas, J. M. The Birth of X-Ray Crystallography. *Nature* **2012**, *491* (7423), 186–187. https://doi.org/10.1038/491186a.
(30) Wang, D.; Stuart, J. D.; Jones, A. A.; Snow, C. D.; Kipper, M. J. Measuring Interactions of DNA with Nanoporous Protein Crystals by Atomic Force Microscopy. *Nanoscale* **2021**, *13* (24), 10871–10881. https://doi.org/10.1039/D1NR01703A.

(31) Nguyen, T. K.; Negishi, H.; Abe, S.; Ueno, T. Construction of Supramolecular Nanotubes from Protein Crystals. *Chem. Sci.* **2019**, *10* (4), 1046–1051. https://doi.org/10.1039/C8SC04167A.
(32) Boyton, I.; Goodchild, S. C.; Diaz, D.; Elbourne, A.; Collins-Praino, L. E.; Care, A. Characterizing the Dynamic Disassembly/Reassembly Mechanisms of Encapsulin Protein Nanocages. *ACS Omega* **2022**, *7* (1), 823–836. https://doi.org/10.1021/acsomega.1c05472.
(33) Falkner, J. C.; Al-Somali, A. M.; Jamison, J. A.; Zhang, J.; Adrianse, S. L.; Simpson, R. L.; Calabretta, M. K.; Radding, W.; Phillips, G. N.; Colvin, V. L. Generation of Size-Controlled, Submicrometer Protein Crystals. *Chemistry of Materials* **2005**, *17* (10), 2679–2686. https://doi.org/10.1021/cm047924w.
(34) Kowalski, A. E.; Johnson, L. B.; Dierl, H. K.; Park, S.; Huber, T. R.; Snow, C. D. Porous Protein Crystals as Scaffolds for Enzyme Immobilization. *Biomaterials Science* **2019**, *7* (5), 1898–1904. https://doi.org/10.1039/C8BM01378K.
(35) Han, K.; Zhang, Z.; Tezcan, F. A. Spatially Patterned, Porous Protein Crystals as Multifunctional Materials. *J. Am. Chem. Soc.* **2023**, *145* (36), 19932–19944. https://doi.org/10.1021/jacs.3c06348.
(36) Nair, M. S.; Lee, M. M.; Bonnegarde-Bernard, A.; Wallace, J. A.; Dean, D. H.; Ostrowski, M. C.; Burry, R. W.; Boyaka, P. N.; Chan, M. K. Cry Protein Crystals: A Novel Platform for Protein Delivery. *PLOS ONE* **2015**, *10* (6), e0127669. https://doi.org/10.1371/journal.pone.0127669.
(37) Adalat, R.; Saleem, F.; Crickmore, N.; Naz, S.; Shakoori, A. R. In Vivo Crystallization of Three-Domain Cry Toxins. *Toxins (Basel)* **2017**, *9* (3), 80. https://doi.org/10.3390/toxins9030080.
(38) Herrmann, J.; Jabbarpour, F.; Bargar, P. G.; Nomellini, J. F.; Li, P.-N.; Lane, T. J.; Weiss, T. M.; Smit, J.; Shapiro, L.; Wakatsuki, S. Environmental Calcium Controls Alternate Physical States of the Caulobacter Surface Layer. *Biophys J* **2017**, *112* (9), 1841–1851. https://doi.org/10.1016/j.bpj.2017.04.003.
(39) Comerci, C. J.; Herrmann, J.; Yoon, J.; Jabbarpour, F.; Zhou, X.; Nomellini, J. F.; Smit, J.; Shapiro, L.; Wakatsuki, S.; Moerner, W. E. Topologically-Guided Continuous Protein Crystallization Controls Bacterial Surface Layer Self-Assembly. *Nat Commun* **2019**, *10* (1), 2731. https://doi.org/10.1038/s41467-019-10650-x.
(40) Mann, V. R.; Manea, F.; Borys, N. J.; Ajo-Franklin, C. M.; Cohen, B. E. Controlled and Stable Patterning of Diverse Inorganic Nanocrystals on Crystalline Two-Dimensional Protein Arrays. *Biochemistry* **2021**, *60* (13), 1063–1074. https://doi.org/10.1021/acs.biochem.1c00032.
(41) Lu, K.; Ye, W.; Zhou, L.; Collins, L. B.; Chen, X.; Gold, A.; Ball, L. M.; Swenberg, J. A. Structural Characterization of Formaldehyde-Induced Cross-Links Between Amino Acids and Deoxynucleosides and Their Oligomers. *J. Am. Chem. Soc.* **2010**, *132* (10), 3388–3399. https://doi.org/10.1021/ja908282f.
(42) Yan, E.-K.; Cao, H.-L.; Zhang, C.-Y.; Lu, Q.-Q.; Ye, Y.-J.; He, J.; Huang, L.-J.; Yin, D.-C. Cross-Linked Protein Crystals by Glutaraldehyde and Their Applications. *RSC Advances* **2015**, *5* (33), 26163–26174. https://doi.org/10.1039/C5RA01722J.
(43) Quiocho, F. A.; Richards, F. M. Intermolecular Cross Linking of a Protein in the Crystalline State: Carboxypeptidase-A*. *Proceedings of the National Academy of Sciences* **1964**, *52* (3), 833–839. https://doi.org/10.1073/pnas.52.3.833.
(44) Hartje, L. F.; Bui, H. T.; Andales, D. A.; James, S. P.; Huber, T. R.; Snow, C. D. Characterizing the Cytocompatibility of Various Cross-Linking Chemistries for the Production of Biostable Large-Pore Protein Crystal Materials. *ACS Biomater Sci Eng* **2018**, *4* (3), 826–831. https://doi.org/10.1021/acsbiomaterials.8b00023.
(45) Orun, A. R.; Dmytriw, S.; Vajapayajula, A.; Snow, C. D. Stabilizing DNA–Protein Co-Crystals via Intra-Crystal Chemical Ligation of the DNA. *Crystals* **2022**, *12* (1), 49. https://doi.org/10.3390/cryst12010049.
(46) Zhang, Q.; Crosland, E.; Fabris, D. Nested Arg-Specific Bifunctional Crosslinkers for MS-Based Structural Analysis of Proteins and Protein Assemblies. *Anal Chim Acta* **2008**, *627* (1), 117–128. https://doi.org/10.1016/j.aca.2008.05.074.

(47) Lusty, C. J. A Gentle Vapor-Diffusion Technique for Cross-Linking of Protein Crystals for Cryocrystallography. *J Appl Cryst* **1999**, *32* (1), 106–112. https://doi.org/10.1107/S002188989801053X.
(48) Hiromoto, T.; Ikura, T.; Honjo, E.; Blaber, M.; Kuroki, R.; Tamada, T. Creation of Cross-Linked Crystals With Intermolecular Disulfide Bonds Connecting Symmetry-Related Molecules Allows Retention of Tertiary Structure in Different Solvent Conditions. *Frontiers in Molecular Biosciences* **2022**, *9*.
(49) Pu, M.; Xu, Z.; Peng, Y.; Hou, Y.; Liu, D.; Wang, Y.; Liu, H.; Song, G.; Liu, Z.-J. Protein Crystal Quality Oriented Disulfide Bond Engineering. *Protein Cell* **2018**, *9* (7), 659–663. https://doi.org/10.1007/s13238-017-0482-7.
(50) Silva, D.-A.; Stewart, L.; Lam, K.-H.; Jin, R.; Baker, D. Structures and Disulfide Cross-Linking of de Novo Designed Therapeutic Mini-Proteins. *The FEBS Journal* **2018**, *285* (10), 1783–1785. https://doi.org/10.1111/febs.14394.
(51) Fauser, J.; Savitskiy, S.; Fottner, M.; Trauschke, V.; Gulen, B. Sortase-Mediated Quantifiable Enzyme Immobilization on Magnetic Nanoparticles. *Bioconjugate Chem.* **2020**, *31* (8), 1883–1892. https://doi.org/10.1021/acs.bioconjchem.0c00322.
(52) Susmitha, A.; Arya, J. S.; Sundar, L.; Maiti, K. K.; Nampoothiri, K. M. Sortase E-Mediated Site-Specific Immobilization of Green Fluorescent Protein and Xylose Dehydrogenase on Gold Nanoparticles. *Journal of Biotechnology* **2023**, *367*, 11–19. https://doi.org/10.1016/j.jbiotec.2023.03.007.
(53) Wang, H. H.; Altun, B.; Nwe, K.; Tsourkas, A. Proximity-Based Sortase-Mediated Ligation. *Angew Chem Int Ed Engl* **2017**, *56* (19), 5349–5352. https://doi.org/10.1002/anie.201701419.
(54) Cai, L.-X.; Lin, Y.-Q.; Chu, Y.-M.; Chen, X.-P.; Liu, L.-X.; Zhang, M.; Zhang, G.-Y. A Simple Technique for Direct Immobilization of Target Enzymes from Cell Lysates Based on the SpyTag/SpyCatcher Spontaneous Reaction. *Bio Protoc* **2022**, *12* (1), e4282. https://doi.org/10.21769/BioProtoc.4282.
(55) Liu, C.; Hua, J.; Ng, P. F.; Fei, B. Photochemistry of Bioinspired Dityrosine Crosslinking. *Journal of Materials Science & Technology* **2021**, *63*, 182–191. https://doi.org/10.1016/j.jmst.2020.02.086.
(56) Lee, J.; Ju, M.; Cho, O. H.; Kim, Y.; Nam, K. T. Tyrosine-Rich Peptides as a Platform for Assembly and Material Synthesis. *Advanced Science* **2019**, *6* (4), 1801255. https://doi.org/10.1002/advs.201801255.
(57) Raven, D. J.; Earland, C.; Little, M. Occurrence of Dityrosine in Tussah Silk Fibroin and Keratin. *Biochimica et Biophysica Acta (BBA) - Protein Structure* **1971**, *251* (1), 96–99. https://doi.org/10.1016/0005-2795(71)90065-1.
(58) Müller, F.; Graziadei, A.; Rappsilber, J. Quantitative Photo-Crosslinking Mass Spectrometry Revealing Protein Structure Response to Environmental Changes. *Anal. Chem.* **2019**, *91* (14), 9041–9048. https://doi.org/10.1021/acs.analchem.9b01339.
(59) Stahl, K.; Graziadei, A.; Dau, T.; Brock, O.; Rappsilber, J. Protein Structure Prediction with In-Cell Photo-Crosslinking Mass Spectrometry and Deep Learning. *Nat Biotechnol* **2023**, 1–10. https://doi.org/10.1038/s41587-023-01704-z.
(60) Schweizer, U.; Hey, T.; Lipps, G.; Krauss, G. Photocrosslinking Locates a Binding Site for the Large Subunit of Human Replication Protein A to the Damaged Strand of Cisplatin-Modified DNA. *Nucleic Acids Research* **1999**, *27* (15), 3183–3189. https://doi.org/10.1093/nar/27.15.3183.
(61) Zhang, S.; Adamson, D. H.; Prud'homme, R. K.; Link, A. J. Photocrosslinking the Polystyrene Core of Block-Copolymer Nanoparticles. *Polym. Chem.* **2011**, *2* (3), 665–671. https://doi.org/10.1039/C0PY00350F.
(62) Luse, R. A.; McLaren, A. D. Mechanism of Enzyme Inactivation by Ultraviolet Light and the Photochemistry of Amino Acids (at 2537 Å)*. *Photochemistry and Photobiology* **1963**, *2* (3), 343–360. https://doi.org/10.1111/j.1751-1097.1963.tb08127.x.
(63) Wang, D.; Hedayati, M.; Stuart, J. D.; Madruga, L. Y. C.; Popat, K. C.; Snow, C. D.; Kipper, M. J. Ligand Presentation inside Protein Crystal Nanopores: Tunable Interfacial Adhesion Noncovalently

Modulates Cell Attachment. *Materials Today Nano* **2023**, *24*, 100432. https://doi.org/10.1016/j.mtnano.2023.100432.
(64) Willmott, G. R. Tunable Resistive Pulse Sensing: Better Size and Charge Measurements for Submicrometer Colloids. *Anal. Chem.* **2018**, *90* (5), 2987–2995. https://doi.org/10.1021/acs.analchem.7b05106.
(65) Xu, K.; Chen, X.; Zheng, R.; Zheng, Y. Immobilization of Multi-Enzymes on Support Materials for Efficient Biocatalysis. *Frontiers in Bioengineering and Biotechnology* **2020**, *8*.
(66) Nguyen, T. K.; Abe, S.; Kasamatsu, M.; Maity, B.; Yamashita, K.; Hirata, K.; Kojima, M.; Ueno, T. In-Cell Engineering of Protein Crystals with Nanoporous Structures for Promoting Cascade Reactions. *ACS Appl. Nano Mater.* **2021**, *4* (2), 1672–1681. https://doi.org/10.1021/acsanm.0c03129.
(67) Healey, R. D.; Couillaud, L.; Hoh, F.; Mouhand, A.; Fouillen, A.; Couvineau, P.; Granier, S.; Leyrat, C. Structure, Dynamics and Transferability of the Metal-Dependent Polyhistidine Tetramerization Motif TetrHis for Single-Chain Fv Antibodies. *Commun Chem* **2023**, *6* (1), 1–13. https://doi.org/10.1038/s42004-023-00962-x.
(68) Heater, B. S.; Chan, W. S.; Lee, M. M.; Chan, M. K. Directed Evolution of a Genetically Encoded Immobilized Lipase for the Efficient Production of Biodiesel from Waste Cooking Oil. *Biotechnology for Biofuels* **2019**, *12* (1), 165. https://doi.org/10.1186/s13068-019-1509-5.
(69) Gad, S.; Ayakar, S. Protein Scaffolds: A Tool for Multi-Enzyme Assembly. *Biotechnology Reports* **2021**, *32*, e00670. https://doi.org/10.1016/j.btre.2021.e00670.
(70) Sun, Q.; Heater, B. S.; Li, T. L.; Ye, W.; Guo, Z.; Chan, M. K. Cry3Aa*SpyCatcher Fusion Crystals Produced in Bacteria as Scaffolds for Multienzyme Coimmobilization. *Bioconjugate Chemistry* **2022**, *33* (2), 386–396. https://doi.org/10.1021/acs.bioconjchem.2c00003.
(71) Zakeri, B.; Fierer, J. O.; Celik, E.; Chittock, E. C.; Schwarz-Linek, U.; Moy, V. T.; Howarth, M. Peptide Tag Forming a Rapid Covalent Bond to a Protein, through Engineering a Bacterial Adhesin. *Proceedings of the National Academy of Sciences* **2012**, *109* (12), E690–E697. https://doi.org/10.1073/pnas.1115485109.
(72) Keeble, A. H.; Turkki, P.; Stokes, S.; Khairil Anuar, I. N. A.; Rahikainen, R.; Hytönen, V. P.; Howarth, M. Approaching Infinite Affinity through Engineering of Peptide–Protein Interaction. *Proceedings of the National Academy of Sciences* **2019**, *116* (52), 26523–26533. https://doi.org/10.1073/pnas.1909653116.
(73) Tian, J.; Jia, R.; Wenge, D.; Sun, H.; Wang, Y.; Chang, Y.; Luo, H. One-Step Purification and Immobilization of Recombinant Proteins Using SpyTag/SpyCatcher Chemistry. *Biotechnol Lett* **2021**, *43* (5), 1075–1087. https://doi.org/10.1007/s10529-021-03098-x.
(74) Anderson, G. P.; Liu, J. L.; Shriver-Lake, L. C.; Zabetakis, D.; Sugiharto, V. A.; Chen, H.-W.; Lee, C.-R.; Defang, G. N.; Wu, S.-J. L.; Venkateswaran, N.; Goldman, E. R. Oriented Immobilization of Single-Domain Antibodies Using SpyTag/SpyCatcher Yields Improved Limits of Detection. *Anal. Chem.* **2019**, *91* (15), 9424–9429. https://doi.org/10.1021/acs.analchem.9b02096.
(75) Liu, M.; Song, Y.; Zhang, Y.-H. P. J.; You, C. Carrier-Free Immobilization of Multi-Enzyme Complex Facilitates In Vitro Synthetic Enzymatic Biosystem for Biomanufacturing. *ChemSusChem* **2023**, *16* (6), e202202153. https://doi.org/10.1002/cssc.202202153.
(76) Khairil Anuar, I. N. A.; Banerjee, A.; Keeble, A. H.; Carella, A.; Nikov, G. I.; Howarth, M. Spy&Go Purification of SpyTag-Proteins Using Pseudo-SpyCatcher to Access an Oligomerization Toolbox. *Nat Commun* **2019**, *10* (1), 1734. https://doi.org/10.1038/s41467-019-09678-w.
(77) Schoene, C.; Fierer, J. O.; Bennett, S. P.; Howarth, M. SpyTag/SpyCatcher Cyclization Confers Resilience to Boiling on a Mesophilic Enzyme. *Angew Chem Int Ed Engl* **2014**, *53* (24), 6101–6104. https://doi.org/10.1002/anie.201402519.
(78) Zhang, S.; Ren, Q.; Novick, S. J.; Strutzenberg, T. S.; Griffin, P. R.; Bao, H. One-Step Construction of Circularized Nanodiscs Using SpyCatcher-SpyTag. *Nat Commun* **2021**, *12* (1), 5451. https://doi.org/10.1038/s41467-021-25737-7.

(79) Guo, S.; Huang, Y.; Jiang, Q.; Sun, Y.; Deng, L.; Liang, Z.; Du, Q.; Xing, J.; Zhao, Y.; Wang, P. C.; Dong, A.; Liang, X.-J. Enhanced Gene Delivery and siRNA Silencing by Gold Nanoparticles Coated with Charge-Reversal Polyelectrolyte. *ACS Nano* **2010**, *4* (9), 5505–5511. https://doi.org/10.1021/nn101638u.

(80) Guo, J.; Armstrong, M. J.; O'Driscoll, C. M.; Holmes, J. D.; Rahme, K. Positively Charged, Surfactant-Free Gold Nanoparticles for Nucleic Acid Delivery. *RSC Adv.* **2015**, *5* (23), 17862–17871. https://doi.org/10.1039/C4RA16294C.

(81) Ruks, T.; Loza, K.; Heggen, M.; Ottmann, C.; Bayer, P.; Beuck, C.; Epple, M. Targeting the Surface of the Protein 14-3-3 by Ultrasmall (1.5 Nm) Gold Nanoparticles Carrying the Specific Peptide CRaf. *ChemBioChem* **2021**, *22* (8), 1456–1463. https://doi.org/10.1002/cbic.202000761.

(82) Bharti, C.; Nagaich, U.; Pal, A. K.; Gulati, N. Mesoporous Silica Nanoparticles in Target Drug Delivery System: A Review. *Int J Pharm Investig* **2015**, *5* (3), 124–133. https://doi.org/10.4103/2230-973X.160844.

(83) Rizzi, F.; Castaldo, R.; Latronico, T.; Lasala, P.; Gentile, G.; Lavorgna, M.; Striccoli, M.; Agostiano, A.; Comparelli, R.; Depalo, N.; Curri, M. L.; Fanizza, E. High Surface Area Mesoporous Silica Nanoparticles with Tunable Size in the Sub-Micrometer Regime: Insights on the Size and Porosity Control Mechanisms. *Molecules* **2021**, *26* (14). https://doi.org/10.3390/molecules26144247.

(84) Vallet-Regí, M.; Schüth, F.; Lozano, D.; Colilla, M.; Manzano, M. Engineering Mesoporous Silica Nanoparticles for Drug Delivery: Where Are We after Two Decades? *Chem. Soc. Rev.* **2022**, *51* (13), 5365–5451. https://doi.org/10.1039/D1CS00659B.

(85) Elsana, H.; Olusanya, T. O. B.; Carr-wilkinson, J.; Darby, S.; Faheem, A.; Elkordy, A. A. Evaluation of Novel Cationic Gene Based Liposomes with Cyclodextrin Prepared by Thin Film Hydration and Microfluidic Systems. *Sci Rep* **2019**, *9* (1), 15120. https://doi.org/10.1038/s41598-019-51065-4.

(86) Obeid, M. A.; Elburi, A.; Young, L. C.; Mullen, A. B.; Tate, R. J.; Ferro, V. A. Formulation of Nonionic Surfactant Vesicles (NISV) Prepared by Microfluidics for Therapeutic Delivery of siRNA into Cancer Cells. *Mol. Pharmaceutics* **2017**, *14* (7), 2450–2458. https://doi.org/10.1021/acs.molpharmaceut.7b00352.

(87) Lee, B. R.; Oh, K. T.; Baik, H. J.; Youn, Y. S.; Lee, E. S. A Charge-Switched Nano-Sized Polymeric Carrier for Protein Delivery. *Int J Pharm* **2010**, *392* (1–2), 78–82. https://doi.org/10.1016/j.ijpharm.2010.03.028.

(88) Ninan, N.; Forget, A.; Shastri, V. P.; Voelcker, N. H.; Blencowe, A. Antibacterial and Anti-Inflammatory pH-Responsive Tannic Acid-Carboxylated Agarose Composite Hydrogels for Wound Healing. *ACS Appl Mater Interfaces* **2016**, *8* (42), 28511–28521. https://doi.org/10.1021/acsami.6b10491.

(89) Cooley, M.; Sarode, A.; Hoore, M.; Fedosov, D. A.; Mitragotri, S.; Gupta, A. S. Influence of Particle Size and Shape on Their Margination and Wall-Adhesion: Implications in Drug Delivery Vehicle Design across Nano-to-Micro Scale. *Nanoscale* **2018**, *10* (32), 15350–15364. https://doi.org/10.1039/c8nr04042g.

(90) Decuzzi, P.; Godin, B.; Tanaka, T.; Lee, S. Y.; Chiappini, C.; Liu, X.; Ferrari, M. Size and Shape Effects in the Biodistribution of Intravascularly Injected Particles. *Journal of Controlled Release* **2010**, *141* (3), 320–327. https://doi.org/10.1016/j.jconrel.2009.10.014.

(91) Yang, Z.; Lee, M. M. M.; Chan, M. K. Efficient Intracellular Delivery of P53 Protein by Engineered Protein Crystals Restores Tumor Suppressing Function in Vivo. *Biomaterials* **2021**, *271*, 120759. https://doi.org/10.1016/j.biomaterials.2021.120759.

(92) Nakase, I.; Noguchi, K.; Aoki, A.; Takatani-Nakase, T.; Fujii, I.; Futaki, S. Arginine-Rich Cell-Penetrating Peptide-Modified Extracellular Vesicles for Active Macropinocytosis Induction and Efficient Intracellular Delivery. *Sci Rep* **2017**, *7*, 1991. https://doi.org/10.1038/s41598-017-02014-6.

(93) Silva, S.; Almeida, A. J.; Vale, N. Combination of Cell-Penetrating Peptides with Nanoparticles for Therapeutic Application: A Review. *Biomolecules* **2019**, *9* (1), 22. https://doi.org/10.3390/biom9010022.

(94) Degors, I. M. S.; Wang, C.; Rehman, Z. U.; Zuhorn, I. S. Carriers Break Barriers in Drug Delivery: Endocytosis and Endosomal Escape of Gene Delivery Vectors. *Acc Chem Res* **2019**, *52* (7), 1750–1760. https://doi.org/10.1021/acs.accounts.9b00177.
(95) Sun, Z.; Huang, J.; Fishelson, Z.; Wang, C.; Zhang, S. Cell-Penetrating Peptide-Based Delivery of Macromolecular Drugs: Development, Strategies, and Progress. *Biomedicines* **2023**, *11* (7), 1971. https://doi.org/10.3390/biomedicines11071971.
(96) McNaughton, B. R.; Cronican, J. J.; Thompson, D. B.; Liu, D. R. Mammalian Cell Penetration, siRNA Transfection, and DNA Transfection by Supercharged Proteins. *Proceedings of the National Academy of Sciences* **2009**, *106* (15), 6111–6116. https://doi.org/10.1073/pnas.0807883106.
(97) Yin, J.; Wang, Q.; Hou, S.; Bao, L.; Yao, W.; Gao, X. Potent Protein Delivery into Mammalian Cells via a Supercharged Polypeptide. *J. Am. Chem. Soc.* **2018**, *140* (49), 17234–17240. https://doi.org/10.1021/jacs.8b10299.
(98) Aboul-Soud, M. A. M.; Al-Amri, M. Z.; Kumar, A.; Al-Sheikh, Y. A.; Ashour, A. E.; El-Kersh, T. A. Specific Cytotoxic Effects of Parasporal Crystal Proteins Isolated from Native Saudi Arabian Bacillus Thuringiensis Strains against Cervical Cancer Cells. *Molecules* **2019**, *24* (3), 506. https://doi.org/10.3390/molecules24030506.
(99) Stuart, J. D.; Hartman, D. A.; Gray, L. I.; Jones, A. A.; Wickenkamp, N. R.; Hirt, C.; Safira, A.; Regas, A. R.; Kondash, T. M.; Yates, M. L.; Driga, S.; Snow, C. D.; Kading, R. C. Mosquito Tagging Using DNA-Barcoded Nanoporous Protein Microcrystals. *PNAS Nexus* **2022**, *1* (4), pgac190. https://doi.org/10.1093/pnasnexus/pgac190.
(100) Kiseleva, A. P.; Krivoshapkin, P. V.; Krivoshapkina, E. F. Recent Advances in Development of Functional Spider Silk-Based Hybrid Materials. *Frontiers in Chemistry* **2020**, *8*.
(101) Aigner, T. B.; DeSimone, E.; Scheibel, T. Biomedical Applications of Recombinant Silk-Based Materials. *Advanced Materials* **2018**, *30* (19), 1704636. https://doi.org/10.1002/adma.201704636.
(102) Wise, S. G.; Mithieux, S. M.; Weiss, A. S. Engineered Tropoelastin and Elastin-Based Biomaterials. *Adv Protein Chem Struct Biol* **2009**, *78*, 1–24. https://doi.org/10.1016/S1876-1623(08)78001-5.
(103) Zhao, S.; Ye, X.; Dai, X.; Wang, X.; Yu, S.; Zhong, B. Drosophila Melanogaster Resilin Improves the Mechanical Properties of Transgenic Silk. *PLoS One* **2023**, *18* (3), e0282533. https://doi.org/10.1371/journal.pone.0282533.
(104) Balu, R.; Dutta, N. K.; Dutta, A. K.; Choudhury, N. R. Resilin-Mimetics as a Smart Biomaterial Platform for Biomedical Applications. *Nat Commun* **2021**, *12* (1), 149. https://doi.org/10.1038/s41467-020-20375-x.
(105) Zeng, R.; Tang, K.; Tian, H.; Pei, Y. Collagen Materials with Oriented Structure for Biomedical Applications. *Journal of Polymer Science n/a* (n/a). https://doi.org/10.1002/pol.20230664.
(106) Tran, H. A.; Hoang, T. T.; Maraldo, A.; Do, T. N.; Kaplan, D. L.; Lim, K. S.; Rnjak-Kovacina, J. Emerging Silk Fibroin Materials and Their Applications: New Functionality Arising from Innovations in Silk Crosslinking. *Materials Today* **2023**, *65*, 244–259. https://doi.org/10.1016/j.mattod.2023.03.027.
(107) Fang, W.; Fan, R.; Aranko, A. S.; Hummel, M.; Sixta, H. Upcycling of Keratin Wastes in Sustainable Textile Fiber Applications. *ACS Sustainable Chem. Eng.* **2023**, *11* (40), 14807–14815. https://doi.org/10.1021/acssuschemeng.3c04987.
(108) Hartje, L. F.; Andales, D. A.; Gintner, L. P.; Johnson, L. B.; Li, Y. V.; Snow, C. D. Textile Functionalization by Porous Protein Crystal Conjugation and Guest Molecule Loading. *Crystals* **2023**, *13* (2). https://doi.org/10.3390/cryst13020352.
(109) Culbert, N. J.; Kaiser, M.; Venter, N.; Vreysen, M. J. B.; Gilles, J. R. L.; Bouyer, J. A Standardised Method of Marking Male Mosquitoes with Fluorescent Dust. *Parasites & Vectors* **2020**, *13* (1), 192. https://doi.org/10.1186/s13071-020-04066-6.
(110) Silver, J. B. *Mosquito Ecology: Field Sampling Methods*, 3rd edition.; Springer: Dordrecht, 2007.
(111) Kelly, D. C.; Raftery, R. M.; Curtin, C. M.; O'Driscoll, C. M.; O'Brien, F. J. Scaffold-Based Delivery of Nucleic Acid Therapeutics for Enhanced Bone and Cartilage Repair. *Journal of Orthopaedic Research* **2019**, *37* (8), 1671–1680. https://doi.org/10.1002/jor.24321.

(112) Chen, X.; Mangala, L. S.; Rodriguez-Aguayo, C.; Kong, X.; Lopez-Berestein, G.; Sood, A. K. RNA Interference-Based Therapy and Its Delivery Systems. *Cancer and Metastasis Reviews* **2018**, *37* (1), 107–124. https://doi.org/10.1007/s10555-017-9717-6.
(113) Guimarães, D.; Cavaco-Paulo, A.; Nogueira, E. Design of Liposomes as Drug Delivery System for Therapeutic Applications. *International Journal of Pharmaceutics* **2021**, *601*, 120571. https://doi.org/10.1016/j.ijpharm.2021.120571.
(114) Amiri, A.; Bagherifar, R.; Ansari Dezfouli, E.; Kiaie, S. H.; Jafari, R.; Ramezani, R. Exosomes as Bio-Inspired Nanocarriers for RNA Delivery: Preparation and Applications. *Journal of Translational Medicine* **2022**, *20* (1), 125. https://doi.org/10.1186/s12967-022-03325-7.
(115) Dongen, H. M. van; Masoumi, N.; Witwer, K. W.; Pegtel, D. M. Extracellular Vesicles Exploit Viral Entry Routes for Cargo Delivery. **2016**. https://doi.org/10.1128/MMBR.00063-15.
(116) O'Brien, K.; Breyne, K.; Ughetto, S.; Laurent, L. C.; Breakefield, X. O. RNA Delivery by Extracellular Vesicles in Mammalian Cells and Its Applications. *Nat Rev Mol Cell Biol* **2020**, *21* (10), 585–606. https://doi.org/10.1038/s41580-020-0251-y.
(117) Mitchell, M. J.; Billingsley, M. M.; Haley, R. M.; Wechsler, M. E.; Peppas, N. A.; Langer, R. Engineering Precision Nanoparticles for Drug Delivery. *Nature Reviews Drug Discovery* **2021**, *20* (2), 101–124. https://doi.org/10.1038/s41573-020-0090-8.
(118) Pozdniakova, N.; Generalov, E.; Shevelev, A.; Tarasova, O. RNA Therapeutics: Delivery Problems and Solutions-A Review. *Pharmaceutics* **2025**, *17* (10), 1305. https://doi.org/10.3390/pharmaceutics17101305.
(119) Hartje, L. F.; Snow, C. D. Protein Crystal Based Materials for Nanoscale Applications in Medicine and Biotechnology. *Wiley Interdisciplinary Reviews: Nanomedicine and Nanobiotechnology* **2019**, *11* (4), e1547. https://doi.org/10.1002/wnan.1547.
(120) Khanh Nguyen, T.; Toan Pham, T.; Ueno, T. Engineering of Protein Crystals for Development of Bionanomaterials. *Japanese Journal of Applied Physics* **2019**, *58* (SI), SI0802. https://doi.org/10.7567/1347-4065/ab1399.
(121) Arthur Jones, A.; D. Snow, C. Porous Protein Crystals: Synthesis and Applications. *Chemical Communications* **2024**, *60* (45), 5790–5803. https://doi.org/10.1039/D4CC00183D.
(122) Chen, S.; Stuart, J. D.; Munsky, B.; Snow, C. D. Characterization of Guest DNA Transport and Adsorption within Host Porous Protein Crystals. *Langmuir* **2024**, *40* (50), 26443–26454. https://doi.org/10.1021/acs.langmuir.4c02960.
(123) Imamura, H.; Nhat, K. P.; Togawa, H.; Saito, K.; Iino, R.; Kato-Yamada, Y.; Nagai, T.; Noji, H. Visualization of ATP Levels inside Single Living Cells with Fluorescence Resonance Energy Transfer-Based Genetically Encoded Indicators. *Proceedings of the National Academy of Sciences of the United States of America* **2009**, *106* (37), 15651–15656. https://doi.org/10.1073/pnas.0904764106.
(124) Lapashina, A. S.; Tretyakov, D. O.; Feniouk, B. A. ATP in Mitochondria: Quantitative Measurement, Regulation, and Physiological Role. *Biochemistry (Moscow)* **2025**, *90* (12), 1929–1943. https://doi.org/10.1134/S0006297925603338.
(125) Martin, R. W.; Zilm, K. W. Preparation of Protein Nanocrystals and Their Characterization by Solid State NMR. *J Magn Reson* **2003**, *165* (1), 162–174.
(126) Durbin, S. D.; Feher, G. Crystal Growth Studies of Lysozyme as a Model for Protein Crystallization. *Journal of Crystal Growth* **1986**, *76* (3), 583–592. https://doi.org/10.1016/0022-0248(86)90175-2.
(127) Guilloteau, J.-P.; Rie`s-Kautt, M. M.; Ducruix, A. F. Variation of Lysozyme Solubility as a Function of Temperature in the Presence of Organic and Inorganic Salts. *Journal of Crystal Growth* **1992**, *122* (1), 223–230. https://doi.org/10.1016/0022-0248(92)90249-I.
(128) Antonov, J.; Goldstein, D. R.; Oberli, A.; Baltzer, A.; Pirotta, M.; Fleischmann, A.; Altermatt, H. J.; Jaggi, R. Reliable Gene Expression Measurements from Degraded RNA by Quantitative Real-Time PCR Depend on Short Amplicons and a Proper Normalization. *Laboratory Investigation* **2005**, *85* (8), 1040–1050. https://doi.org/10.1038/labinvest.3700303.

(129) Whiteheart, S. W.; Schraw, T.; Matveeva, E. A. N-Ethylmaleimide Sensitive Factor (NSF) Structure and Function. In *International Review of Cytology*; Academic Press, 2001; Vol. 207, pp 71–112. https://doi.org/10.1016/S0074-7696(01)07003-6.
(130) Yu, R. C.; Hanson, P. I.; Jahn, R.; Brünger, A. T. Structure of the ATP-Dependent Oligomerization Domain of N-Ethylmaleimide Sensitive Factor Complexed with ATP. *Nature Structural Biology* **1998**, *5* (9), 803–811. https://doi.org/10.1038/1843.
(131) Kothalawala, S. G.; Jiao, J.; Speight, R.; Song, H.; Yang, Y.; Zhang, J. Pore Architecture Influences the Enzyme Immobilization Performance of Mesoporous Silica Nanospheres. *Microporous and Mesoporous Materials* **2022**, *338*, 111963. https://doi.org/10.1016/j.micromeso.2022.111963.
(132) Ballin, J. D.; Prevas, J. P.; Ross, C. R.; Toth, E. A.; Wilson, G. M.; M. Thomas Record, J. Contributions of the Histidine Side Chain and the N-Terminal α-Amino Group to the Binding Thermodynamics of Oligopeptides to Nucleic Acids as a Function of pH. *Biochemistry* **2010**, *49* (9), 2018. https://doi.org/10.1021/bi902027z.
(133) Iacobucci, V.; Di Giuseppe, F.; Bui, T. T.; Vermeer, L. S.; Patel, J.; Scherman, D.; Kichler, A.; Drake, A. F.; Mason, A. J. Control of pH Responsive Peptide Self-Association during Endocytosis Is Required for Effective Gene Transfer. *Biochimica et Biophysica Acta* **2012**, *1818* (5), 1332–1341. https://doi.org/10.1016/j.bbamem.2011.12.018.
(134) Chou, S. T.; Hom, K.; Zhang, D.; Leng, Q.; Tricoli, L. J.; Hustedt, J. M.; Lee, A.; Shapiro, M. J.; Seog, J.; Kahn, J. D.; Mixson, A. J. Enhanced Silencing and Stabilization of siRNA Polyplexes by Histidine-Mediated Hydrogen Bonds. *Biomaterials* **2014**, *35* (2), 846–855. https://doi.org/10.1016/j.biomaterials.2013.10.019.
(135) Prazeres, D. M. Prediction of Diffusion Coefficients of Plasmids. *Biotechnology and Bioengineering* **2008**, *99* (4), 1040–1044. https://doi.org/10.1002/bit.21626.
(136) Latulippe, D. R.; Zydney, A. L. Size Exclusion Chromatography of Plasmid DNA Isoforms. *Journal of Chromatography A* **2009**, *1216* (35), 6295–6302. https://doi.org/10.1016/j.chroma.2009.07.009.
(137) Vaney, M. C.; Maignan, S.; Riès-Kautt, M.; Ducruix, A. High-Resolution Structure (1.33 Å) of a HEW Lysozyme Tetragonal Crystal Grown in the APCF Apparatus. Data and Structural Comparison with a Crystal Grown under Microgravity from SpaceHab-01 Mission. *Acta Crystallographica Section D* **1996**, *52* (3), 505–517. https://doi.org/10.1107/S090744499501674X.
(138) Zakharova, S. S.; Jesse, W.; Backendorf, C.; Egelhaaf, S. U.; Lapp, A.; van der Maarel, J. R. C. Dimensions of Plectonemically Supercoiled DNA. *Biophysical Journal* **2002**, *83* (2), 1106–1118. https://doi.org/10.1016/S0006-3495(02)75234-X.
(139) Regtmeier, J.; Eichhorn, R.; Bogunovic, L.; Ros, A.; Anselmetti, D. Dielectrophoretic Trapping and Polarizability of DNA: The Role of Spatial Conformation. *Analytical Chemistry* **2010**, *82* (17), 7141–7149. https://doi.org/10.1021/ac1005475.
(140) Spång, H. C.; Braathen R Fau - Bogen, B.; Bogen, B. Heterodimeric Barnase-Barstar Vaccine Molecules: Influence of One versus Two Targeting Units Specific for Antigen Presenting Cells. No. 1932-6203 (Electronic).
(141) Avraham, O.; Levi-Kalisman, Y.; Livnah, O. Generating a High Valency Biotin Binder by Selecting Uniform Protein Assemblies via Crystallization. *Crystals* **2019**, *9* (7). https://doi.org/10.3390/cryst9070353.
(142) Arnaout, R.; Lee, R. A.; Lee, G. R.; Callahan, C.; Cheng, A.; Yen, C. F.; Smith, K. P.; Arora, R.; Kirby, J. E. The Limit of Detection Matters: The Case for Benchmarking Severe Acute Respiratory Syndrome Coronavirus 2 Testing. *Clin Infect Dis* **2021**, *73* (9), e3042–e3046. https://doi.org/10.1093/cid/ciaa1382.
(143) Ke, Z.; Oton, J.; Qu, K.; Cortese, M.; Zila, V.; McKeane, L.; Nakane, T.; Zivanov, J.; Neufeldt, C. J.; Cerikan, B.; Lu, J. M.; Peukes, J.; Xiong, X.; Kräusslich, H.-G.; Scheres, S. H. W.; Bartenschlager, R.; Briggs, J. A. G. Structures and Distributions of SARS-CoV-2 Spike Proteins on Intact Virions. *Nature* **2020**, *588* (7838), 498–502. https://doi.org/10.1038/s41586-020-2665-2.
(144) Fonseca, M. S.; Machado, B. A. S.; Rolo, C. de A.; Hodel, K. V. S.; Almeida, E. dos S.; de Andrade, J. B. Evaluation of SARS-CoV-2 Concentrations in Wastewater and River Water Samples. *Case*

Studies in Chemical and Environmental Engineering **2022**, *6*, 100214. https://doi.org/10.1016/j.cscee.2022.100214.

(145) Torii, S.; Oishi, W.; Zhu, Y.; Thakali, O.; Malla, B.; Yu, Z.; Zhao, B.; Arakawa, C.; Kitajima, M.; Hata, A.; Ihara, M.; Kyuwa, S.; Sano, D.; Haramoto, E.; Katayama, H. Comparison of Five Polyethylene Glycol Precipitation Procedures for the RT-qPCR Based Recovery of Murine Hepatitis Virus, Bacteriophage Phi6, and Pepper Mild Mottle Virus as a Surrogate for SARS-CoV-2 from Wastewater. *Science of The Total Environment* **2022**, *807*, 150722. https://doi.org/10.1016/j.scitotenv.2021.150722.

(146) Peng, S.; Bie, B.; Sun, Y.; Liu, M.; Cong, H.; Zhou, W.; Xia, Y.; Tang, H.; Deng, H.; Zhou, X. Metal-Organic Frameworks for Precise Inclusion of Single-Stranded DNA and Transfection in Immune Cells. *Nature Communications* **2018**, *9* (1), 1293. https://doi.org/10.1038/s41467-018-03650-w.

(147) Li, Y.; Zhang, K.; Liu, P.; Chen, M.; Zhong, Y.; Ye, Q.; Wei, M. Q.; Zhao, H.; Tang, Z. Encapsulation of Plasmid DNA by Nanoscale Metal-Organic Frameworks for Efficient Gene Transportation and Expression. *Advanced Materials* **2019**, *31* (29), e1901570. https://doi.org/10.1002/adma.201901570.

(148) FitzGerald, L. I.; Hahn, E. E.; Wallace, M.; Stephenson, S. A.; Berry, O. F.; Doherty, C. M. Capture and Protection of Environmental DNA in a Metal-Organic Framework. *Small Science* **2024**, *4* (12), 2400432. https://doi.org/10.1002/smsc.202400432.

(149) Tan, T. K.; Rijal, P.; Rahikainen, R.; Keeble, A. H.; Schimanski, L.; Hussain, S.; Harvey, R.; Hayes, J. W. P.; Edwards, J. C.; McLean, R. K.; Martini, V.; Pedrera, M.; Thakur, N.; Conceicao, C.; Dietrich, I.; Shelton, H.; Ludi, A.; Wilsden, G.; Browning, C.; Zagrajek, A. K.; Bialy, D.; Bhat, S.; Stevenson-Leggett, P.; Hollinghurst, P.; Tully, M.; Moffat, K.; Chiu, C.; Waters, R.; Gray, A.; Azhar, M.; Mioulet, V.; Newman, J.; Asfor, A. S.; Burman, A.; Crossley, S.; Hammond, J. A.; Tchilian, E.; Charleston, B.; Bailey, D.; Tuthill, T. J.; Graham, S. P.; Duyvesteyn, H. M. E.; Malinauskas, T.; Huo, J.; Tree, J. A.; Buttigieg, K. R.; Owens, R. J.; Carroll, M. W.; Daniels, R. S.; McCauley, J. W.; Stuart, D. I.; Huang, K.-Y. A.; Howarth, M.; Townsend, A. R. A COVID-19 Vaccine Candidate Using SpyCatcher Multimerization of the SARS-CoV-2 Spike Protein Receptor-Binding Domain Induces Potent Neutralising Antibody Responses. *Nat Commun* **2021**, *12* (1), 542. https://doi.org/10.1038/s41467-020-20654-7.

(150) Karoyan, P.; Vieillard, V.; Gómez-Morales, L.; Odile, E.; Guihot, A.; Luyt, C.-E.; Denis, A.; Grondin, P.; Lequin, O. Human ACE2 Peptide-Mimics Block SARS-CoV-2 Pulmonary Cells Infection. *Communications Biology* **2021**, *4* (1), 197. https://doi.org/10.1038/s42003-021-01736-8.

(151) Maria, R.; Alessia, R.; Flavia, S.; Rita, B. An Engineered Stable Mini-Protein to Plug SARS-Cov-2 Spikes. *bioRxiv* **2020**, 2020.04.29.067728. https://doi.org/10.1101/2020.04.29.067728.

(152) Cao, L.; Goreshnik, I.; Coventry, B.; Case, J. B.; Miller, L.; Kozodoy, L.; Chen, R. E.; Carter, L.; Walls, A. C.; Park, Y.-J.; Strauch, E.-M.; Stewart, L.; Diamond, M. S.; Veesler, D.; Baker, D. De Novo Design of Picomolar SARS-CoV-2 Miniprotein Inhibitors. *Science* **2020**, *370* (6515), 426–431. https://doi.org/10.1126/science.abd9909.

(153) Hartje, L. F.; Munsky, B.; Ni, T. W.; Ackerson, C. J.; Snow, C. D. Adsorption-Coupled Diffusion of Gold Nanoclusters within a Large-Pore Protein Crystal Scaffold. *J Phys Chem B* **2017**, *121* (32), 7652–7659. https://doi.org/10.1021/acs.jpcb.7b03999.

(154) Thom, R. E.; Eastaugh, L. S.; O'Brien, L. M.; Ulaeto, D. O.; Findlay, J. S.; Smither, S. J.; Phelps, A. L.; Stapleton, H. L.; Hamblin, K. A.; Weller, S. A. Evaluation of the SARS-CoV-2 Inactivation Efficacy Associated With Buffers From Three Kits Used on High-Throughput RNA Extraction Platforms. *Frontiers in Cellular and Infection Microbiology* **2021**, *11*, 716436. https://doi.org/10.3389/fcimb.2021.716436.

(155) Tyler, J.; Ralston, C. Y.; Rad, B. Sneaking in SpyCatcher Using Cell Penetrating Peptides for in Vivo Imaging. *Nanotechnology* **2023**, *34* (42), 425101. https://doi.org/10.1088/1361-6528/acdf65.

(156) Guo, K.; Grünberg, R.; Ren, Y.; Chang, T.; Wustoni, S.; Strnad, O.; Koklu, A.; Díaz-Galicia, E.; Agudelo, J. P.; Druet, V.; Castillo, T. C. H.; Moser, M.; Ohayon, D.; Hama, A.; Dada, A.;

McCulloch, I.; Viola, I.; Arold, S. T.; Inal, S. SpyDirect: A Novel Biofunctionalization Method for High Stability and Longevity of Electronic Biosensors. *Advanced Science* **2024**, *11* (27), e2306716. https://doi.org/10.1002/advs.202306716.

(157) Gardy, J. L.; Loman, N. J. Towards a Genomics-Informed, Real-Time, Global Pathogen Surveillance System. *Nature Reviews Genetics* **2018**, *19* (1), 9–20. https://doi.org/10.1038/nrg.2017.88.

(158) Quick, J.; Grubaugh, N. D.; Pullan, S. T.; Claro, I. M.; Smith, A. D.; Gangavarapu, K.; Oliveira, G.; Robles-Sikisaka, R.; Rogers, T. F.; Beutler, N. A.; Burton, D. R.; Lewis-Ximenez, L. L.; de Jesus, J. G.; Giovanetti, M.; Hill, S. C.; Black, A.; Bedford, T.; Carroll, M. W.; Nunes, M.; Alcantara, L. C.; Sabino, E. C.; Baylis, S. A.; Faria, N. R.; Loose, M.; Simpson, J. T.; Pybus, O. G.; Andersen, K. G.; Loman, N. J. Multiplex PCR Method for MinION and Illumina Sequencing of Zika and Other Virus Genomes Directly from Clinical Samples. *Nature Protocols* **2017**, *12* (6), 1261–1276. https://doi.org/10.1038/nprot.2017.066.

(159) Herigstad, M. O.; Dimartino, S.; Boi, C.; Sarti, G. C. Experimental Characterization of the Transport Phenomena, Adsorption, and Elution in a Protein A Affinity Monolithic Medium. *Journal of Chromatography A* **2015**, *1407*, 130–138. https://doi.org/10.1016/j.chroma.2015.06.045.

(160) Burden, C. S.; Jin, J.; Podgornik, A.; Bracewell, D. G. A Monolith Purification Process for Virus-like Particles from Yeast Homogenate. *Journal of Chromatography B: Analytical Technologies in the Biomedical and Life Sciences* **2012**, *880* (1), 82–89. https://doi.org/10.1016/j.jchromb.2011.10.044.

(161) Fernández-Penas, R.; Verdugo-Escamilla, C.; Martínez-Rodríguez, S.; Gavira, J. A. Production of Cross-Linked Lipase Crystals at a Preparative Scale. *Crystal Growth & Design* **2021**, *21* (3), 1698–1707. https://doi.org/10.1021/acs.cgd.0c01608.

(162) Stubbs, J.; Tremlett, C. J.; Waitman, A.; Harmer, N. J.; Orville, A. M.; Tews, I.; Kolek, S.; Shaw Stewart, P. D. Automated Microbatch-under-Oil Phase Diagrams to Rationalize Serial Crystallography Sample Preparation. *IUCrJ* **2026**, *13* (2), 159–168. https://doi.org/10.1107/S2052252526000448.

(163) Kober, U. A.; Ogbuoji, E. A.; Hutchinson, J. A.; Mueser, T. C.; Schall, C. A. Equilibration of Precipitants in a Counter-Diffusion Apparatus for Protein Crystallization. *Journal of Applied Crystallography* **2023**, *56*, 1057–1065.

(164) Gong, H.; Holcomb, I.; Ooi, A.; Wang, X.; Majonis, D.; Unger, M. A.; Ramakrishnan, R. Simple Method To Prepare Oligonucleotide-Conjugated Antibodies and Its Application in Multiplex Protein Detection in Single Cells. *Bioconjugate Chemistry* **2016**, *27* (1), 217–225. https://doi.org/10.1021/acs.bioconjchem.5b00613.

(165) Liu, Y.; Hou, W.; Sun, H.; Cui, C.; Zhang, L.; Jiang, Y.; Wu, Y.; Wang, Y.; Li, J.; Sumerlin, B. S.; Liu, Q.; Tan, W. Thiol-Ene Click Chemistry: A Biocompatible Way for Orthogonal Bioconjugation of Colloidal Nanoparticles. *Chemical Science* **2017**, *8* (9), 6182–6187. https://doi.org/10.1039/c7sc01447c.

(166) Wityk, P.; Piątek, R.; Nowak, R.; Kostrzewa-Nowak, D. Generation and Characterization of a DNA-GCN4 Oligonucleotide-Peptide Conjugate: The Impact DNA/Protein Interactions on the Sensitization of DNA. *Molecules* **2020**, *25* (16), 3630. https://doi.org/10.3390/molecules25163630.

(167) Lu, T. C.; Lin, Y. T.; Xiao, W. B.; Qiu, Q. Z.; Tian, H. Y.; Lei, Y.; Liu, A. L. Reagent-Free Anti-Fouling Electrochemical Immunosensor Based on AL-BSA/AuNPs/PANI Coating for the Point-of-Care Detection of C-Reactive Protein in Plasma and Whole Blood. *Biosensors and Bioelectronics* **2024**, *264*, 116667. https://doi.org/10.1016/j.bios.2024.116667.

(168) Wang, Z.; Zhang, C.-M.; Li, C.-X.; Li, Y.-F.; Mou, X.; You, R. Evaluation of Adsorption-Elution Methods with Positively and Negatively Charged Membranes for Virus Concentration in Municipal Wastewater: New Insight into Effects of Dissolved Organic Matter. *Journal of Environmental Chemical Engineering* **2022**, *10* (3), 107875. https://doi.org/10.1016/j.jece.2022.107875.

(169) Sharma, S.; Kaur, G.; Deep, A.; Nayak, M. K. A Multifunctional Recyclable Adsorbent Based on Engineered MIL-125 (Ti) Magnetic Mesoporous Composite for the Effective Removal of

Pathogens. *Environmental Research* **2023**, *233*, 116496. https://doi.org/10.1016/j.envres.2023.116496.
(170) He, Q.; Pan, J.; Xu, Z.; Hammock, B. D.; Li, D. Development of a Nanobody-Based Immunoassay for the Detection of Escherichia Coli O157:H7 in Food Samples. *Food Chemistry* **2025**, *473*, 142987. https://doi.org/10.1016/j.foodchem.2025.142987.
(171) Hu, W.; Liu, Y.; Li, X.; Lei, L.; Lin, H.; Yuan, Q.; Mao, D.; Luo, Y. Nanobody-Based Strategy for Rapid and Accurate Pathogen Detection: A Case of COVID-19 Testing. *Biosensors and Bioelectronics* **2024**, *263*, 116598. https://doi.org/10.1016/j.bios.2024.116598.
(172) Huang, Y. H.; Jiang, S. Quantification of Viruses in Wastewater on a Centrifugal Microfluidic Disc. *Environmental Science & Technology* **2025**, *59* (6), 3088–3097. https://doi.org/10.1021/acs.est.4c13718.
(173) Dehghan Banadaki, M.; Torabi, S.; Strike, W. D.; Phillips, A. R.; Sakhaei, A.; Farahbakhsh, S.; Noble, A.; Keck, J. W.; Berry, S. M. Enabling SARS-CoV-2 Wastewater Surveillance Using an Integrated Microfluidic Chip. *Analytical Chemistry* **2025**, *97* (25), 13140–13150. https://doi.org/10.1021/acs.analchem.5c00831.
(174) Gowda, H. N.; Kido, H.; Wu, X.; Shoval, O.; Lee, A.; Lorenzana, A.; Madou, M.; Hoffmann, M.; Jiang, S. C. Development of a Proof-of-Concept Microfluidic Portable Pathogen Analysis System for Water Quality Monitoring. *Science of the Total Environment* **2022**, *813*, 152556. https://doi.org/10.1016/j.scitotenv.2021.152556.
(175) Newman, S. P. Drug Delivery to the Lungs: Challenges and Opportunities. *Ther Deliv* **2017**, *8* (8), 647–661. https://doi.org/10.4155/tde-2017-0037.
(176) Labiris, N. R.; Dolovich, M. B. Pulmonary Drug Delivery. Part I: Physiological Factors Affecting Therapeutic Effectiveness of Aerosolized Medications. *Br J Clin Pharmacol* **2003**, *56* (6), 588–599. https://doi.org/10.1046/j.1365-2125.2003.01892.x.
(177) Labiris, N. R.; Dolovich, M. B. Pulmonary Drug Delivery. Part II: The Role of Inhalant Delivery Devices and Drug Formulations in Therapeutic Effectiveness of Aerosolized Medications. *Br J Clin Pharmacol* **2003**, *56* (6), 600–612. https://doi.org/10.1046/j.1365-2125.2003.01893.x.
(178) Zhang, Y. B.; Xu, D.; Bai, L.; Zhou, Y. M.; Zhang, H.; Cui, Y. L. A Review of Non-Invasive Drug Delivery through Respiratory Routes. *Pharmaceutics* **2022**, *14* (9). https://doi.org/10.3390/pharmaceutics14091974.
(179) Yeung, S.; Traini, D.; Lewis, D.; Young, P. M. Dosing Challenges in Respiratory Therapies. *International Journal of Pharmaceutics* **2018**, *548* (1), 659–671. https://doi.org/10.1016/j.ijpharm.2018.07.007.
(180) He, S.; Gui, J.; Xiong, K.; Chen, M.; Gao, H.; Fu, Y. A Roadmap to Pulmonary Delivery Strategies for the Treatment of Infectious Lung Diseases. *Journal of Nanobiotechnology* **2022**, *20* (1), 101. https://doi.org/10.1186/s12951-022-01307-x.
(181) Mathers, C. D.; Boerma, T.; Ma Fat, D. Global and Regional Causes of Death. *Br Med Bull* **2009**, *92*, 7–32. https://doi.org/10.1093/bmb/ldp028.
(182) Lopez, A. D.; Mathers, C. D. Measuring the Global Burden of Disease and Epidemiological Transitions: 2002-2030. *Ann Trop Med Parasitol* **2006**, *100* (5–6), 481–499. https://doi.org/10.1179/136485906X97417.
(183) Measuring the Global Burden of Disease and Risk Factors, 1990–2001. In *Global Burden of Disease and Risk Factors*; Lopez, A. D., Mathers, C. D., Eds.; World Bank / Oxford University Press: Washington, DC; New York, NY, 2006.
(184) Henjakovic, M.; Sewald, K.; Switalla, S.; Kaiser, D.; Muller, M.; Veres, T. Z.; Martin, C.; Uhlig, S.; Krug, N.; Braun, A. Ex Vivo Testing of Immune Responses in Precision-Cut Lung Slices. *Toxicol Appl Pharmacol* **2008**, *231* (1), 68–76. https://doi.org/10.1016/j.taap.2008.04.003.
(185) Lam, M.; Lamanna, E.; Organ, L.; Donovan, C.; Bourke, J. E. Perspectives on Precision Cut Lung Slices—Powerful Tools for Investigation of Mechanisms and Therapeutic Targets in Lung Diseases. *Frontiers in Pharmacology* **2023**, *14*, 1162889. https://doi.org/10.3389/fphar.2023.1162889.

(186) Liu, Y.; Wu, P.; Wang, Y.; Liu, Y.; Yang, H. Application of Precision-Cut Lung Slices as an In Vitro Model for Research of Inflammatory Respiratory Diseases. *Bioengineering (Basel)* **2022**, *9* (12). https://doi.org/10.3390/bioengineering9120589.
(187) Patlin, B.; Schwerdtfeger, L. A.; Tobet, S. A. Neuropeptide Stimulation of Physiological and Immunological Responses in Precision-cut Lung Slices. *Physiological Reports* **2023**, *11* (22), e15873. https://doi.org/10.14814/phy2.15873.
(188) Viana, F.; O'Kane, C. M.; Schroeder, G. N. Precision-cut Lung Slices: A Powerful Ex Vivo Model to Investigate Respiratory Infectious Diseases. *Molecular Microbiology* **2022**, *117* (3), 578–588. https://doi.org/10.1111/mmi.14817.
(189) Frohlich, E. Comparison of Conventional and Advanced in Vitro Models in the Toxicity Testing of Nanoparticles. *Artif Cells Nanomed Biotechnol* **2018**, *46* (sup2), 1091–1107. https://doi.org/10.1080/21691401.2018.1479709.
(190) Pearson, R. M. In-Vitro Techniques: Can They Replace Animal Testing? *Hum Reprod* **1986**, *1* (8), 559–560. https://doi.org/10.1093/oxfordjournals.humrep.a136473.
(191) Liu, G.; Betts, C.; Cunoosamy, D. M.; Åberg, P. M.; Hornberg, J. J.; Sivars, K. B.; al, et. Use of Precision Cut Lung Slices as a Translational Model for the Study of Lung Biology. *Respiratory Research* **2019**, *20* (1), 162. https://doi.org/10.1186/s12931-019-1131-x.
(192) Kokoszynska, M.; Ubags, N. D. J.; Bivona III, J. J.; Ventrone, S.; Reed, L. F.; Dixon, A. E. Storage Conditions of High-Fat Diets Affect Pulmonary Inflammation. *Physiological Reports* **2021**, *9* (22), e15116. https://doi.org/10.14814/phy2.15116.
(193) Avila-Calderón, E. D.; Ruiz-Palma, M. de los S.; Aguilera-Arreola, M. G.; Velázquez-Guadarrama, N.; Ruiz, E. A.; Gomez-Lunar, Z.; Witonsky, S.; Contreras-Rodríguez, A. Outer Membrane Vesicles of Gram-Negative Bacteria: An Outlook on Biogenesis. *Frontiers in Microbiology* **2021**, *12*, 557902. https://doi.org/10.3389/fmicb.2021.557902.
(194) Park, B. S.; Song, D.; Kim, H.; Choi, B.; Lee, J.; Lee, H.; Lee, J.; al, et. The Structural Basis of Lipopolysaccharide Recognition by the TLR4-MD-2 Complex. *Nature* **2009**, *458* (7242), 1191–1195. https://doi.org/10.1038/nature07830.
(195) Chilton, P. M.; Hadel, D. M.; To, T. T.; Mitchell, T. C.; Darveau, R. P. Adjuvant Activity of Naturally Occurring Monophosphoryl Lipopolysaccharide Preparations from Mucosa-associated Bacteria. *Infection and Immunity* **2013**, *81* (10), 3317–3325. https://doi.org/10.1128/IAI.00302-13.
(196) Melssen, M. M.; Petroni, G. R.; Chianese-Bullock, K. A.; Wages, N. A.; Grosh, W. W.; Varhegyi, N.; Smolkin, M. E.; Smith, K. T.; Galeassi, N. V.; Deacon, D. H.; Gaughan, E. M.; Slingluff, C. L., Jr. A Multipeptide Vaccine plus Toll-like Receptor Agonists LPS or polyICLC in Combination with Incomplete Freund's Adjuvant in Melanoma Patients. *J Immunother Cancer* **2019**, *7* (1), 163. https://doi.org/10.1186/s40425-019-0625-x.
(197) Casella, C. R.; Mitchell, T. C. Putting Endotoxin to Work for Us: Monophosphoryl Lipid A as a Safe and Effective Vaccine Adjuvant. *Cell Mol Life Sci* **2008**, *65* (20), 3231–3240. https://doi.org/10.1007/s00018-008-8228-6.
(198) Hawkins, E. D.; Turner, M. L.; Wellard, C. J.; Zhou, J. H. S.; Dowling, M. R.; Hodgkin, P. D. Quantal and Graded Stimulation of B Lymphocytes as Alternative Strategies for Regulating Adaptive Immune Responses. *Nature Communications* **2013**, *4*, 2406. https://doi.org/10.1038/ncomms3406.
(199) Anand, S.; Mande, S. S. Diet, Microbiota and Gut-Lung Connection. *Frontiers in Microbiology* **2018**, *9*, 2147. https://doi.org/10.3389/fmicb.2018.02147.
(200) Kaul, D.; Rathnasinghe, R.; Ferres, M.; Tan, G. S.; Barrera, A.; Pickett, B. E.; Methe, B. A.; Das, S. R.; Budnik, I.; Halpin, R. A.; Wentworth, D.; Schmolke, M.; Mena, I.; Albrecht, R. A.; Singh, I.; Nelson, K. E.; Garcia-Sastre, A.; Dupont, C. L.; Medina, R. A. Microbiome Disturbance and Resilience Dynamics of the Upper Respiratory Tract during Influenza A Virus Infection. *Nature Communications* **2020**, *11*, 3827. https://doi.org/10.1038/s41467-020-17664-3.

(201) Hussain, I.; Cher, G. L. Y.; Abid, M. A.; Abid, M. B. Role of Gut Microbiome in COVID-19: An Insight Into Pathogenesis and Therapeutic Potential. *Front Immunol* **2021**, *12*. https://doi.org/10.3389/fimmu.2021.765965.
(202) Heater, B. S.; Yang, Z.; Lee, M. M.; Chan, M. K. In Vivo Enzyme Entrapment in a Protein Crystal. *J. Am. Chem. Soc.* **2020**, *142* (22), 9879–9883. https://doi.org/10.1021/jacs.9b13462.
(203) Schwerdtfeger, L. A.; Ryan, E. P.; Tobet, S. A. An Organotypic Slice Model for Ex Vivo Study of Neural, Immune, and Microbial Interactions of Mouse Intestine. *Am J Physiol Gastrointest Liver Physiol* **2016**, *310* (4), G240-8. https://doi.org/10.1152/ajpgi.00299.2015.
(204) Smith, L. K.; Babcock, I. W.; Minamide, L. S.; Shaw, A. E.; Bamburg, J. R.; Kuhn, T. B. Direct Interaction of HIV Gp120 with Neuronal CXCR4 and CCR5 Receptors Induces Cofilin-Actin Rod Pathology via a Cellular Prion Protein- and NOX-Dependent Mechanism. *Plos One* **2021**, *16* (3). https://doi.org/10.1371/journal.pone.0248309.
(205) Byvaltsev, V. A.; Bardonova, L. A.; Onaka, N. R.; Polkin, R. A.; Ochkal, S. V.; Shepelev, V. V.; Aliyev, M. A.; Potapov, A. A. Acridine Orange: A Review of Novel Applications for Surgical Cancer Imaging and Therapy. *Front Oncol* **2019**, *9*, 925. https://doi.org/10.3389/fonc.2019.00925.
(206) Xu, H.; Liew, L. N.; Kuo, I.; Huang, C. C.; Goh, D. L.; Chua, K. Y. The Modulatory Effects of Lipopolysaccharide-stimulated B Cells on Differential T-cell Polarization. *Immunology* **2008**, *125*, 218–228. https://doi.org/10.1111/j.1365-2567.2008.02811.x.
(207) Venkataraman, C.; Lu, P. J.; Buhl, A. M.; Chen, C. S.; Cambier, J. C.; Bondada, S. Bacterial Lipopolysaccharide Induced B Cell Activation Is Mediated via a Phosphatidylinositol 3-Kinase Dependent Signaling Pathway. *Immunology Letters* **1999**, *69* (2), 233–238. https://doi.org/10.1016/S0165-2478(99)00068-1.
(208) Patlin, B. Calcitonin Gene Related Peptide (CGRP) Modulates B Cells in the Lung Neuroimmune Axis. In *Society for Neuroscience Annual Meeting*; 2022.
(209) Palange, A. L.; Di Mascolo, D.; Ferreira, M.; Gawne, P. J.; Spanò, R.; Felici, A.; Bono, L.; Moore, T. L.; Salerno, M.; Armirotti, A.; Decuzzi, P. Boosting the Potential of Chemotherapy in Advanced Breast Cancer Lung Metastasis via Micro-Combinatorial Hydrogel Particles. *Advanced Science* **2023**, *10* (10), e2205223. https://doi.org/10.1002/advs.202205223.
(210) Kubiak, M.; Storm, K. F.; Kampen, I.; Schilde, C. Relationship between Cross-Linking Reaction Time and Anisotropic Mechanical Behavior of Enzyme Crystals. *Crystal Growth & Design* **2019**, *19* (8), 4453–4464. https://doi.org/10.1021/acs.cgd.9b00593.
(211) Shen, S.; Wu, Y.; Liu, Y.; Wu, D. High Drug-Loading Nanomedicines: Progress, Current Status, and Prospects. *International Journal of Nanomedicine* **2017**, *12*, 4085–4109. https://doi.org/10.2147/IJN.S132780.
(212) Khalbas, A. H.; Albayati, T. M.; Ali, N. S.; Salih, I. K. Drug Loading Methods and Kinetic Release Models Using Mesoporous Silica Nanoparticles as a Drug Delivery System: A Review. *South African Journal of Chemical Engineering* **2024**, *50*, 261–280. https://doi.org/10.1016/j.sajce.2024.08.013.
(213) Singh, L. P.; Bhattacharyya, S. K.; Kumar, R.; Mishra, G.; Sharma, U.; Singh, G.; Ahalawat, S. Sol-Gel Processing of Silica Nanoparticles and Their Applications. *Advances in Colloid and Interface Science* **2014**, *214*, 17–37. https://doi.org/10.1016/j.cis.2014.10.007.
(214) Fornaguera, C.; Dols-Perez, A.; Calderó, G.; García-Celma, M. J.; Camarasa, J.; Solans, C. PLGA Nanoparticles Prepared by Nano-Emulsion Templating Using Low-Energy Methods as Efficient Nanocarriers for Drug Delivery across the Blood-Brain Barrier. *Journal of Controlled Release* **2015**, *211*, 134–143. https://doi.org/10.1016/j.jconrel.2015.06.002.
(215) Shepherd, S. J.; Issadore, D.; Mitchell, M. J. Microfluidic Formulation of Nanoparticles for Biomedical Applications. *Biomaterials* **2021**, *274*, 120826. https://doi.org/10.1016/j.biomaterials.2021.120826.
(216) Gimondi, S.; Ferreira, H.; Reis, R. L.; Neves, N. M. Microfluidic Devices: A Tool for Nanoparticle Synthesis and Performance Evaluation. *ACS Nano* **2023**, *17* (15), 14205–14228. https://doi.org/10.1021/acsnano.3c01117.

(217) Friedman, A. D.; Claypool, S. E.; Liu, R. The Smart Targeting of Nanoparticles. *Current Pharmaceutical Design* **2013**, *19* (35), 6315–6329. https://doi.org/10.2174/1381612811319990375.
(218) Yetisgin, A. A.; Cetinel, S.; Zuvin, M.; Kosar, A.; Kutlu, O. Therapeutic Nanoparticles and Their Targeted Delivery Applications. *Molecules* **2020**, *25* (9), 2193. https://doi.org/10.3390/molecules25092193.
(219) Gamucci, O.; Bertero, A.; Gagliardi, M.; Bardi, G. Biomedical Nanoparticles: Overview of Their Surface Immune-Compatibility. *Coatings* **2014**, *4* (1), 139–159. https://doi.org/10.3390/coatings4010139.
(220) Seeman, N. C. Nucleic Acid Junctions and Lattices. *Journal of Theoretical Biology* **1982**, *99* (2), 237–247. https://doi.org/10.1016/0022-5193(82)90002-9.
(221) Skotland, T.; Iversen, T. G.; Llorente, A.; Sandvig, K. Biodistribution, Pharmacokinetics and Excretion Studies of Intravenously Injected Nanoparticles and Extracellular Vesicles: Possibilities and Challenges. *Advanced Drug Delivery Reviews* **2022**, *186*, 114326. https://doi.org/10.1016/j.addr.2022.114326.
(222) Salerno, I.; Dunn, N.; White, H.; Miyazaki, W.; Jeziorski, K.; Silvestros, D.; Jha, A.; Laforest, R.; Akerele, M. I.; Thomas, M. A.; Thorek, D. L. J. Quantitative Comparison of SPECT and PET Performance for Clinical Theranostic Applications. *J Nucl Med* **2025**, jnumed.125.270987. https://doi.org/10.2967/jnumed.125.270987.
(223) Pavlicek, A.; Neubauer, S.; Zafiu, C.; Huber-Humer, M.; Ehmoser, E.-K.; Part, F. The Use and Detection of Quantum Dots as Nanotracers in Environmental Fate Studies of Engineered Nanoparticles. *Environmental Pollution* **2023**, *317*, 120461. https://doi.org/10.1016/j.envpol.2022.120461.
(224) Dave, R.; Terry, D. S.; Munro, J. B.; Blanchard, S. C. Mitigating Unwanted Photophysical Processes for Improved Single-Molecule Fluorescence Imaging. *Biophysical Journal* **2009**, *96* (6), 2371–2381. https://doi.org/10.1016/j.bpj.2008.11.061.
(225) Kim, H. K.; Lee, G. H.; Chang, Y. Gadolinium as an MRI Contrast Agent. *Future Medicinal Chemistry* **2018**, *10* (6), 639–661. https://doi.org/10.4155/fmc-2017-0215.
(226) Rahman, M. Magnetic Resonance Imaging and Iron-Oxide Nanoparticles in the Era of Personalized Medicine. *Nanotheranostics* **2023**, *7* (4), 424–449. https://doi.org/10.7150/ntno.86467.
(227) Toledo-Garcia, P.; Argüelles-Luyo, C.; Donayre-Torres, A. Engineering a Fusion Protein Biomaterial Based on SpyTag/SpyCatcher Bioconjugation of Elastin and Collagen Synthetic Proteins. *ACS Omega* **2025**, *10* (16), 16245–16256. https://doi.org/10.1021/acsomega.4c10313.
(228) Nguyen, P. Q.; Botyanszki, Z.; Tay, P. K. R.; Joshi, N. S. Programmable Biofilm-Based Materials from Engineered Curli Nanofibres. *Nat Commun* **2014**, *5* (1), 4945. https://doi.org/10.1038/ncomms5945.
(229) Hinrichsen, M.; Lenz, M.; Edwards, J. M.; Miller, O. K.; Mochrie, S. G. J.; Swain, P. S.; Schwarz-Linek, U.; Regan, L. A New Method for Post-Translationally Labeling Proteins in Live Cells for Fluorescence Imaging and Tracking. *Protein Engineering Design and Selection* **2017**, *30* (12), 771–780. https://doi.org/10.1093/protein/gzx059.
(230) Kutscher, H. L.; Chao, P.-Y.; Deshmukh, M.; Singh, Y.; Hu, P.; Joseph, L. B.; Reimer, D. C.; Stein, S.; Laskin, D. L.; Sinko, P. J. Threshold Size for Optimal Passive Pulmonary Targeting and Retention of Rigid Microparticles in Rats. *Journal of Controlled Release* **2010**, *143* (1), 31–37. https://doi.org/10.1016/j.jconrel.2009.12.019.
(231) Bausart, M.; Bozzato, E.; Joudiou, N.; Koutsoumpou, X.; Manshian, B.; Préat, V.; Gallez, B. Mismatch between Bioluminescence Imaging (BLI) and MRI When Evaluating Glioblastoma Growth: Lessons from a Study Where BLI Suggested "Regression" While MRI Showed "Progression." *Cancers* **2023**, *15* (6), 1919. https://doi.org/10.3390/cancers15061919.
(232) Potter, R. F.; Groom, A. C. Capillary Diameter and Geometry in Cardiac and Skeletal Muscle Studied by Means of Corrosion Casts. *Microvascular Research* **1983**, *25* (1), 68–84. https://doi.org/10.1016/0026-2862(83)90044-4.

(233) Nicolas, N.; Roux, E. 3D Imaging and Quantitative Characterization of Mouse Capillary Coronary Network Architecture. *Biology (Basel)* **2021**, *10* (4), 306. https://doi.org/10.3390/biology10040306.
(234) d'Aquino, A. I.; Dong, C.; Nguyen, L. T.; Yan, J.; Jons, C. K.; Saouaf, O. M.; Song, Y. E.; Eckman, N.; Kapasi, S.; Williams, C. M.; Doulames, V. M.; Sen, S.; Manna, M. K.; Alakesh, A.; Lu, K.; Hall, I.; Appel, E. A. Long-Acting Hydrogel-Based Depot Formulations of Tirzepatide and Semaglutide for the Management of Type 2 Diabetes and Weight. *bioRxiv* **2025**, 2025.07.02.662867. https://doi.org/10.1101/2025.07.02.662867.
(235) Park, K. PLGA-Based Long-Acting Injectable (LAI) Formulations. *Journal of Controlled Release* **2025**, *382*, 113758. https://doi.org/10.1016/j.jconrel.2025.113758.
(236) Zheng, T.; Doyle, P. S. Injectable Sustained-Release Hydrogel for High-Concentration Antibody Delivery. *RSC Pharmaceutics* **2024**, *2* (1), 186–196. https://doi.org/10.1039/D4PM00290C.
(237) HogenEsch, H. Mechanisms of Stimulation of the Immune Response by Aluminum Adjuvants. *Vaccine* **2002**, *20* (Supplement 3), S34–S39. https://doi.org/10.1016/S0264-410X(02)00169-X.
(238) Lan, J.; Feng, D.; He, X.; Zhang, Q.; Zhang, R. Basic Properties and Development Status of Aluminum Adjuvants Used for Vaccines. *Vaccines (Basel)* **2024**, *12* (10), 1187. https://doi.org/10.3390/vaccines12101187.
(239) Su, Y.; Zhang, B.; Sun, R.; Liu, W.; Zhu, Q.; Zhang, X.; Wang, R.; Chen, C. PLGA-Based Biodegradable Microspheres in Drug Delivery: Recent Advances in Research and Application. *Drug Delivery* **2021**, *28* (1), 1397–1418. https://doi.org/10.1080/10717544.2021.1938756.
(240) Suk, J. S.; Xu, Q.; Kim, N.; Hanes, J.; Ensign, L. M. PEGylation as a Strategy for Improving Nanoparticle-Based Drug and Gene Delivery. *Advanced Drug Delivery Reviews* **2016**, *99*, 28–51. https://doi.org/10.1016/j.addr.2015.09.012.
(241) Dierks, K.; Meyer, A.; Einspahr, H.; Betzel, C. Dynamic Light Scattering in Protein Crystallization Droplets: Adaptations for Analysis and Optimization of Crystallization Processes. *Crystal Growth & Design* **2008**, *8* (5), 1628–1634. https://doi.org/10.1021/cg701067r.
(242) Baitan, D.; Schubert, R.; Meyer, A.; Dierks, K.; Perbandt, M.; Betzel, C. Growing Protein Crystals with Distinct Dimensions Using Automated Crystallization Coupled with In Situ Dynamic Light Scattering. *JoVE* **2018**, No. 138, e57070. https://doi.org/10.3791/57070.
(243) Ozturk, K.; Kaplan, M.; Calis, S. Effects of Nanoparticle Size, Shape, and Zeta Potential on Drug Delivery. *International Journal of Pharmaceutics* **2024**, *666*, 124799. https://doi.org/10.1016/j.ijpharm.2024.124799.
(244) Cai, M.-M.; Ni, Z.-F.; Sun, Z.-K.; Li, X.-L.; Qi, Y.-L.; Wang, L.; He, C.; Li, C.-W. The SpyTag/SpyCatcher System: Precise Regulation of Covalent Conjugation and Expansion of Application Scenarios. *Biotechnology Journal* **2025**, *20* (10), e70131. https://doi.org/10.1002/biot.70131.
(245) Lehmann, M.; Krishnan, R.; Sucre, J.; Kulkarni, H. S.; Pineda, R. H.; Anderson, C.; Banovich, N. E.; Behrsing, H. P.; Dean, C. H.; Haak, A.; Gosens, R.; Kaminski, N.; Zagorska, A.; Koziol-White, C.; Metcalf, J. P.; Kim, Y. H.; Loebel, C.; Neptune, E.; Noel, A.; Raghu, G.; Sewald, K.; Sharma, A.; Suki, B.; Sperling, A.; Tatler, A.; Turner, S.; Rosas, I. O.; Van Ry, P.; Wille, T.; Randell, S. H.; Pryhuber, G.; Rojas, M.; Bourke, J.; Konigshoff, M. Precision-Cut Lung Slices: Emerging Tools for Preclinical and Translational Lung Research: An Official American Thoracic Society Workshop Report. *American Journal of Respiratory Cell and Molecular Biology* **2025**, *72* (1), 16–31. https://doi.org/10.1165/rcmb.2024-0479ST.
(246) Li, Z.; Wang, S.; Nattermann, U.; Bera, A. K.; Borst, A. J.; Yaman, M. Y.; Bick, M. J.; Yang, E. C.; Sheffler, W.; Lee, B.; Seifert, S.; Hura, G. L.; Nguyen, H.; Kang, A.; Dalal, R.; Lubner, J. M.; Hsia, Y.; Haddox, H.; Courbet, A.; Dowling, Q.; Miranda, M.; Favor, A.; Etemadi, A.; Edman, N. I.; Yang, W.; Weidle, C.; Sankaran, B.; Negahdari, B.; Ross, M. B.; Ginger, D. S.; Baker, D. Accurate Computational Design of Three-Dimensional Protein Crystals. *Nat. Mater.* **2023**, 1–8. https://doi.org/10.1038/s41563-023-01683-1.
(247) Watson, J. L.; Juergens, D.; Bennett, N. R.; Trippe, B. L.; Yim, J.; Eisenach, H. E.; Ahern, W.; Borst, A. J.; Ragotte, R. J.; Milles, L. F.; Wicky, B. I. M.; Hanikel, N.; Pellock, S. J.; Courbet, A.;

Sheffler, W.; Wang, J.; Venkatesh, P.; Sappington, I.; Torres, S. V.; Lauko, A.; De Bortoli, V.; Mathieu, E.; Ovchinnikov, S.; Barzilay, R.; Jaakkola, T. S.; DiMaio, F.; Baek, M.; Baker, D. De Novo Design of Protein Structure and Function with RFdiffusion. *Nature* **2023**, *620* (7976), 1089–1100. https://doi.org/10.1038/s41586-023-06415-8.

(248) Madani, A.; Krause, B.; Greene, E. R.; Subramanian, S.; Mohr, B. P.; Holton, J. M.; Olmos, J. L.; Xiong, C.; Sun, Z. Z.; Socher, R.; Fraser, J. S.; Naik, N. Large Language Models Generate Functional Protein Sequences across Diverse Families. *Nat Biotechnol* **2023**, *41* (8), 1099–1106. https://doi.org/10.1038/s41587-022-01618-2.

(249) Ingraham, J. B.; Baranov, M.; Costello, Z.; Barber, K. W.; Wang, W.; Ismail, A.; Frappier, V.; Lord, D. M.; Ng-Thow-Hing, C.; Van Vlack, E. R.; Tie, S.; Xue, V.; Cowles, S. C.; Leung, A.; Rodrigues, J. V.; Morales-Perez, C. L.; Ayoub, A. M.; Green, R.; Puentes, K.; Oplinger, F.; Panwar, N. V.; Obermeyer, F.; Root, A. R.; Beam, A. L.; Poelwijk, F. J.; Grigoryan, G. Illuminating Protein Space with a Programmable Generative Model. *Nature* **2023**, *623* (7989), 1070–1078. https://doi.org/10.1038/s41586-023-06728-8.

(250) Gazizov, A.; Lian, A.; Goverde, C.; Ovchinnikov, S.; Polizzi, N. F. AF2BIND: Predicting Ligand-Binding Sites Using the Pair Representation of AlphaFold2. bioRxiv October 18, 2023, p 2023.10.15.562410. https://doi.org/10.1101/2023.10.15.562410.